

Master of Science Thesis

---

# Computational Analysis of Base Drag Reduction Using Active Flow Control

P.M. van Leeuwen

---

November 2009



# Computational Analysis of Base Drag Reduction Using Active Flow Control

Master of Science Thesis

For obtaining the degree of Master of Science in Aerospace  
Engineering at Delft University of Technology

P.M. van Leeuwen

November 2009



**Delft University of Technology**

Copyright © Aerospace Engineering, Delft University of Technology  
All rights reserved.

DELFT UNIVERSITY OF TECHNOLOGY  
DEPARTMENT OF AERODYNAMICS

The undersigned hereby certify that they have read and recommend to the Faculty of Aerospace Engineering for acceptance the thesis entitled “**Computational Analysis of Base Drag Reduction Using Active Flow Control**” by **P.M. van Leeuwen** in fulfillment of the requirements for the degree of **Master of Science**.

Dated: November 2009

Supervisors:

---

Prof. dr. ir. drs. H. Bijl

---

Prof. dr. ir. B. Koren

---

Ir. G.M.R. van Raemdonck

---

Prof. dr. ir. M.J.L. van Tooren

---

Ir. L.M.M. Boermans



---

# Summary

Increasing fuel prices and the increasing environmental awareness has led to an increasing importance of truck aerodynamics in the automotive transport sector. At highway speeds the aerodynamic drag of a truck leads to 40% of the total fuel consumption, making aerodynamic improvements an important field of possible fuel consumption reduction. For a typical truck 35% of this drag is generated by the base of the truck due to the large wake area and the turbulent flow behavior behind the truck. Different aerodynamic devices have been developed in the past to reduce this area of turbulence and in this thesis an active systems has been analyzed.

Using the Coanda effect the wake size can be reduced significantly and thereby an increase in base pressure can be achieved. Using a compressor, flow is blown past curved surfaces attached to the back of the truck, causing the shear layers to curve more inward and thereby reducing the wake size. The drag reduction is significantly but the reduction in fuel consumption is less due to the energy consumption of the active flow system.

The active system is attached to a generic truck system (GETS) and analyzed by computational fluid dynamics. The RANS equations with a two equation turbulence model are solved on a hybrid grid constructed around the geometry. To accelerate the design process the grid generation is automated and the different grids, boundary conditions and model scales are tested on the generic model and compared to available wind tunnel data. Using the results of the generic model the active drag reduction model is added to the system and CFD is applied to analyze the flow field and minimize the drag coefficient.

Different grids and boundary conditions are simulated on a full scale GETS model and a half grid on a symmetric floor boundary condition prove applicable when base pressures are of interest, which leads to a reduction in grid cells. The wind tunnel scale model differs from the full scale CFD model in terms of boundary layer development. Compared to wind tunnel measurements performed on a scale model the base pressures differ as well in the CFD results. Differences in the model occur on the bottom side of the model due to interaction between the floor and the model boundary layers.

The aerodynamic coefficients agree well for the simulated and wind tunnel results in terms of drag and the trends in average base pressure. Using CFD the active flow control system proved to achieve a drag reduction of 20% which would lead to a reduction in fuel consumption of 5 to 10%. Due to the energy consumption of the active system moderate blowing on a boat tail like geometry prove to be most efficient. For higher blowing velocities and momentum coefficients the wake length can be shortened by 85% and the shear layers curve inwards significantly causing a large increase in base pressure. Different geometric variations are simulated and different flow topologies are observed at different momentum coefficients and velocity ratios.

In conclusion, applying an active flow control system on trucks can reduce drag and the resulting fuel consumption. However, for practical implementations the energy consumption and therefor the compressor system efficiency is a significant factor in making this system a success.



---

# Preface

This thesis is written as a graduate thesis as part of the Masters Program at the faculty of Aerospace Engineering at the Delft University of Technology. It finalizes the Masters variant Aerodynamics and focuses on aerodynamic design using computational fluid dynamics.

The reduction of drag for heavy duty vehicles is the subject of this thesis and a phenomena used in certain aircrafts is applied to a truck model and analyzed using CFD. This subject gave me the opportunity to apply CFD and work with the advantages and drawbacks found during the application of CFD. The aim of this thesis is to provide the reader a description of the performed work and to present the findings.

I would like to thank my supervisor Ir. G. van Raemdonck for his guidance throughout this project and I wish him the best with his PhD and his company aimed at applying aerodynamic devices in industry. Furthermore I would like to express my gratitude to Prof. B. Koren for his support and interest in my thesis. Also the interest and the invested time in my work from the other members in my exam committee is much appreciated. Many thanks to E. de Keizer and M. Haanschoten for their assistance with any software and hardware related issues.

Peter van Leeuwen  
Delft, November 2009



---

# Table of Contents

<b>Summary</b>	<b>v</b>
<b>Preface</b>	<b>vii</b>
<b>List of Figures</b>	<b>xiii</b>
<b>List of Tables</b>	<b>xvii</b>
<b>Nomenclature</b>	<b>xix</b>
<b>1 Trucks and Aerodynamics</b>	<b>1</b>
1.1 Introduction . . . . .	1
1.2 Generic European Transport System . . . . .	2
1.2.1 Reynolds number . . . . .	4
<b>2 Bluff Body Aerodynamics</b>	<b>5</b>
2.1 Bluff body flow . . . . .	5
2.1.1 Vortex structure . . . . .	5
2.1.2 Steady wake drag model . . . . .	7
2.2 Base drag reduction devices for trucks . . . . .	7
2.3 Coanda effect . . . . .	9
2.3.1 Momentum coefficient . . . . .	10
2.3.2 Energy balance . . . . .	11
<b>3 Numerical Aspects</b>	<b>13</b>
3.1 Flow modeling . . . . .	13
3.2 Turbulence modeling . . . . .	14
3.2.1 Filtering versus statistical approach . . . . .	14
3.2.2 Closure model . . . . .	15
3.3 Wall treatment . . . . .	16
3.4 Model setup . . . . .	18
3.4.1 Boundary conditions . . . . .	19
3.4.2 Solver settings . . . . .	20
3.5 Numerical diffusion . . . . .	22

<b>4</b>	<b>Grid Generation</b>	<b>23</b>
4.1	Parametric approach . . . . .	23
4.2	Numerical domain . . . . .	24
4.2.1	Grid blocks . . . . .	25
4.3	GETS grid . . . . .	27
4.3.1	Boundary layer grid . . . . .	27
4.3.2	Unstructured grid . . . . .	29
4.4	Active Flow Control grid . . . . .	31
4.4.1	Velocity inlet geometry . . . . .	31
4.4.2	Boundary layer grid . . . . .	33
4.4.3	Unstructured grid . . . . .	35
<b>5</b>	<b>Simulation Results GETS Model</b>	<b>37</b>
5.1	Wall function validity . . . . .	37
5.2	Grid independence . . . . .	37
5.3	Grid dimensions . . . . .	40
5.4	Floor boundary condition . . . . .	41
5.5	Flow analysis of the GETS model . . . . .	44
5.6	Wind tunnel comparison . . . . .	48
5.6.1	Simulation results comparison . . . . .	48
5.6.2	Boundary layer comparison . . . . .	50
5.6.3	Yaw sensitivity . . . . .	52
5.6.4	Base pressure comparison . . . . .	53
5.7	Concluding remarks . . . . .	55
<b>6</b>	<b>Design of the Active Flow Control System</b>	<b>57</b>
6.1	Drag determination . . . . .	57
6.2	Englar's reference case . . . . .	58
6.3	Analysis of the reference case . . . . .	59
6.4	Jet turning . . . . .	61
6.4.1	Full jet turning . . . . .	61
6.4.2	Jet separation . . . . .	65
6.5	Geometric variations . . . . .	70
6.5.1	Slot height variation . . . . .	70
6.5.2	Radius variation . . . . .	72
6.5.3	Angle variation . . . . .	73
6.6	Design optimization . . . . .	74
6.7	Concluding remarks . . . . .	78
<b>7</b>	<b>Conclusions and Recommendations</b>	<b>79</b>
7.1	Conclusions . . . . .	79
7.2	Recommendations . . . . .	80
	<b>Bibliography</b>	<b>81</b>

---

<b>A</b>	<b>Momentum Coefficient Background</b>	<b>85</b>
A.1	Dimensional analysis . . . . .	85
A.2	Energy equation . . . . .	87
<b>B</b>	<b>Grid Parameters</b>	<b>89</b>
<b>C</b>	<b>Element Properties and Richardson Extrapolation</b>	<b>91</b>
C.1	Grid topologies . . . . .	91
C.2	Grid quality criteria . . . . .	93
C.3	Richardson extrapolation . . . . .	94
C.3.1	Extrapolation results . . . . .	95
<b>D</b>	<b>Additional Computational Results of the GETS System</b>	<b>97</b>
<b>E</b>	<b>Additional Computational Results of the AFC System</b>	<b>101</b>
E.1	Grid independence and quality metrics . . . . .	101
E.1.1	Wall function validity . . . . .	101
E.1.2	Grid independence . . . . .	102
E.1.3	Grid cut location . . . . .	104
E.1.4	Grid dimensions . . . . .	105
E.2	AFC system results . . . . .	106
E.2.1	Englar's reference case . . . . .	106
E.2.2	Slot height variation . . . . .	110
E.2.3	Radius variation . . . . .	110
E.2.4	Design optimization . . . . .	111



---

# List of Figures

1.1	Crude oil prices since 1975, corrected for inflation [24]	1
1.2	Tractor-trailer	2
1.3	Different flow topology due to tractor streamlining [36]	2
1.4	GETS model	3
2.1	Near wake visualization and ring vortex	6
2.2	Vortex shedding in near wake [13]	6
2.3	Steady wake drag representation [44]	7
2.4	Truck with boat tail	8
2.5	Schematic representation of guiding vanes on GETS model	8
2.6	Coanda Effect	9
2.7	circulation control applied to a truck by Englar [45]	10
2.8	Conceptual add-on Active Flow Control device	10
2.9	Compressor power	12
3.1	Dimensionless velocity profile for a turbulence wall flow	17
3.2	Boundary conditions on simulated domains	19
3.3	Theoretical and simulated and interpolated boundary layer thickness	22
4.1	Script files structure	24
4.2	Overview of domain including GETS (half) model	25
4.3	Absolute pressure coefficient in symmetry plane of GETS model	26
4.4	Wake enclosure (red) for GETS-half model (green)	26
4.5	Surface mesh details of GETS-half model	27
4.6	Grid topologies	28
4.7	Boundary layer mesh of GETS-half model	28
4.8	Grid refinements around GETS Model in symmetry plane	29
4.9	Prism layer under the GETS Model	29
4.10	Domain grid overview of half model	30
4.11	AFC geometry definitions	31
4.12	Half AFC model in rear iso view	32
4.13	Different velocity inlet geometries	32
4.14	AFC grid sectors in symmetry plane (schematic)	33
4.15	Surface and boundary layer mesh of AFC-half model	34
4.16	Grid connection 2D (schematic)	35

4.17	Domain grid AFC-half model . . . . .	36
5.1	$y^+$ values on GETS model . . . . .	37
5.2	Convergence of drag and lift coefficient . . . . .	38
5.3	Residuals GETS simulation, 6.1M cells . . . . .	38
5.4	Drag and Lift convergence for different grid sizes . . . . .	39
5.5	Velocity profiles at three stations behind the GETS model . . . . .	39
5.6	Base pressure coefficient . . . . .	41
5.7	Velocity profiles behind the GETS model ( $Z = 0$ indicating ground plane) . . . . .	42
5.8	Close up of velocity profiles behind the GETS model ( $Z = 0$ indicating ground plane) . . . . .	43
5.9	Pressure difference ( $C_{p,moving} - C_{p,symmetric}$ ) . . . . .	43
5.10	Drag distribution on GETS model . . . . .	44
5.11	Pressure distributions GETS . . . . .	45
5.12	Contour slices indicating trailing vortex . . . . .	46
5.13	Wake visualization GETS model . . . . .	47
5.14	Velocity profiles behind the GETS model (stationary and moving BC) . . . . .	49
5.15	Velocity profiles behind the GETS model (stationary floor BC) . . . . .	50
5.16	Boundary layer development underneath the model . . . . .	51
5.17	Force and pressure coefficient for increasing yaw angle . . . . .	52
5.18	Streamlines indicating vortices for $\beta = 9^\circ$ , streamlines colored by velocity magnitude . . . . .	53
5.19	Base pressure comparison wind tunnel, measured and CFD for $\beta = 0^\circ$ . . . . .	53
5.20	Base pressure comparison wind tunnel, measured and CFD for $\beta = 6^\circ$ . . . . .	54
5.21	$C_{P,base}$ at different positions on the base for $\beta = 0^\circ$ , 0.65mm zigzag tape . . . . .	54
6.1	Reference Case Results . . . . .	59
6.2	Drag force split for $R_1 = 0.058w$ and $R_1 = 0.116w$ . . . . .	60
6.3	Jet sheet for separation for $C_\mu = 0.021$ and flow turning for $C_\mu = 0.073$ , $R_1 = 0.116w$ . . . . .	61
6.4	Flow structure in wake for $R_1 = 0.058w$ and $R_1 = 0.116w$ . . . . .	62
6.5	Streamlines originating from base for $R_1 = 0.058w$ and $R_1 = 0.116w$ . . . . .	62
6.6	Base pressure coefficients for $R_1 = 0.116w$ and $R_1 = 0.058w$ . . . . .	63
6.7	Velocity profiles in wake for $R_1 = 0.058w$ , $C_\mu = 0.061$ and $R_1 = 0.116w$ , $C_\mu = 0.073$ . . . . .	63
6.8	Velocity magnitude for both radii (full jet turning) . . . . .	64
6.9	Large (left) and small (right) radius geometry . . . . .	65
6.10	Boundary layer comparison at $x = L, y = 0$ (top side) . . . . .	66
6.11	Velocity profiles in symmetry plane, $C_\mu = 0.035$ . . . . .	67
6.12	Edge vortices originating from Coanda surface intersection, $R_1 = 0.058w$ . . . . .	68
6.13	Streamlines and projected vortex core, $R_1 = 0.116w$ . . . . .	68
6.14	Base pressure coefficients for $R_1 = 0.058w$ and $R_1 = 0.116w$ . . . . .	69
6.15	Velocity profiles in wake for $R_1 = 0.058w$ , $C_\mu = 0.061$ and $R_1 = 0.116w$ , $C_\mu = 0.073$ . . . . .	69
6.16	Velocity magnitude for $R_1 = 0.058w$ (jet separation) . . . . .	70
6.17	Slot height variation for $R = 0.116w$ and $R = 0.058w$ . . . . .	71
6.18	$\Delta C_{D^*}$ vs $C_\mu$ for various radii . . . . .	72
6.19	$C_\mu$ vs $\zeta$ colored by $C_D$ . . . . .	75

6.20	Response surfaces for $C_{D^*}$ and $C_{D,0.7}$ . . . . .	75
6.21	Response surfaces for $C_D$ for increasing $C_{p,i}$ . . . . .	76
6.22	Different $R_2/R_1$ ratios compared to a boat tail with 10 degrees slant angle . . . . .	77
C.1	Grid topologies [3] . . . . .	91
C.2	Example of unwanted grid refinement . . . . .	92
C.3	Different element properties . . . . .	94
D.1	Wake Station aft of the base, in the $y = 0$ plane . . . . .	97
D.2	Base Pressure in XZ-plane . . . . .	98
D.3	Base Pressure in XY-plane . . . . .	98
D.4	Steady vorticity iso-surfaces (streamlines colored by velocity magnitude) . . . . .	99
E.1	$y^+$ values on rear section of Coanda system model . . . . .	101
E.2	Convergence of drag and lift coefficient . . . . .	102
E.3	Residuals AFC simulation, 5.5M cells . . . . .	103
E.4	Drag and Lift convergence for different grid sizes . . . . .	103
E.5	Velocity profiles in the symmetry plane at different stations behind the AFC model . . . . .	104
E.6	Pressure coefficient in symmetry plane of GETS model (modified scale) . . . . .	104
E.7	Pressure coefficient at $x=4.4w$ for both GETS and AFC model . . . . .	105
E.8	Base pressure coefficient half and full model, ( $R_1 = 0.116w$ , $h = 1.5 \cdot 10^{-3}w$ , $C_\mu = 0.021$ ) . . . . .	106
E.9	Vorticity magnitude for both models with jet turning and separated jet sheet . . . . .	107
E.10	Total pressure for the GETS model, the AFC model with jet turning and separated jet sheet . . . . .	108
E.11	Vorticity iso surfaces for AFC model with jet turning and separated jet sheet . . . . .	109
E.12	Wake visualization optimal AFC model . . . . .	112



---

# List of Tables

1.1	GETS model dimensions . . . . .	3
3.1	Wall approach properties . . . . .	18
3.2	Boundary conditions . . . . .	20
3.3	Summarized solver settings . . . . .	21
4.1	Element and type distribution for GETS model . . . . .	30
4.2	Element and type distribution in GETS model . . . . .	36
5.1	Locations of saddle point and vortex cores . . . . .	40
5.2	Flow properties for different floor BC's . . . . .	42
5.3	Boundary Layer properties at $x = L$ ( $y = 0, z = 0.5H$ ) . . . . .	45
5.4	Full scale and wind tunnel model data . . . . .	48
5.5	Full scale and wind tunnel model data . . . . .	49
5.6	Data from wind tunnel and full scale simulations, coordinates expressed in $X/W$ and $Z/H$ . . . . .	49
5.7	Boundary Layer properties at the top surface ( $x = 6.27W, y = 0$ ) . . . . .	51
6.1	Englar's tested geometries . . . . .	58
6.2	Data from 2 full jet turning simulations, coordinates expressed in $X/W$ and $Z/H$ . . . . .	61
6.3	Data from two jet separation simulations, coordinates expressed in $X/W$ and $Z/H$ . . . . .	65
6.4	Data for slot height variation, coordinates expressed in $h/W, X/W$ and $Z/H$ . . . . .	71
6.5	Data for radius variation, coordinates expressed in $R_1/W, X/W$ and $Z/H$ . . . . .	72
6.6	Parameter range for design optimization, expressed in $R/W$ and $h/W$ . . . . .	74
6.7	Design optimization results for different compressor inlet pressures . . . . .	77
B.1	Model Parameters GETS and AFC model . . . . .	89
B.2	Model Parameters GETS and AFC model (dimensions in $[m]$ ) . . . . .	90
C.1	Richardson extrapolation data . . . . .	95
E.1	Data for $R_1 = 0.116, h = 1.5e - 003$ , coordinates expressed in $X/W$ and $Z/H$ . . . . .	105
E.2	Results Reference Case . . . . .	106
E.3	Results Variation of slot height . . . . .	110
E.4	Results variation of radius . . . . .	110
E.5	Results design optimization . . . . .	111



---

# Nomenclature

## Latin Symbols

$A$	Area	$[m^2]$
$C_D$	Drag Coefficient	$[-]$
$C_{D^*}$	Uncorrected Drag Coefficient	$[-]$
$C_f$	Friction Coefficient	$[-]$
$C_p$	Pressure Coefficient	$[-]$
$C_L$	Lift Coefficient	$[-]$
$C_\mu$	Momentum Coefficient	$[-]$
$C_S$	Side Force Coefficient	$[-]$
$C_T$	Tangential Force Coefficient	$[-]$
$D$	Drag Force	$[N]$
$F_{thrust}$	Thrust Force	$[N]$
$g$	Gravity Acceleration	$[m/s^2]$
$h$	Slot Height	$[m]$
$H$	Shape Factor	$[-]$
$H$	Model Height	$[m]$
$I$	Turbulence Intensity	$[-]$
$k$	Turbulent Kinetic Energy	$[m^2/s^2]$
$L$	Length	$[m]$
$L$	Model Length	$[m]$
$M$	Mach Number	$[-]$
$\dot{m}$	Mass Flow	$[kg/s]$
$p$	Pressure	$[N/m^2]$
$P$	Power	$[W]$
$q$	Dynamic Pressure	$[N/m^2]$
$R$	Radius	$[m]$
$Re$	Reynolds Number	$[-]$
$Re_y$	Turbulent Reynolds Number	$[-]$
$s$	Traveled Distance	$[m]$
$t$	Time	$[s]$
$V$	Velocity	$[m/s]$

$u$	x-component of Velocity	$[m/s]$
$v$	y-component of Velocity	$[m/s]$
$w$	z-component of Velocity	$[m/s]$
$w$	Model Width	$[m]$
$X$	x-coordinate	$[m]$
$Y$	y-coordinate	$[m]$
$Z$	z-coordinate	$[m]$
$y_c$	Cell Center	$[m]$
$y^+$	Wall Coordinate	$[-]$

### Greek Symbols

$\alpha$	Grid Element Angle	$[deg]$
$\alpha_{urf}$	Under Relaxation Factor	$[-]$
$\beta$	Yaw Angle	$[deg]$
$\delta$	Boundary Layer Thickness	$[m]$
$\delta_{ij}$	Kronecker Delta	$[-]$
$\ell$	Turbulent Length Scale	$[m]$
$\epsilon$	Turbulent Dissipation Rate	$[m^2/s^2]$
$\eta$	Efficiency	$[-]$
$\mu$	Viscosity	$[Ns/m^2]$
$\mu_{turb}$	Turbulent Viscosity	$[Ns/m^2]$
$\phi$	Scalar Quantity	$[-]$
$\Pi$	Buckingham II Product	$[-]$
$\psi$	Zero Streamline	$[-]$
$\rho$	Density	$[kg/m^3]$
$\tau$	Shear Stress	$[N/m^2]$
$\tau_{wall}$	Wall Shear Stress	$[N/m^2]$
$\theta$	Coanda Surface Angle	$[deg]$
$\theta'$	Additional Coanda Surface Angle	$[deg]$
$\zeta$	Velocity Ratio	$[-]$

## Subscripts

1	First Direction
2	Second Direction
<i>aero</i>	Aerodynamic
<i>avg</i>	Average
<i>c</i>	Compressor
<i>e</i>	Equilateral
<i>i</i>	Inlet
$\infty$	Freestream
<i>j</i>	Jet
<i>max</i>	Maximum
<i>min</i>	Minimum
<i>ref</i>	Reference
<i>SP</i>	Saddle Point
<i>t</i>	Transcritical
<i>V1</i>	Vortex Core One
<i>V2</i>	Vortex Core Two

## Abbreviations

<i>AFC</i>	Active Flow Control
<i>BC</i>	Boundary Condition
<i>BL</i>	Boundary Layer
<i>CFD</i>	Computational Fluid Dynamics
<i>D</i>	Dimensional
<i>DES</i>	Detached Eddy Simulation
<i>FVM</i>	Finite Volume Method
<i>GETS</i>	Generic European Transport System
<i>GTS</i>	Generic Transport System
<i>LES</i>	Large Eddy Simulation
<i>RANS</i>	Reynolds Averaged Navier Stokes
<i>RNG</i>	ReNormalization Group
<i>RSM</i>	Reynolds Stress Model
<i>SAE</i>	Society of Automotive Engineers
<i>SIMPLE</i>	Sem-Implicit Method for Pressure Linked Equations
<i>SIMPLEC</i>	Sem-Implicit Method for Pressure Linked Equations Consistent
<i>SST</i>	Shear-Stress Transport
<i>STOL</i>	Short Take Off and Landing
<i>TCL</i>	Tool Command Language
<i>URF</i>	Under Relaxation Factor



---

# Chapter 1

---

## Trucks and Aerodynamics

In this chapter the background and motivation for this research is discussed as well as the structure of this thesis. Some basic principles of aerodynamics are explained and the definition of the used geometric model is described.

### 1.1 Introduction

Traditionally aerodynamics is related to airplanes and some (high performance) automotive applications, where most applications are esthetically driven. The interest in truck aerodynamics is mainly driven by the increase in the price and environmental burden of fossil fuels. In figure 1.1, the inflation corrected crude oil price per barrel is shown since 1975, indicating the rapid increase in the last decade. According to [25] approximately 40% of the fuel consumption of trucks is due to aerodynamic drag, making aerodynamics an important factor in the financial and environmental impact of the transport sector.

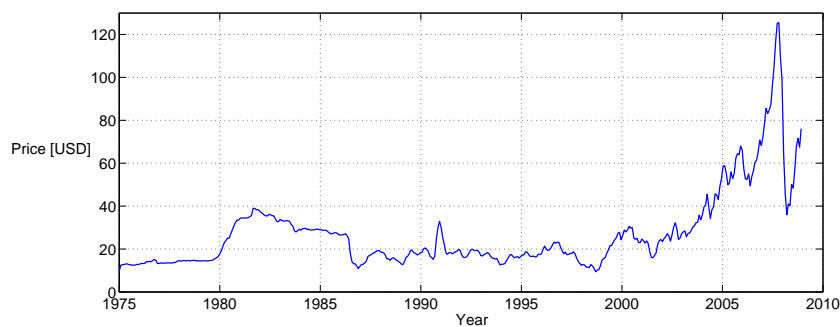


**Figure 1.1:** Crude oil prices since 1975, corrected for inflation [24]

Truck aerodynamics is generally aimed at reducing the drag and improving the flow quality on the front end of the tractor, whereas less attention is given to the aerodynamics of the trailer as the shape is modified for low cost and maximum loading capacity. The drag contribution of the trailer is between 50 to 60% [54], implying that reducing the aerodynamic drag of the trailer could lead to a significant reduction in fuel consumption.

In this thesis a system is analysed which is a derivative of a lift producing device used in certain types of aircraft [41], using an aerodynamic effect called the Coanda effect. This effect can be applied to influence the aerodynamics of the truck resulting in a drag reduction. This approach

has been tested mainly experimentally in the US [14] but the precise results are not clear as is the distinction between the different mechanisms of the actual drag reduction.

Most of the computational analysis on this Coanda effect is performed using two dimensional models, whereas the flow around trucks is highly three dimensional leading to the necessity of a three dimensional model, as will be shown later. This thesis consists of a numerical analysis of the drag reduction device and a comparison with the aerodynamic behavior of a clean truck model. As the computational setup time is a dominant time constraint in engineering applications the modeling setup is automated to a large extent in order to be able to increase the amount of design iterations.

At first the geometric model used to analyse the base drag aerodynamics and some background on base drag and existing drag reduction devices are discussed in chapter 2. The numerical background and computational setup of the computational fluid dynamics models is discussed in chapter 3 and 4, for the latter a separate chapter is dedicated as this is a fundamental aspect of CFD simulations, a low quality grid can influence the solution significantly.

The results and the flow around the geometric base model is discussed in chapter 5 and the simulations are compared to previously conducted experiments and other research related to truck aerodynamics. The design of the active flow control system is discussed in chapter 6 and conclusions and recommendations finalize this project in chapter 7.

## 1.2 Generic European Transport System

Various aerodynamics devices have been developed mainly to guide the airflow around the tractor (figure 1.2), the most applied features are the front edge turning vane and the top cabin fairing placed on the tractor.

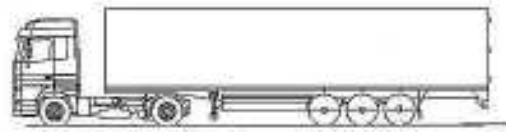


Figure 1.2: Tractor-trailer

These devices are aimed at reducing the separated flow regions on the front end of the truck, see figure 1.3. In the regions where the airflow separates from the tractor body the drag increases significantly, indicated by the regions of turbulence (regions which cause drag). The gap between the tractor and the trailer is furthermore a significant contribution to the total drag of the truck, which can be reduced by minimizing the gap (sometimes achieved by applying cab extension fenders).

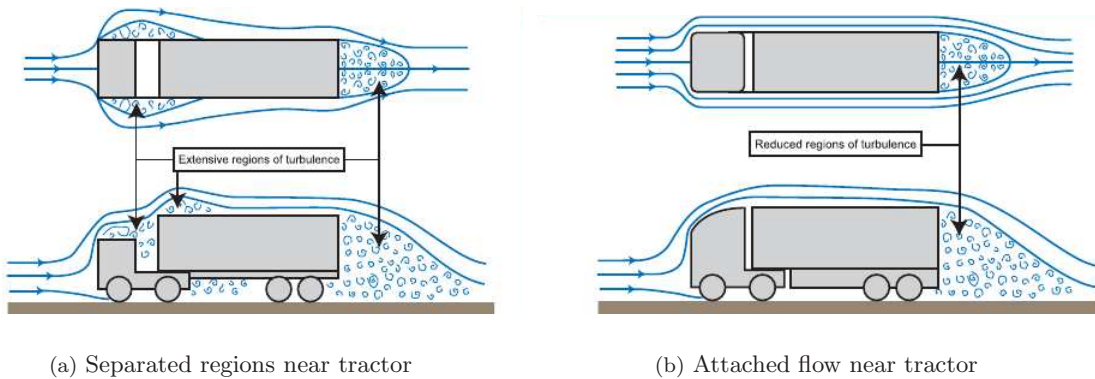


Figure 1.3: Different flow topology due to tractor streamlining [36]

As can be seen in figure 1.3 the turbulence regions are reduced by streamlining the tractor and minimizing the tractor-trailer gap. The drag created by the trailer however, is not significantly affected by this. The rear of the trailer is less aerodynamically optimized, compared to most tractors, while nearly 60% of the total drag is caused by the trailer wheels and the base [54]. This research focuses on the drag caused by the base of the trailer and assumes the flow coming from the tractor to be attached (as shown in 1.3(b)). Attached flow from the front end of the truck minimizes the effects of the fore body on the wake and therefore reduces the effect of the front of the model on the design of the drag reduction device.

To facilitate this study in truck aerodynamics a model which is representative of a European tractor-trailer combination is used. A clean model with the maximum dimensions allowed in Europe for trucks is used in computations and in other research projects for wind tunnel tests. By using the same model as in other experiments and computations the results can be compared and a database with relevant data and drag reduction methods can be stored.

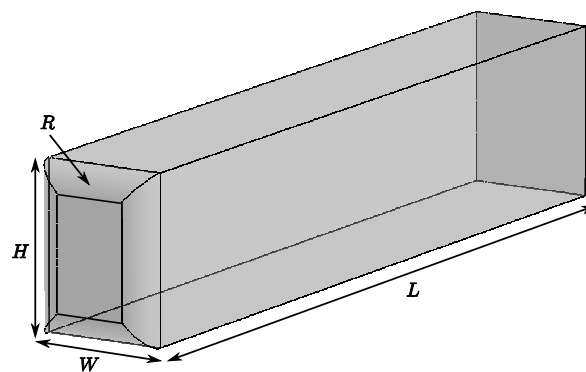


Figure 1.4: GETS model

In figure 1.4 the GETS (*Generic European Transport System*) model is shown, with its dimensions tabulated in table 1.1. The GETS model is the European version of the US GTS model used in various research, with the difference that the front end is less streamlined which is more in line with European tractor design. As can be seen in the figure significant simplifications are applied compared to a real tractor trailer. These simplifications are applied because this model is designed in order to research base drag and the aerodynamics of the wake. The added complexity of mirrors, wheels and the gap between the tractor and the trailer lead to increased complexity of the (computational and wind tunnel) models. Although these effects influence the wake and the base drag of the truck, to gain understanding of the base drag mechanism a clean model is preferred.

Length [m]	16.5	Width [m]	2.595
Height [m]	3.51	Radius [m]	0.540
Ground clearance [m]	0.495	Wind tunnel scale	1 : 15

Table 1.1: GETS model dimensions

The front edge radius is equal on all edges and chosen such that the flow remains attached under zero yaw conditions. According to Cooper [10] the transcritical Reynolds number, defined as

$$(Re_r)_t = \frac{\rho R V_t}{\mu} \quad (1.1)$$

and can be considered as the Reynolds number based on the front end radius. As found in [10] and [22] this value should be  $(Re_r)_t = 1.24 \cdot 10^5$  for the flow to remain attached. This value decreases with increasing turbulence intensity, which is relevant for the full scale simulations, meaning the front end radius can be decreased for the full scale model as the relatively large radius is not preferred from a practical point of view. Using equation 1.1 a front radius for the 1 : 15 scale wind tunnel model was found of 36 mm, which leads to a radius of 540 mm for the full scale model.

### 1.2.1 Reynolds number

The Reynolds number based on the length of the model and using a freestream velocity of 25 m/s equals 28M for the full scale model. As the length of the model is less determinant for the flow dynamics compared to the width and height of the model it is more sensible to define the Reynolds number on the width or the square root of the frontal area of the model as is also frequently used in literature. Based on the width of the model (as will be used throughout this thesis) the full scale Reynolds number is 4.5M.

In [5, 6] the dependency of the drag coefficient on the Reynolds number based on the model width has been tested experimentally in the NASA-Ames 40ft wind tunnel as part of the US Department of Energy research of truck aerodynamics. The Reynolds number was varied from 1M to 6M for various configurations of a Generic Conventional Model (GCM), and it is observed that the drag coefficient is independent on the Reynolds number for  $Re > 1M$ . This experiment has been repeated for the GETS model by varying the Reynolds number from 0.8M tot 1.5M in [55]. In this range no Reynolds dependency was detected for the drag coefficient.

These experiments are in agreement with the SAE wind tunnel test procedure for trucks and buses [1], which states that the Reynolds number should exceed  $Re > 0.7M$  to ensure drag independence of the Reynolds number.

# Bluff Body Aerodynamics

In this chapter the basic aerodynamic phenomena of truck base drag is explained and several existing drag reduction devices are discussed. The aerodynamic effect which has a central role in this thesis, the Coanda effect, is discussed and finally the implications of an active aerodynamic device on the determination of the drag reduction is discussed.

## 2.1 Bluff body flow

The term bluff body is devised for aerodynamic bodies where the total drag consists of mainly pressure drag and the friction drag is a small portion of the total drag. Flow separation plays an important role in the total drag of bluff bodies since pressure drag is a result of flow separation. Most automotive applications are concerned with bluff body aerodynamics, even in the cases where streamlining is applied the flow still separates and the drag is dominated by pressure drag.

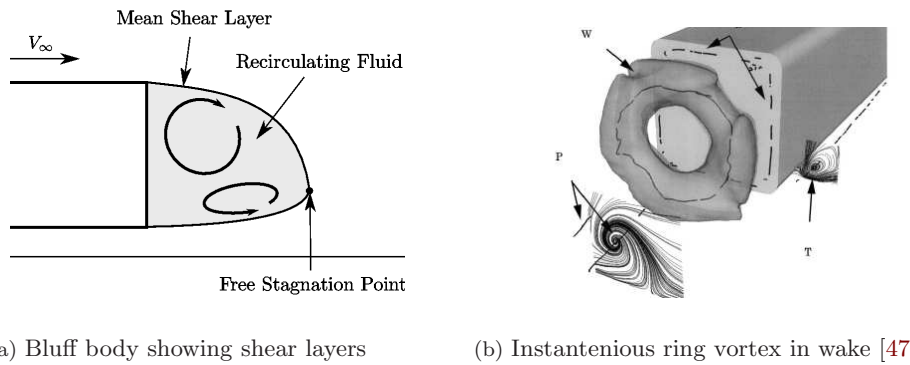
### 2.1.1 Vortex structure

The GETS model is a bluff body, where flow separation occurs only at the back of the model. The front edge radius is chosen such that the flow remains attached and the boundary layers can develop on the surfaces of the model. The boundary layers on the side top and bottom reach the base of the model and separate on the aft edge of the model forming free shear layers. These shear layers curve towards each other and close in the free stagnation point, see figure 2.1(a). The shear layers enclose a region of recirculating air, called the wake and this structure of the recirculating air in the wake is an unsteady three dimensional process.

The recirculating fluid in the wake forms a vortex, with a continuous vortex core and which is described as a ring vortex. In figure 2.1(b) an instantaneous representation of the vortex core is shown obtained by LES simulations from [47]. This vortex imposes a pressure field on the base of the trailer responsible for the suction force acting on the base.

The vortex ring and the shear layers encapsulating is not a steady process however, small eddies develop in the shear layer and are convected downstream while growing in size. The larger vortical structures separate from the shear layer at a shedding frequency causing the wake to decrease in size and the free stagnation point to move upstream closer towards the base as is displayed in figure 2.2.

This vortex shedding and moving of the free stagnation point is called bubble pumping and is an unsteady effect in the recirculation region. The fluid shed from the recirculation region in the form of a vortex is equal to the average amount of fluid which is entrained in the recirculation region



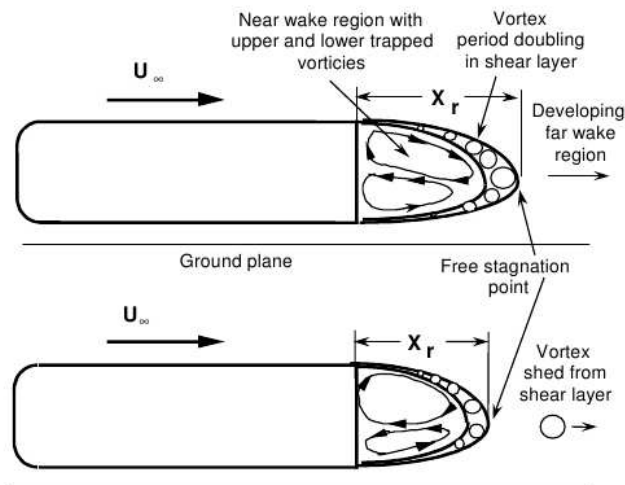
(a) Bluff body showing shear layers

(b) Instantaneous ring vortex in wake [47]

**Figure 2.1:** Near wake visualization and ring vortex

through the shear layers [13]. This continuous process of fluid entrainment through the shear layers and the periodic shedding of vortices causes the flow behind the truck to be unsteady.

The development of the small eddies in the shear layers which leads to the eventual shedding of vortices in the wake requires a modeling approach capable of capturing the small size eddies, which is not practical for conceptual engineering projects. Furthermore as this unsteady process is not fully understood, it remains a subject of research. The unsteady behavior of the shear layers is not treated in this thesis and a time-averaged flow field is evaluated in order to obtain the overall force balance on the model.

**Figure 2.2:** Vortex shedding in near wake [13]

### 2.1.2 Steady wake drag model

In the absence of vortex shedding and assuming a steady wake Roshko proposed a base drag model [44]. The model is demonstrated using figure 2.3 showing a bluff plate and a wake splitter plate, which is modelled by an elliptic wake behind the bluff plate.

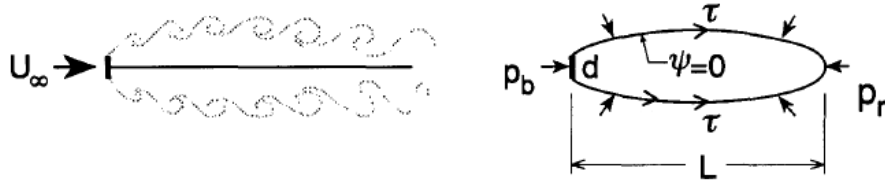


Figure 2.3: Steady wake drag representation [44]

The shear layers re-attach at a distance  $L$  from the bluff plate and enclose the wake with the zero streamline  $\Psi = 0$ . Since vortex shedding is absent the highest shear stresses are found in the shear layer or at  $\Psi = 0$ . As the base pressure is determined by the pressure in the wake and the distribution of shear stresses, the force equilibrium between the shear and pressure force can be written as (assuming a symmetric wake)

$$\oint_{\Psi=0} p dz + \oint_{\Psi=0} \tau dx = 0. \quad (2.1)$$

This expression assumes that all the shear stresses are focused on the  $\Psi = 0$  streamline which is shown in [56] to be incorrect: downstream of the wake the shear stresses are distributed throughout the shear layer due to diffusion. Although it is a rough model, it clearly indicates that a shorter re-attachment length lowers the contribution of the shear stresses in 2.1 and thus increases the average pressure in the wake. If the pressure would be constant in the wake this would result in a higher base pressure and thus a reduction in base drag. The pressure is not constant in the wake however, but is influenced by the presence of the ring vortex in the wake.

Although the various assumptions minimize the practical usability of above described model, the result of reducing the wake size is the fundamental principle behind many different base drag reduction devices as discussed in the next section.

## 2.2 Base drag reduction devices for trucks

Aerodynamic devices for base drag reduction for trucks are under development since a long time, where the streamlined afterbody (a boat tail) is the most intensively investigated solution. A boat tail consists of four surfaces attached to the back of the trailer, thereby streamlining the trailer, delaying separation and thus reducing the wake size, see figure 2.4.

Several different versions of the boat tail exist, the traditional boat tail [53], the stepped boat tail or boat tail cavity [51], the boat tail with curved flaps [33] and the boat tail with modified inner cavity [53]. The drag reduction achieved with a boat tail system is in the order of 9 to 12% for a baseline tractor-trailer model [53], which is of the same order as found in [42] and [12].

The drawback of boat tailing the base of the trailer is the required length of the boat tail, this can be up to 2 meters which is in conflict with current European legislation. The European legislation



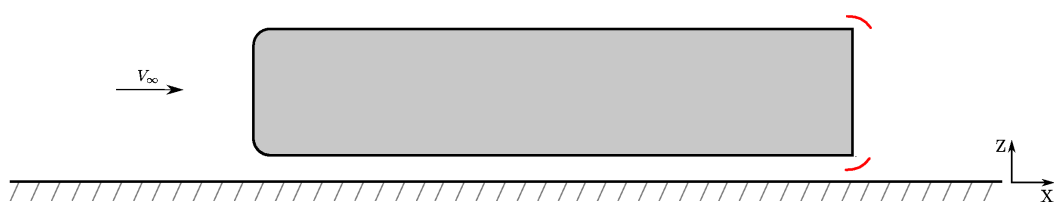
(a) Side view

(b) Rear view

**Figure 2.4:** Truck with boat tail

allows additional devices to extend for maximally 0.6 m behind the aft bumper and thus limits the possibilities for boat tails. In the United States however, this length is 1.5 meters and therefore it can be expected that boat tails will first appear in the United States. Furthermore the added length leads to practical constraints for truck drivers while maneuvering the tractor-trailer combination. Finally the boat tail is mounted on the cargo doors of the trailer, requiring the boat tail to be removed when loading or unloading the truck.

A more recently developed device for reducing base drag on trucks has been investigated by Van Straaten [56] in 2007. Guiding vanes are applied in the vicinity of the trailer base, under a angle of attack with respect to the surface of the trailer. The guided flow produced by the guiding vanes curves the shear layer inwards reducing the wake size and therefore increasing the base pressure, see figure 2.5. The drag reduction obtained for the GTS model as used in [56] is 25% in CFD computations and 21% in wind tunnel tests, which would lead to a reduction of fuel consumption of up to 10%.

**Figure 2.5:** Schematic representation of guiding vanes on GETS model

In [19] the application of transverse and longitudinal grooves and vortex generators to reduce base pressure drag is discussed. Both systems are aimed at generating vortices which close the wake more rapidly and thus reduce drag. Following that report, the application of vortex generators has been investigated in [20] on a bluff body with boat tail, however the results are not conclusive.

## 2.3 Coanda effect

The Coanda effect phenomena as described and patented by the Romanian H. Coanda [9] is the balancing effect between the centrifugal force and the pressure force in a wall bounded jet, causing the fluid jet to adhere to the wall surface, see figure 2.6. Although Coanda patented the phenomena the effect was first described by Young in 1800 [59] and had also been observed by others [43]. Applying this adherence effect with the effects of fluid entrainment, fluid motion can be influenced and this has been widely used in circulation control of airfoils.

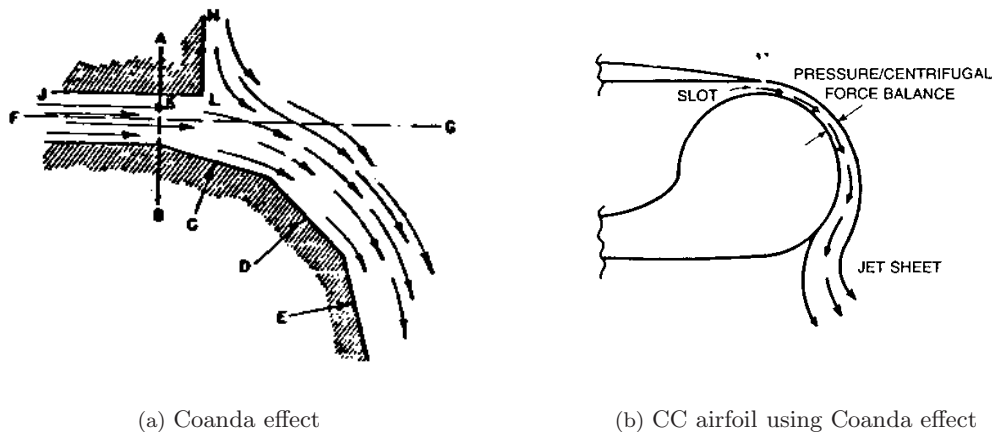


Figure 2.6: Coanda Effect

The Coanda effect is applied by tangentially blowing air along a highly curved surface in a region where separation would normally occur. Due to the entrainment of surrounding fluid with the blown jet and the Coanda adherence to the surface, the flow is guided along the surface, postponing or eliminating separation completely (see figure 2.6(b)). High blowing velocity experiments [14, 52] have shown 100% jet turning where the Coanda jet adheres to the surface until the jet flow separates while flowing opposite to the freestream flow.

Circulation control airfoils are developed since the 1930's and in the 1950's practical applications are mainly used for STOL (short take-off and landing) aircrafts due to their ability to significantly increase the lift coefficient [16, 41]. The increase in lift coefficient is due to the delayed separation and thereby increased circulation around the airfoil. Experimental wind tunnel tests with a STOL aircraft as conducted by Englar [41] even showed maximum angles of attack of 40 to 45 degrees and lift coefficients of 8.5 to 9 for the circulation control wing.

At Georgia Tech the research in the field of circulation control led to the first automotive applications, where the aim was drag reduction by reducing the wake size and thus reducing the base pressure drag. After experiments with road and race cars the attention shifted to trucks (see figure 2.3) due to the large percentage of base pressure drag. Wind tunnel tests showed drag reductions up to 50% [15] at relatively low blowing velocity for truck models.

The circulation control system for automotive applications generally consists of an add-on device which can be mounted to the back of the truck and is called an active flow control (AFC) system, as circulation control is intended to achieve more lift, whereas the purpose of the AFC system is to reduce drag. The system consists of a circular shape with a continuous circumference as displayed in figure 2.8



**Figure 2.7:** circulation control applied to a truck by Englar [45]

Another interesting result appeared to be the improvement of the stability and braking by enabling or shutting down the individual blowing slots. With this configuration also road tests were performed, however the high drag reductions achieved in the wind tunnel were not replicated during the road tests. In a presentation for the US Department of Energy the reduction of fuel consumption of a blown flap system using the Coanda effect is determined in a road test to be approximately 4% [45] and in [12] 5 to 6% is referenced, much less as claimed by Englar.

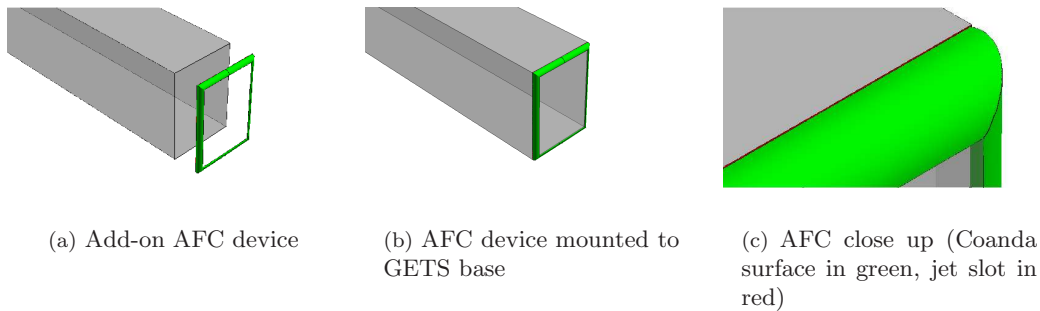


**Figure 2.8:** Conceptual add-on Active Flow Control device

In Europe similar research in Sweden with Scania [19, 46] has shown a decrease in drag coefficient of about 10 to 15% for a blown boat tail configuration. In this research, configurations were evaluated in a full scale wind tunnel and the results show in several configurations an increased drag coefficient opposed to drag reduction. In Germany an elaborate study of the Coanda effect on a 2 dimensional automotive bluff body [18, 21] showed a base pressure reduction of 50% and a corresponding reduction in drag coefficient of 10%. In this research the drawback of the power requirement for slot blowing is discussed impacting the final results.

### 2.3.1 Momentum coefficient

In circulation control aerodynamics the driving parameter is the momentum coefficient defined as equation 2.2 for a three dimensional flow (see appendix A.1)

$$C_{\mu} = \frac{\dot{m}V_j}{q_{\infty}A_{ref}}. \quad (2.2)$$

The momentum coefficient shows the ratio of momentum in the jet to a reference momentum (based on the frontal area of the truck in this research).

The blown jet influences the force balance by the components of the jet momentum and the effect of the jet on the actual flow field. For circulation control applications the driving influence is the effect of the jet on the flow field. Other systems where the jet momentum is more significant compared to the altered flow field are jet flaps, usually these systems require a high mass flow and therefor have a high energy consumption.

Another parameter of interest is the velocity ratio, defined as the ratio of the jet sheet velocity to the freestream velocity:

$$\zeta = \frac{V_j}{V_\infty}. \quad (2.3)$$

The maximum blowing velocity considered in the research is 75 m/s, as higher velocities require too much energy (see section 2.3.2), thus the flow can be assumed incompressible ( $M < 0.3$ ). Assuming incompressible flow (and  $\rho_j = \rho_\infty$ ), the momentum coefficient can be written using the velocity ratio as:

$$C_\mu = \frac{\dot{m}V_j}{q_\infty A_{ref}} = \frac{\rho_j A_j V_j \cdot V_j}{\frac{1}{2}\rho_\infty V_\infty^2 A_{ref}} = 2 \frac{A_j}{A_{ref}} \zeta^2. \quad (2.4)$$

Since the blowing mechanism will be applied on the complete outer contour of the truck, the slot length ( $L_j$ ) will be constant for all configurations; the slot area will only be changed due to the slot height, equation 2.4 can thus be written as:

$$C_\mu = 2 \frac{L_j h_j}{A_{ref}} \zeta^2, \quad (2.5)$$

where  $h_j$  is the slot height. In [15] it is indicated that varying slot height with constant  $C_\mu$  can have a significant influence on the results, therefor slot height variation is also evaluated in this research.

### 2.3.2 Energy balance

A common error made in blown aerodynamics is the fact that the net power consumption of the total aerodynamic system is dependent on the aerodynamic efficiency as well as the mechanical efficiency and the power used by the mechanical part of the blown aerodynamics, such as pumps etc. Since the blowing of air costs energy this must be included in the evaluation of the effectiveness of the aerodynamic device.

The total power required by the truck is equal to the sum of the frictional, mechanical and aerodynamic power. In this thesis the focus is on the aerodynamic power consumption, which is related to the drag of the vehicle and the power required by the blowing mechanism (the compressor), which can be expressed as:

$$P_{aero} = P_{aero, clean} + P_c. \quad (2.6)$$

As the total aerodynamic power is now related to the power used by the compressor ( $P_c$ ) a minimum aerodynamic power used might not be the solution which leads to the largest reduction in required power and thus lower fuel consumption. Using Bernoulli's equation and the pressure coefficient (equation A.18), the drag coefficient can be rewritten to include the power required of the compressor (for a complete derivation see A.2)

$$C_D = C_{D^*} + \underbrace{\frac{1}{\eta_c} \frac{A_j}{A_{ref}} \zeta (\zeta^2 + C_{p,j} - C_{p,i})}_{\text{Compressor power in terms of } C_D}. \quad (2.7)$$

With  $C_{D^*}$  the drag coefficient neglecting the compressor power consumption,  $C_{p,i}$  the pressure coefficient at the compressor inlet (1 for stagnation pressure) and  $C_{p,j}$  the pressure coefficient in the jet sheet aft of the jet slot. Without blowing the velocity ratio  $\zeta$  equals zero and thus  $C_D = C_{D^*}$ . For a derivation of equation 2.7 see appendix A and [21].

In [54] the total drag contribution of the back end of a complete truck model is determined as 35% of the total pressure and viscous drag force generated by the truck. As it can be assumed no aerodynamic tool will be able to create a complete base pressure recovery, the maximum energy required by the AFC system can be determined by setting the following requirement on drag contribution from the compressor in equation 2.7.

$$\frac{1}{\eta_c} \frac{A_j}{A_{ref}} \zeta (\zeta^2 + C_{p,j} - C_{p,i}) < 0.35 C_{D,GETS} \quad (2.8)$$

With  $C_{D,GETS}$  the drag coefficient of the clean GETS model. In figure 2.9(a) the compressor power in terms of  $C_D$  (the second term in equation 2.7) is plotted for increasing  $C_\mu$  and for  $\zeta$  in figure 2.9(b). The values for the slot height and compressor efficiency used for computing the  $C_\mu$  and  $\zeta$  are typical values based on [14].

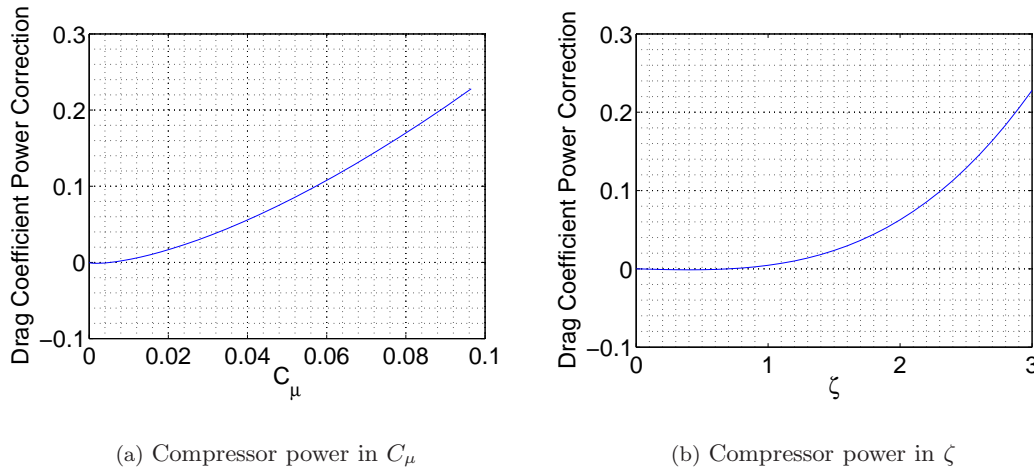


Figure 2.9: Compressor power

It can be seen in figure 2.9(a) that the compressor power in terms of  $C_D$  is larger than 0.1 for blowing coefficients higher than 0.06. For a slot height of 2 to 4 mm this corresponds to a maximum velocity ratio of 2 to 3, or a maximum jet velocity of 75 m/s, therefore the maximum velocity ratio is limited to 3 in this research. The flattened area in the graph of figure 2.9(b) is caused by the assumption that the jet and inlet pressure coefficient difference ( $C_{p,j} - C_{p,i}$ ) is approximately 0.4, this estimation is based on an inlet  $C_p$  of  $\sim 0.7$  and a jet  $C_p$  of  $\sim 0.3$ .

The window for the Coanda system to be energy efficient differs slightly with different slot height parameters and inlet and jet pressure coefficients, however the conclusion can be made that in order to have a reduction in the power required to overcome aerodynamic drag the momentum coefficient should not be chosen too high.

---

# Chapter 3

---

## Numerical Aspects

This research is based on the application of Computational Fluid Dynamics (CFD), which is used as a tool to evaluate different geometries and a reference model. CFD modeling consists of several elements, fluid modeling, solver algorithm and grid generation. The first two aspects are discussed in this chapter, grid generation is discussed in chapter 4.

### 3.1 Flow modeling

The fluid flow is numerically computed from the basic laws of conservation of mass and momentum. As for the low Mach number the compressibility effects can be ignored and the use of the energy equation can be omitted. The incompressible and steady conservation of mass and momentum can be expressed as

$$\nabla \cdot \mathbf{V} = 0 \quad (3.1)$$

$$(\mathbf{V} \cdot \nabla)\mathbf{V} = -\frac{1}{\rho}\nabla p + \nu\nabla^2\mathbf{V} \quad (3.2)$$

where equation 3.1 is called the continuity equation and equation 3.2 the Navier-Stokes equations for incompressible constant viscosity flow. Using these equations and the equations of state [57] the system of equations can be solved for incompressible flow. Unfortunately for engineering applications there are no exact solutions obtainable and hence a numerical discretization approach is used to solve the system of equations.

Fluent uses the Finite Volume Method (FVM) for the discretization of the governing equations in order to convert them to algebraic equations which are solved numerically. This technique uses control volumes which are defined by the model grid elements. The discrete values for the flow variables are stored in the cell centers by Fluent, however for the computation of the convective terms the cell face values are required and these are interpolated from the cell center values using an upwind scheme.

More details on the computation algorithm and the Finite Volume Method can be found in the Fluent manual [3] where a thorough description of the method is given. The selected options in Fluent are summarized in table 3.3.

## 3.2 Turbulence modeling

As this research is carried out with the readily available flow solver Fluent the options for possible flow modeling are limited to three viscous flow models which are suited for a high Reynolds number bluff body flow:

- Large Eddy Simulation (LES)
- Detached Eddy Simulation (DES)
- Reynolds Averaged Navier Stokes (RANS)

These three methods are based on two different approaches of turbulence modeling; filtering and ensemble-averaging. In both methods the Navier-Stokes equations are modified and additional terms and unknowns are created, which need to be modelled in order to close the model. This is known as the closure problem and remains a critical part in turbulence modeling.

### 3.2.1 Filtering versus statistical approach

**Filtering** is applied in the case of LES, where the large scale turbulence eddies are explicitly computed and the smaller scale eddies are modelled. The concept behind LES is that the large scale eddies are accurately captured, while the small scales, which are believed to be more isotropic and thus easier to model, are modelled instead. This results in most of the turbulence to be resolved, with the small scales left to be modelled.

**Ensemble-averaging** or Reynolds-averaging is based on the averaging of the Navier-Stokes equations using the definition of ensemble averaging:

$$\bar{u} = \lim_{N \rightarrow \infty} \frac{1}{N} \sum_{\alpha=1}^N u^{\alpha}. \quad (3.3)$$

The ensemble averaging allows the fluctuating turbulence properties to be written as an average and a fluctuating value:

$$u_i = \bar{u}_i + u'_i \quad (3.4)$$

$$\phi = \bar{\phi} + \phi' \quad (3.5)$$

for the velocity components  $u$  and the scalar quantities  $\phi$ . Substituting equations 3.4, 3.5 in the full Navier Stokes equation the following equation (after time averaging) is obtained:

$$\rho \frac{D\bar{\mathbf{V}}}{Dt} + \rho \frac{\partial}{\partial x_j} (\overline{u'_i u'_j}) = -\nabla \bar{p} + \mu \nabla^2 \bar{\mathbf{V}}. \quad (3.6)$$

In the latter the additional term for the turbulence inertia tensor is added to the mean momentum equation. This term can not be neglected and adds in total nine extra unknowns (the tensor unknowns) to the set of equations. The values of the the tensor are not only dependent on fluid properties but also on geometric, velocity and upstream conditions, making it very difficult to find a general solution for this additional term.

To gain insight on the nature of the turbulence tensor equation 3.6 can be rewritten as

$$\rho \frac{D\bar{\mathbf{V}}}{Dt} = \rho \mathbf{g} - \nabla \bar{p} + \nabla \cdot \tau_{ij} \quad (3.7)$$

by defining  $\tau_{ij}$  as

$$\tau_{ij} = \underbrace{\mu \left( \frac{\partial u_i}{\partial x_j} + \frac{\partial u_j}{\partial x_i} \right)}_{Laminar} - \underbrace{\overline{\rho u'_i u'_j}}_{Turbulent}. \quad (3.8)$$

This latter can be interpreted as if the total stresses on the system behave as Newtonian viscous stresses (laminar stresses) plus an additional term accounting for the turbulence stresses. The main dilemma remains to find appropriate values for the nine unknown tensor components which is the fundamental problem imposed by turbulence modeling.

Summarizing there are two methods for treating the effects of turbulence, filtering (LES) and ensemble-averaging (RANS). A hybrid version is in DES where the large scale eddies are resolved using LES and the small scale eddies by using RANS.

For this research the RANS method is used as it is widely used in engineering applications and the computational load compared to LES is smaller. As the design of the AFC device is expected to require several iterations the computational load is a constraint on the selected turbulence modeling.

### 3.2.2 Closure model

The nine unknowns resulting from the 'turbulence' tensor in equation 3.8 need to be solved in order to find a solution for the RANS equations. There exist two common methods to achieve this, both approaches are the corner stone of several different turbulence closure models. The first method is based on the Boussinesq hypothesis [35], where the turbulence stresses are related to the mean velocity gradients:

$$-\overline{\rho u'_i u'_j} = \mu_t \left( \frac{\partial u_i}{\partial x_j} + \frac{\partial u_j}{\partial x_i} \right) - \frac{2}{3} \left( \rho k + \mu_t \frac{\partial u_i}{\partial x_i} \right) \delta_{ij}. \quad (3.9)$$

This approach is used in the *Spallart-Allmaras*,  $k - \epsilon$  and the  $k - \omega$  models. In the latter two, additional equations are used to compute the turbulence kinetic energy  $k$  and the turbulence dissipation rate  $\epsilon$ , the turbulence viscosity is determined as a function of  $k$  and  $\epsilon$ .

The *Spallart-Allmaras* model is a one equation model, where the turbulence viscosity is solved. This model is effectively a low Reynolds number model suitable for wall bounded flows. The advantages of the *Spallart-Allmaras* model (as listed in [3]) are not required for this engineering case.

The  $k - \epsilon$  model exists in three versions;

- Standard  $k - \epsilon$
- RNG (ReNormalization Group)  $k - \epsilon$
- Realizable  $k - \epsilon$

The standard model is the oldest and the most basic version of the  $k - \epsilon$  group. The difference between the standard and the *RNG* model is the addition of several terms and equations to capture low Reynolds number effects and swirling flow effects more accurately. A more recent improvement on the *RNG* model is the *Realizable* model, which means the model satisfies certain constraints on the turbulence stresses, which are consistent with the physical properties of turbulence. One of the most important benefits of the *Realizable* model is the more accurate prediction of planar jet flows, which is relevant for this research. For more information about the individual differences between turbulence closure models and the mathematical formulation of the models see [3].

The  $k - \omega$  model is available in the standard and the shear-stress transport (SST) model. The standard model incorporates the Wilcox  $k - \omega$  model [3] and can be applied for wall bounded flows and free shear layers. The SST model is a blended model with the  $k - \omega$  formulation in close proximity to the wall and the  $k - \epsilon$  formulation away from the surface.

Opposed to the Boussinesq hypothesis the *RSM* (*Reynolds Stress Model*) uses transport equations for each term in the Reynolds stress tensor and one additional scaling equation for the turbulence dissipation rate. In total this model leads to seven more equations in  $3D$  which requires significantly more computing power. The strength of the RSM model lies in the fact that it is able to handle anisotropic turbulence opposed to the models based on the Boussinesq hypothesis. Still all the seven equations are closed by means of models, so the accuracy of the *RSM* model is still dependent on the quality of the individual models.

The computational time required is significantly higher for the *RSM* model compared to the  $k - \epsilon$  model. According to [3] the *RSM* model requires 50 – 60% more cpu-time per iteration and 15 – 20% more memory. This would mean double the computation time per simulation, assuming the same amount of iterations per computation, while due to the more complex coupling of the turbulence stresses and the mean flow the *RSM* model is expected to require more iterations.

Due to the improved handling of jet sheets of the *Realizable*  $k - \epsilon$  model compared to the other  $k - \epsilon$ ,  $k - \omega$  models and the one equation *Spallart-Allmaras* model the *Realizable* model is used in this research. The *RSM* is computationally costly and therefore at this moment not suitable for engineering practices.

### 3.3 Wall treatment

The influence of walls is significant on the result of turbulence CFD simulations. Not only does the wall influence the flow field, it also influences the turbulence properties due to near wall damping and kinematic blocking. The turbulence models need to be adjusted in close proximity to the wall in order to maintain their accuracy, which is the subject of this section.

Fluent (and others [35]) divides the turbulence boundary layer in three domains:

- Viscous sub-layer

The viscous sub-layer is the region close to the wall where the eddy viscosity goes to zero, leading to almost negligible turbulence stresses and thus nearly laminar flow.

- Buffer layer

In this layer the flow is dominated by viscous and turbulence stresses, neither of both are negligible, but the bias between both is unknown.

- Log-law layer

In this layer the turbulence plays a major role and the viscous stresses are negligible compared to the Reynolds stresses.

These three layers can be described using the friction velocity  $u_t$  and the dimensionless wall coordinate  $y^+$  which are defined as follows:

$$u_t = \sqrt{\frac{\tau_w}{\rho}}, \quad (3.10)$$

$$y^+ = y_c u_t \frac{\rho}{\mu}. \quad (3.11)$$

The three layers expressed in above parameters are shown in figure 3.1, which is based on experimental data and this relation is called the law of the wall. It shows from this figure that the following bounds exist for the three layers:

- Viscous sub-layer:  $0 < y^+ \leq 5$
- Buffer layer:  $5 < y^+ < 60$
- Log-law layer:  $y^+ \geq 60$

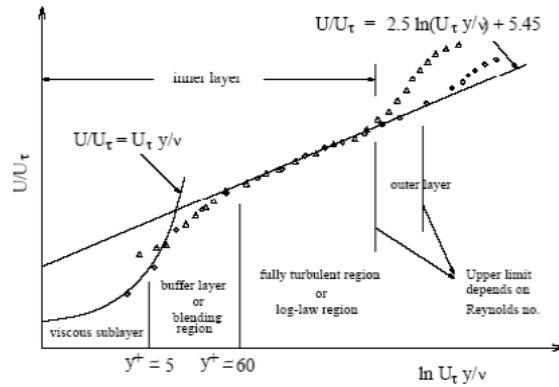


**Figure 3.1:** Dimensionless velocity profile for a turbulence wall flow

Based on this subdivision Fluent has two different approaches for the wall modeling; the *wall functions* and the *near wall model*. Both approaches treat the wall differently, both apply modifications to the turbulence model in use to simulate the effects of the presence of a wall. In case of wall functions the viscous layer and the buffer layer are not resolved, but are modelled instead. This leads to the advantage that the  $y^+ < 30$  region does not need to be meshed, but is modelled using information from the region  $y^+ > 30$ .

The main advantage for the wall functions approach is the reduction in the amount of required cells and it's fairly good performance in high Reynolds number wall bounded flows. Fluent recommends this model for most engineering purposes due to the robustness, the cost-effectiveness and the reasonable accuracy.

Two versions of the wall functions are available, the standard and the non-equilibrium wall functions. The non-equilibrium wall functions effectively relaxes the local equilibrium assumption (production equals dissipation) which is used in the standard wall function. The result is that the non-equilibrium wall function is more suitable for flows in adverse pressure gradients and to some extent separated and re-attaching flows.

The near wall modeling (enhanced wall treatment) approach resolves the viscous sub-layer given the constraint the mesh is fine enough to have cells in the  $y^+ \approx 1$  region. Fluent resolves the viscous sub-layer using a two layer approach used to resolve the turbulence dissipation and the turbulence viscosity in the near wall cells.

The first layer which is defined for the turbulence Reynolds number (equation 3.12) smaller than 200, in this layer the equations for  $k$  and the momentum equation from the chosen turbulence model are used, but the turbulence viscosity is computed from a one equation model. In the layer

where  $Re_y > 200$  the turbulence properties, including the turbulence viscosity are computed using the chosen turbulence model (in case of  $k-\epsilon$  and  $RSM$ ).

$$Re_y = \frac{\rho y \sqrt{k}}{\mu} \quad (3.12)$$

The lower layer viscosity is smoothly blended as a function of the turbulence Reynolds number with the second layer turbulence viscosity. For more details on the enhanced wall treatment see [3].

Summarizing the choice of wall functions is a compromise between cell count and accuracy. A typical near wall modeling approach requires twice to three times the amount of cells in the boundary layer compared to wall functions. In table 3.1 the differences and requirements of both methods are summarized.

	Wall Functions	Enhanced Wall Treatment
	Low Re flow	
Limitations	wall transpiration Separation and re-attachment Strong body forces Strong 3D near wall flow	Same limitations as chosen turbulence model
Grid Requirements	$y^+ \approx 30$ $30 < y^+ < 300$ No excessive cell stretching perpendicular to the wall	$y^+ \approx 1$ $y^+ < 4 \sim 5$ Minimum 10 cells in $Re_y < 200$ region

**Table 3.1:** Wall approach properties

Both types of wall modeling techniques are used in this research as both have their strong and weak points which differ per application. For the full GETS model the wall function approach is used; the total surface area covered with a boundary layer is larger compared to the model used for the AFC system making the cell count reduction significant. Furthermore the separation point on the GETS model is fixed; the flow separates at the base of the model and no separation is expected at the front edges of the model due to the selected radii.

For the active flow control system the enhanced wall treatment is used as the flow is dominated by separation and the boundary layer on the AFC system is strongly influenced by the tangential blown jet. This jet influences the boundary layer such that it is unlikely the wall functions will properly simulate these non-standard boundary layer shapes. As only the rear section of the GETS model is used in the Coanda system simulations the increase of cells in the boundary layer is acceptable.

### 3.4 Model setup

In this research three different types of simulations are performed, full scale simulations of the clean GETS body, full scale simulations of the last two stations of the GETS model including various AFC systems and the clean GETS body in wind tunnel conditions at various yaw angles.

The wind tunnel simulations are performed at an 1 : 15 scale conform to the model dimensions from [55]. The boundary conditions for these simulations differ from the full scale simulations due to the wind tunnel environment and the different requirements on the Reynolds number.

In figure 3.2 the domain is shown with the different surfaces and the boundary conditions set at these surfaces for both the full scale GETS model and the wind tunnel model. In the wind tunnel

model the floor underneath the model which extends fore and aft of the model has a different boundary condition compared to the full scale model. For the simulations of the Coanda system the same boundary conditions are used as for the full scale GETS model, except for the inlet condition.

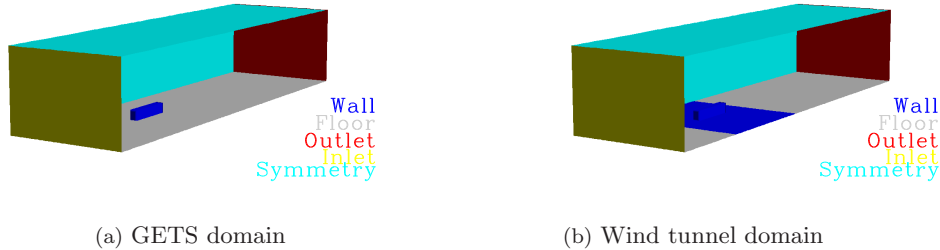


Figure 3.2: Boundary conditions on simulated domains

The full-scale simulations are performed at a vehicle velocity of 25 m/s (90 km/h) according to the average highway speed (including wind) found in [54] leading to a Reynolds number of  $4.5M$  based on the width of the model. According to [1] the Reynolds number based on the width in a wind tunnel environment should be at least  $0.7M$ , the wind tunnel scale model is simulated at a velocity of 60 m/s fulfilling this requirement.

### 3.4.1 Boundary conditions

In order to simulate the flow field around the model the freestream velocity is set equal to the driving speed of the truck, the inlet plane is set as a *velocity inlet* with a 25 m/s for the full scale and 60 m/s for the wind tunnel simulations. The AFC simulations use a velocity profile set at a distance  $2w$  ahead of the base of the model. The velocity profile is obtained from the simulations of the clean GETS model. The location of the model cut for the AFC simulations is determined from the pressure on the GETS model and is discussed in section E.1.3.

The turbulence conditions at the velocity inlet are set, Fluent requires boundary conditions for the turbulence production  $k$  and the dissipation  $\epsilon$ . It is more common to prescribe the turbulence intensity level  $I$  and the turbulence length scale  $\ell$  instead of  $k$  and  $\epsilon$  using the following equations [3]:

$$I = \frac{u'}{\bar{u}}, \quad (3.13)$$

$$k = \frac{3}{2}(u_{avg}I)^2, \quad (3.14)$$

$$\epsilon = C_\mu^{\frac{3}{4}} \frac{k^{\frac{3}{2}}}{\ell}. \quad (3.15)$$

The turbulence intensity is strongly influenced by the atmospheric and environmental properties. For instance the turbulence intensity will be high when the truck is driving in the wake of other traffic. In [7] and [3] highly turbulence flow is referred to as  $\sim 10\%$ , in [8] the effects of freestream turbulence on several bluff bodies is investigated showing for a smooth front, long bluff body (similar to the GETS model) a small effect of the freestream turbulence on the base pressure. A turbulence intensity of 5% is used for the freestream conditions in the full scale simulations and for the wind tunnel simulations a value of 1% is used from [31].

The turbulence length scale is defined as the length scale of the eddies which contain the most energy in the turbulence flow. The macro scale (the largest turbulence scales) contain the highest level of energy which is dissipated as the large eddies break down to smaller eddies. The largest scales for the GETS model are expected to be in the range of half the width of the model, which is in the order of the size of the vortex core. For the velocity inlet of the Coanda jet the hydraulic diameter concept [57] is used. The length scale can be determined using:

$$\ell = 0.07 \frac{4A_j}{A_{wet}}, \quad (3.16)$$

using the definition of the hydraulic diameter from [57]. This leads to a length scale for the velocity inlet of the Coanda jet of approximately 0.0015 m.

The outlet boundary condition for the model is set as a *pressure outlet*, with the outlet pressure set to static pressure. Although the velocity profile is not known at the outlet boundary the static pressure is expected to have recovered to freestream values at the location of the outlet boundary condition

The side, top and the symmetry plane of the domain is set as a *symmetry plane* defining a slip condition at these surfaces. The velocity and gradients normal to the symmetry plane are set to zero which prevent fluxes through the symmetry surfaces.

The GETS model and the Coanda surfaces are given a wall boundary condition which means the normal and tangential velocities are set to zero. The floor is simulated with different conditions, the fixed wall, moving wall and the symmetry condition are compared to each other (see section 5.4) as the boundary conditions are different between the real case and the wind tunnel model. Furthermore different grid requirements are valid for the different boundary conditions. In case of the wind tunnel simulations the floor is split in two boundary conditions. Far upstream and downstream of the model the floor is set to a symmetry plane, while underneath the model a fixed floor is imposed, which is related to the geometrical layout of the wind tunnel (see section 5.6).

In table 3.2 the boundary conditions are summarized.

Surface	Boundary condition	Additional properties
Inlet	Velocity inlet	$I = 5\%$ , $\ell = 1.3m$
Coanda Jet Inlet	Velocity inlet	$I = 5\%$ , $\ell = 1.5mm$
Outlet	Pressure outlet	
Side / Symmetry	Symmetry plane	
Top	Symmetry plane	
GETS	wall	
Coanda Surfaces	wall	
Floor	Moving wall / Stationary wall / symmetry	

**Table 3.2:** Boundary conditions

### 3.4.2 Solver settings

Fluent is set-up using an implicit segregated solver, which is recommended for incompressible flow. The segregated solver solves the equations for mass and momentum conservation and the turbulence quantities sequentially. The coupled solver can also be used in Fluent, however, this was originally developed for compressible flows and requires more memory. Since the flow around the GETS model is incompressible the segregated solver is preferred.

In order to improve the convergence speed and stability the iteration process is carried out using different settings. Under relaxation of the momentum and turbulence quantities can be used to

stabilize and accelerate the solutions. Under relaxation for a quantity  $\phi$  is defined as:

$$\phi = \phi_{old} + \alpha_{urf} \Delta\phi, \quad (3.17)$$

where  $\alpha$  is the under relaxation factor (URF). The under relaxation reduces the change in  $\phi$  ( $\Delta\phi$ ) produced during the iteration. If this change becomes too large the solution can become unstable, which is usually encountered in the first iterations. It must be noted that if  $\alpha$  is chosen too small it can take many iterations before convergence is met, or the solution may appear to be converged as the relative change is small, while it is not yet converged.

The convergence of the solution is based on the drag coefficient and the residuals of the mass conservation and the three velocity components. The residuals are determined by fluent by summing the individual cell residuals and scaling them to a representative flow rate through the domain [3]. Using the double precision method in Fluent the minimum residual is in the order of  $10^{-12}$ , however, in practice values of the residuals are of the order  $10^{-8}$ .

The solution will not converge to a fully stationary solution due to the time-dependent phenomena which are present in the flow field (see section 2.1.1). The residuals and the drag coefficient will therefor oscillate around their mean value and the amplitude of the oscillation is a indicator of the magnitude of the unsteady effects. As the unsteady forces are expected to be small compared to the forces working on the truck the solution can be averaged in order to reduce the computational costs.

To improve the stability and the convergence of the solution process the solver is set to different discretization schemes after a certain amount of iterations. The process is started with first order upwind schemes which are more diffusive compared to second order schemes, which damp strong gradients which occur in the first iterations. The pressure velocity coupling is changed from *SIMPLE* to *SIMPLEC* as this is more accurate. The under relaxation factors are gradually increased during the iteration process from very stable (close to zero) to fast converging (close to 1). In table 3.3 the solver settings are summarized.

Iterations	1 – 50	51 – 150	151–Convergence
Pressure discretization	Standard	Standard	Standard
Momentum discretization	1 <sup>st</sup> order	1 <sup>st</sup> order	2 <sup>st</sup> order
$k$ discretization	1 <sup>st</sup> order	1 <sup>st</sup> order	2 <sup>st</sup> order
$\epsilon$ discretization	1 <sup>st</sup> order	1 <sup>st</sup> order	2 <sup>st</sup> order
Pressure-Velocity coupling	<i>SIMPLE</i>	<i>SIMPLE</i>	<i>SIMPLEC</i>
Pressure URF	0.5	0.65	0.65
Momentum URF	0.2	0.35	0.7
$k$ URF	0.2	0.5	0.8
$\epsilon$ URF	0.2	0.5	0.8

**Table 3.3:** Summarized solver settings

Before the iterations are started the grid is renumbered to increase the memory access efficiency and speed up the solution process. The grid is split in separate zones for parallel computing using the *Metis* [3] based on suggestions of a Fluent user from the aerodynamics department. The initial conditions are set to zero as recommended in [30].

The solution is iterated until the drag coefficient converged till within one drag count which typically required approximately 10,000 iterations, while the AFC system simulations required, varying per case, approximately 12,000 iterations due to the more complicated geometry. Convergence is based on the drag coefficient as this is the primary quantity of interest in this research. The momentum and turbulence quantities converged to values below  $10^{-6}$  before the drag coefficient converged.

### 3.5 Numerical diffusion

An error present in CFD simulations is the presence of numerical diffusion in the discretization schemes. Numerical diffusion is the result of non-alignment of the cells with the flow and the discretization of the convective terms in equation 3.2. The discretization of the convective term leads to a formulation which can be interpreted as a diffusive term, which is the result of the discretization itself.

Numerical diffusion becomes more significant when the actual diffusion becomes smaller compared to convection, which is in the case of high Reynolds numbers. As the flow over a truck is governed by high Reynolds number flow, the effect numerical diffusion is of interest in this thesis research.

All practical forms of numerical discretization lead to some numerical diffusion and the applied Fluent second order scheme [3] is tested in this section for its sensitivity to numerical diffusion. A laminar, two dimensional flat plate flow is simulated on a dense grid for increasing Reynolds numbers. A laminar boundary layer is used as the turbulence model does not influence the convective discretization and related numerical diffusion. As the theoretical solution for the laminar boundary layer thickness is known from [57] the simulated boundary layer thickness at the end of the plate is expected to be proportional to  $\frac{1}{\sqrt{Re}}$ . The Reynolds numbers tested range from  $0.1M$  to  $35M$  and the boundary layer thickness is defined as  $\delta = 0.99 \frac{u}{U_e}$ .

In figure 3.3(a) the boundary layer thickness for increasing Reynolds numbers compared to the theoretical values is shown and a more detailed view is shown in figure 3.3(b).

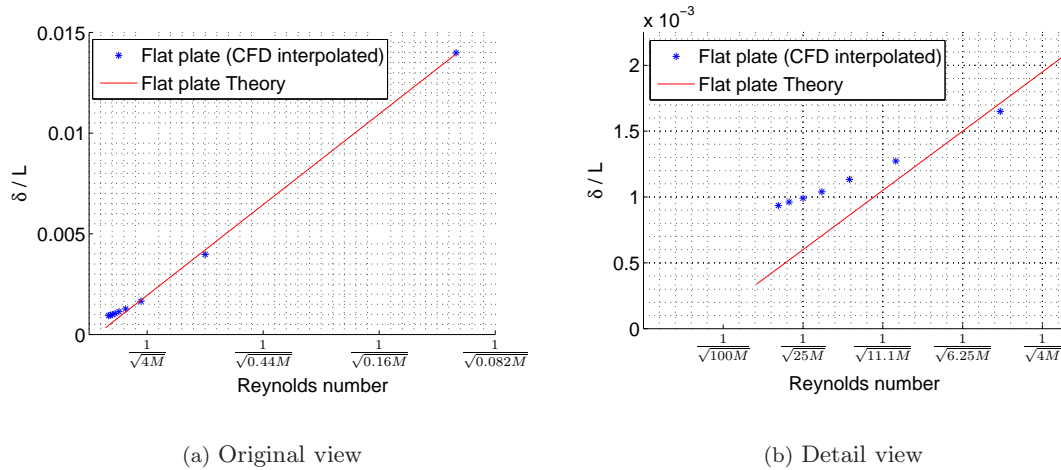


**Figure 3.3:** Theoretical and simulated and interpolated boundary layer thickness

As can be seen in both figures the effect of numerical diffusion is visible for increasing Reynolds numbers. From  $Re = 10M$  the simulated boundary layer thickness deviates from the theoretical value and the discrepancy increases for increasing Reynolds numbers. As the Reynolds number is increased more the simulated boundary layer thickness does not decrease proportionally. The cell sizing used is half the maximum cell size which will still allow a  $y^+$  value of 30 for the GETS grid, which is  $0.7 \text{ mm}$ .

It can be concluded that the required cell spacing to properly predict the boundary layer thickness at the base of the full scale GETS model is smaller than is allowed for the application of the wall functions. The resulting boundary layers therefor will be effected by numerical diffusion and the boundary layers will be thicker in the (full scale) simulations as would be the case if numerical diffusion would not be present.

---

# Chapter 4

---

## Grid Generation

For the creation of the computational domain the commercial grid generation software IcemCFD has been used. IcemCFD is like Fluent a product of the Ansys group, which leads to good compatibility between both products. Furthermore IcemCFD has been used to generate the grid due to the possibility to use input files for the generation of the geometry and the grid, leading to a more automated grid generation procedure.

### 4.1 Parametric approach

An important feature of the IcemCFD software is the possibility to record and replay the commands used in the program while making the geometry and grid. The internal command language used in IcemCFD is the open source language TCL (Tool Command Language) developed from 1988 at Berkeley [58].

Building grids can be very time consuming; in general building the grid requires more time than the actual computation of the flow solver. Especially in an engineering environment where many different geometry parameters are of interest the time spent building grids can be enormous. This is where parameterization can play an important role when the complete geometry is parameterized. When the geometry can be created by the software by running a script file instead of manual input the process of building the geometry takes seconds instead of hours.

The same holds for the computational grid, many grid properties are varied during the design process for grid refinements in order to achieve a grid independent solution. Also the grid has to be reshaped as the geometry changes leading to a time consuming process when many different geometries are to be analysed.

The parameterization approach can be split in several parameters, a full overview can be found in table B.1 in appendix B. The parameters can be divided in four groups:

**Geometric parameters** As only the dimensions of the geometric parts on the AFC device are changed in this research, the shape topology remains the same, making grid parameterization possible. Furthermore the GETS model can be altered for (future) simulations with different  $L/W$  or  $W/H$  ratios, different front radii and ground clearances allowing the analysis of different shape families. Besides the model dimensions also the domain (section 4.2) can be modified for different blockage ratios and model positioning with respect to the inlet and outlet boundaries.

**Grid topology parameters** The shape of the grid blocks can be modified to shape the structured grid such that it is more accurately aligned with the flow, in case of the boundary layer on the AFC grid (section 4.4) and the expansion ratio of the jet sheet boundary layer grid (section 4.4.2). Furthermore the size of the boundary layer grid, the length of the wake and the size of the wake box can be modified using the parameterization.

**Grid density and refinement** The amount of cells, cell growth and initial cell sizing is variable in each grid block and determines the total amount of cells used in the final grid. Most of the cell spacing settings for each geometric part are related to settings on connected geometries, as the smoothness (section C.2) and aspect ratio (section C.2) requirements lead to constraints on the allowable cell sizings. For example, a rectangular quadrilateral element has a length  $a$  and a width  $b$  which both can be varied by defining them as parameters, however, the aspect ratio requires that  $\frac{1}{5} < \frac{a}{b} < 5$ , thus constraining  $a$  in terms of  $b$  or vice versa, see section C.2 in appendix C.

**Grid smoothing and quality** After the construction of the grid smoothing and other techniques [4] can be applied to improve the grid quality. The quality improvement method and amount of smoothing iterations can be varied in the grid generation process.

The grid is created using multiple script files each performing a part of the grid generation process. The different steps are shown in figure 4.1, details on the different steps are discussed in section 4.2.1.

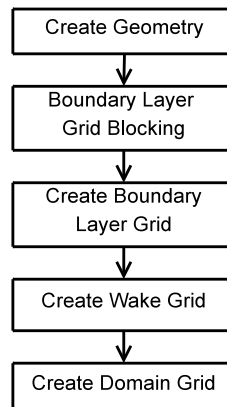


Figure 4.1: Script files structure

Using the script files the grid generation process from geometry input to a grid ready to be read by Fluent requires approximately 30 minutes of computation time for a 6 million cell grid on an ordinary workstation. Comparing this to the amount of time spent generating grids manually automating the grid generation process allows for more design iterations in less time.

## 4.2 Numerical domain

The GETS model is bounded by an outer domain defining the outer perimeter of the numerical domain. As the stagnation pressure on the front of the model develops upstream the numerical domain should extend upstream far enough for the total pressure to develop in front of the model and from [50] a length of eleven times the body width is advised. For practical reasons an inlet length is chosen at eight times the body width, leading to equivalent dimensions as in the referenced paper due to the model dimensions. As this thesis mainly focuses on the wake behavior and the resulting drag, the length of the domain aft of the model is of influence on the

results. From [30] the minimum aft domain length should be five times the vehicle length. As this guideline refers to a car model, for the longer GETS model five times leads to an unwanted large increase in cell count, therefore a ratio of four times the model length is used or 25 times the width.

For truck aerodynamics the use of the truck width is more practical as the influence of the length of the model is less significant opposed to the width of the model on the drag coefficient. Therefore the dimensions will be expressed in terms of truck width instead of truck length in this thesis.

Similar to a wind tunnel environment, a numerical domain suffers from the blockage effect. To avoid these effects having significant influence [30] recommends a blockage ratio of 1% to 1.5%. This leads to a domain width of  $8w$  and an domain height of  $11w$ . The complete domain is shown in figure 4.2.

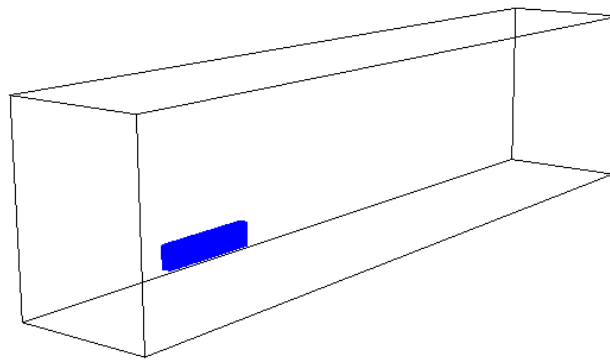


**Figure 4.2:** Overview of domain including GETS (half) model

Most of the simulations are performed with the model at zero yaw angle with an uniform inlet flow field. As the boundary conditions are symmetric and since time averaged Navier Stokes equations are used it is assumed a symmetric flow field will develop (with a symmetric grid). Due to the flow and model symmetry a half model of the GETS can be used, leading to a reduction of cells by a factor of two. This results in a significant reduction in simulation time and leads to the ability to apply grid refinements in significant areas. The assumption of symmetric flow will be further discussed in 5.3.

The chosen domain size is proven to be sufficient in figure 4.3 where a plot of the absolute pressure coefficient ( $|C_p|$ ) at a modified plotting scale is shown. The pressure is nearly fully recovered aft of the model and in front of the model the pressure is less than 1% higher compared to the undisturbed pressure.

### 4.2.1 Grid blocks

The GETS grid itself consists of several different blocks and grid types, to have more influence on the grid density and different element types. By using a hybrid mesh the different elements can be used in areas where specific types are most suited as discussed in section C.1.

For the complete GETS grid the following areas can be distinguished:

- Structured boundary layer grid
- Unstructured dense wake grid

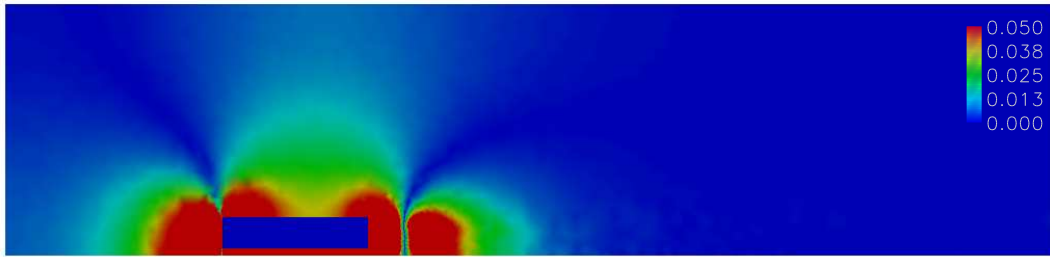


**Figure 4.3:** Absolute pressure coefficient in symmetry plane of GETS model

- Prism layer on the domain ground (for some GETS grids)
- Unstructured coarse outer domain

The structured boundary layer grid is used to keep the grid aligned with the flow and to have precise control over the cell spacing on the surface and in the boundary layer. All the individual surfaces which form the GETS and the AFC model have a squared topology; there are always exactly four edges that make up one surface. This means that a full quadrilateral surface mesh can be mapped onto both geometries. Also a structured grid allows for more control over the  $y^+$  values required for the wall treatment.

Because the most salient flow features are found in the wake of the model the grid requires refinement in this area. Also the area just outside the boundary layer requires a dense grid in order to match the boundary layer grid to the outer domain grid. From [48] the wake closes between  $1.5w$  and  $2w$  behind the base, in the domain a refinement box has been placed around the model extending  $3.5w$  behind the base of the model as can be seen in figure 4.4. Tetrahedral elements are used in this enclosure because flow alignment of the elements is not possible due to the chaotic nature of the wake and the unstructured elements allow for refinements in specific area's without causing unwanted refinements elsewhere.

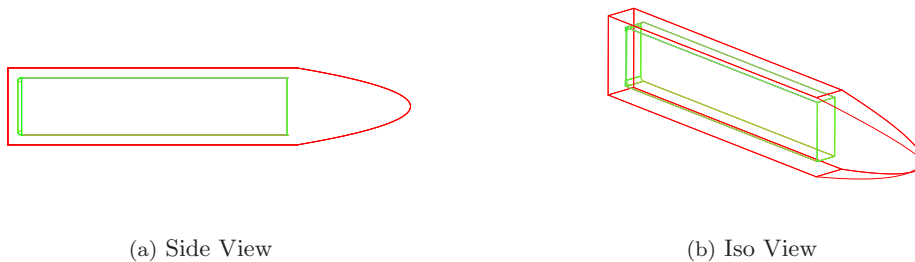


**Figure 4.4:** Wake enclosure (red) for GETS-half model (green)

Simulations employing a prism layer on the floor of the domain have also been carried out to analyse the effects of a stationary and a moving wall boundary condition. A prism layer is most suited for this application, since covering the complete floor in quadrilateral elements would lead to a unrealistic amount of cells and computing time. More details concerning the prism layer in section 4.3.2.

The domain between the wake enclosure and the domain boundary is filled with tetrahedrals as no large gradients are present in this area and an unstructured grid can fill the domain with a minimum amount of cells, reducing computational costs.

## 4.3 GETS grid

The GETS model consists of the base geometry covered with a boundary layer grid placed in the wake refinement box. The connection between the two different topology grids is made by a pyramid layer, used to connect hexahedrals to tetrahedrals.

### 4.3.1 Boundary layer grid

As for the GETS model non-equilibrium wall functions are used the  $y^+$  values are required to stay within the  $30 < y^+ < 300$  range for the wall functions to remain valid. Using an estimate for the skin friction coefficient the minimum cell height can be determined. For the estimation of the skin friction coefficient and the thickness of the boundary layer the top, bottom and side of the GETS is assumed to be similar to a turbulent flat plate. From [57] the turbulent boundary layer thickness and the skin friction coefficient for a flat plate is estimated as:

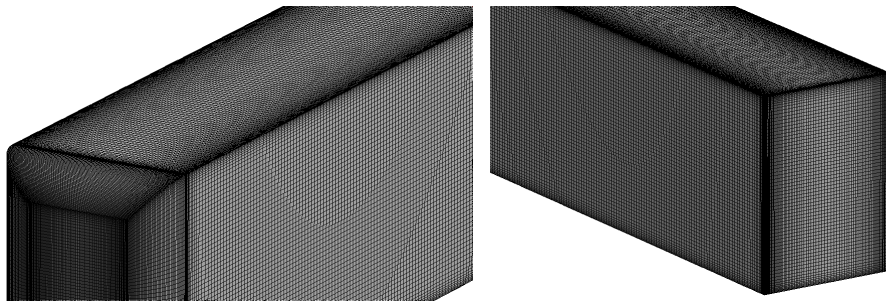
$$\delta(x) = \frac{0.37x}{Re_x^{\frac{1}{5}}}, \quad (4.1)$$

$$C_f = \frac{0.074}{Re_c^{\frac{1}{5}}}. \quad (4.2)$$

Leading to an estimate for the skin friction coefficient and using equations 3.11 to 3.10 this yields a minimum first cell height of 1.4 to 14 *mm*. The boundary layer thickness at the end of the GETS model is estimated to be approximately 200 *mm*, therefore the structured grid height used is 250 *mm*. A higher unstructured grid proved to be impractical due to interference with the prism layer at the bottom of the model. Sufficient space for the connection with the unstructured elements proved necessary to maintain grid quality.

In figure 4.5 the front end curvature surface mesh is shown as well as the surface mesh on the model base for a medium sized grid. Grid refinements can be seen on all the edges of the geometry in order to capture the more complex flow details on the edges. The boundary layer grid and several wall height details on the symmetry plane are shown in figure 4.7.

On the rounded surfaces on the front end of the GETS model an O-grid [4] is created to fully align the flow with the grid. For the grid close to the base two possible topologies are considered, both are shown in figure 4.6.



(a) Surface mesh on the front end curvature

(b) Surface mesh on the base

**Figure 4.5:** Surface mesh details of GETS-half model

The three sector approach leads to perfect flow alignment in the boundary layer and refinements for the first part of the shear layer. However, the additional grid block leads to a dense grid where



**Figure 4.6:** Grid topologies

the structured grid is connected to the unstructured grid. With the large spacing differences the growth ratio of the pyramid element's base (used to connect the two grids) becomes too large leading to very low quality of the important connection elements.

The two sector approach (similar to an O-grid) leads to less refinements in the shear layer and slightly skewed cells but allows the pyramid elements to have a higher quality. Furthermore the element height in the boundary layer can be modified without influencing the spacing on the grid connection. The two sector grid is used for the GETS model, with increased cell density in the shear layer. The element skewness in this part of the grid is maximum 0.3, which is below critical values as described in section C.2.

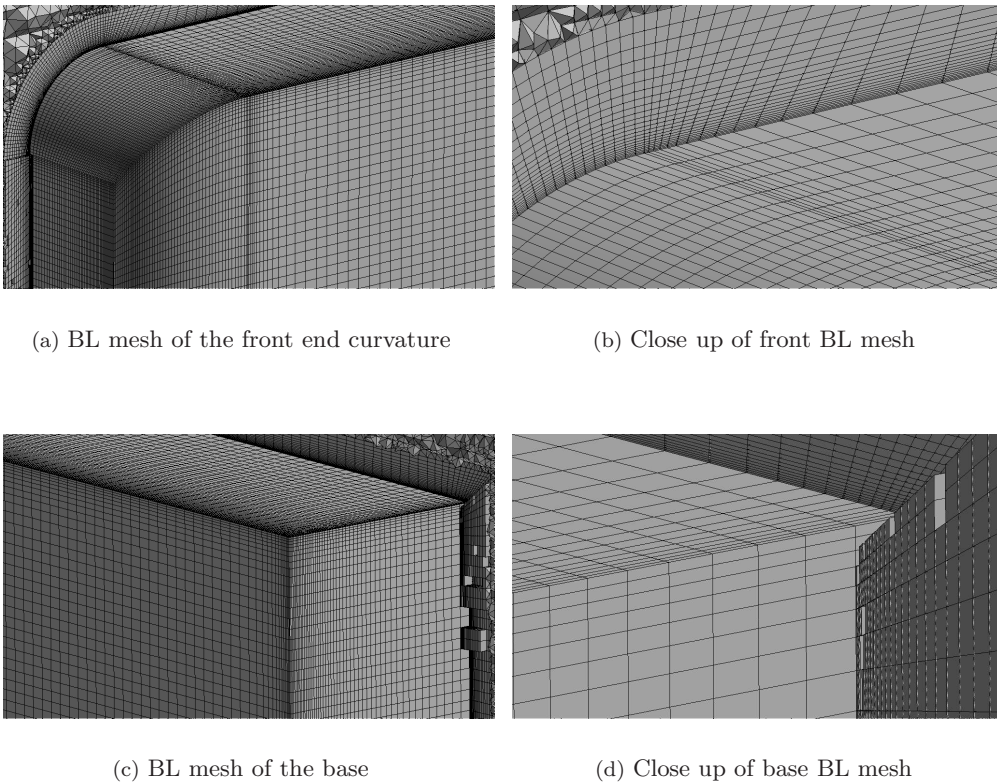


**Figure 4.7:** Boundary layer mesh of GETS-half model

### 4.3.2 Unstructured grid

The structured boundary layer grid is connected to the refinement box (as shown in figure 4.4) by pyramid elements. An overview of the refined grid around the GETS model is shown in figure 4.8. A close up view can be found in figure 4.9.

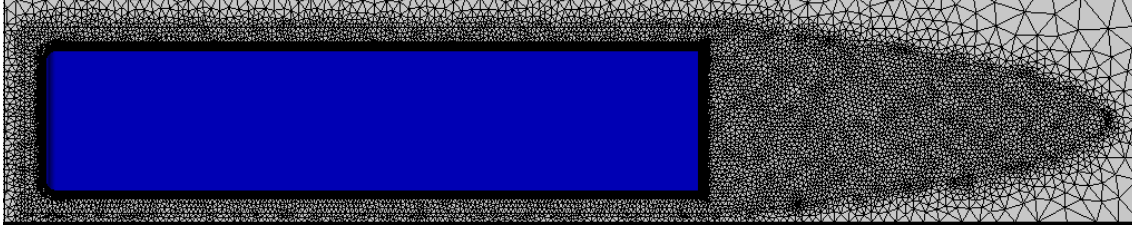


**Figure 4.8:** Grid refinements around GETS Model in symmetry plane

The GETS model is simulated with several different floor boundary conditions. As most automotive applications require a moving floor due to the small ground clearance [8] it is worthwhile to analyse the actual differences. Most wind tunnels are not equipped with a moving floor and simulating a floor where a boundary layer can develop requires more computation time due to the additional required boundary layer cells.

For a moving floor boundary condition a floor boundary layer will develop and thus requires a grid suitable to capture this. Due to the large size of the domain floor a structured boundary layer is not feasible, therefore a prism layer is extruded from the unstructured floor mesh. The first cell height is calculated in a similar manner as for the GETS boundary layer and the surface mesh is extruded over five layers, as recommended in [3, 30]. In figure 4.9 the prism floor underneath the front of the model can be seen; note the five structured layers under the unstructured grid.

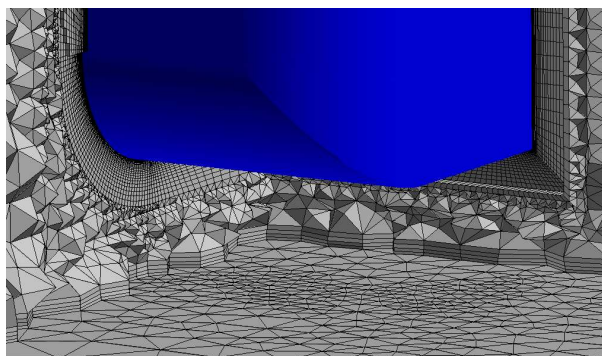


**Figure 4.9:** Prism layer under the GETS Model

The wake refinement domain and the prism floor are connected by tetrahedrals and these elements fill the rest of the domain. Their maximum size is limited to 2 meter on the inlet and outlet surface with a growth ratio in the domain of 20%. In figure 4.10 an overview and some grid slices are shown illustrating the full domain grid.

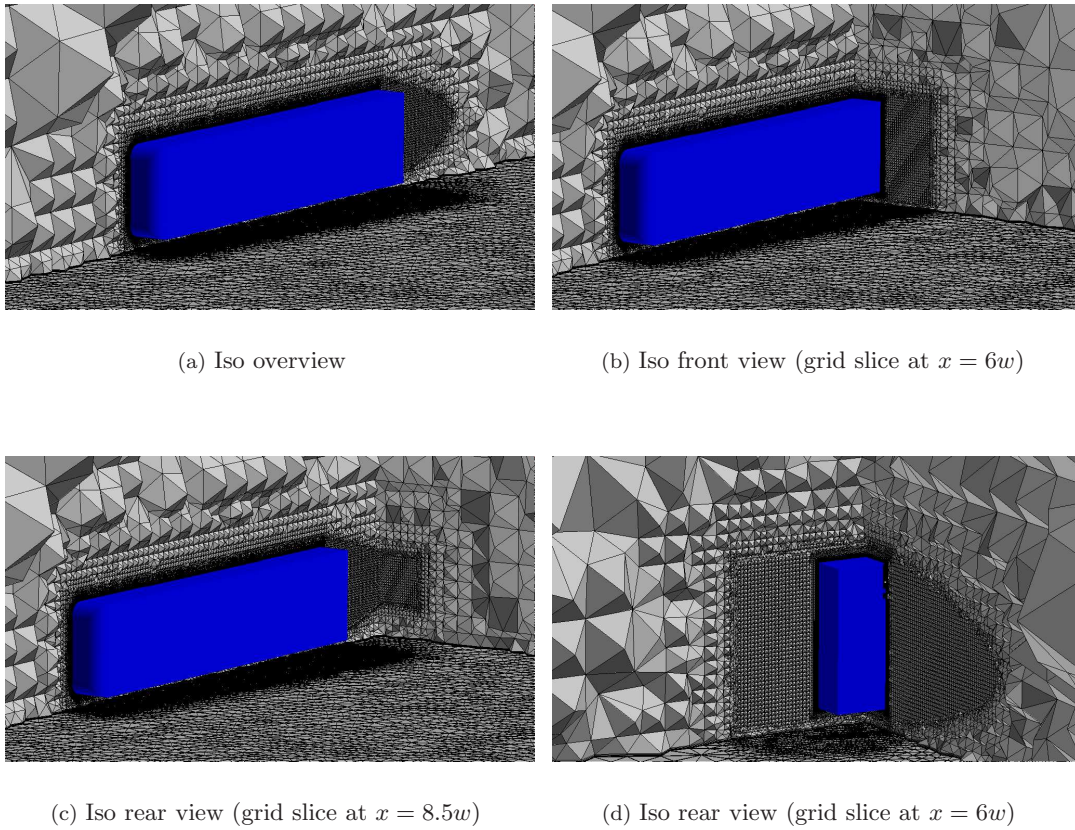


**Figure 4.10:** Domain grid overview of half model

A typical GETS grid constructed as described above consists of the following element type distribution as tabulated in table 4.1, also the distribution of elements in each grid block is shown.

Type	Percentage	Grid Block	Percentage
Hexahedral	23.4 %	Boundary Layer	23.4 %
Tetrahedral	75 %	Wake Grid	48.1 %
Prism	0.6 %	Floor	0.6 %
Pyramid	1 %	Domain	27.9 %

**Table 4.1:** Element and type distribution for GETS model

With differently sized grids and local refinements the distribution will differ slightly, however most grid modifications are made by increasing the amount of cells in each grid block by the same relative amount. This is preferred in order to keep grid qualities like aspect ratio and smoothness consistent.

## 4.4 Active Flow Control grid

The aerodynamic tool studied in this thesis is mounted to the base of the GETS model, although it can be added to the geometry, a new grid has to be created for the modified model. Due to the more complex geometry and the near wall approach (see section 3.3) a large increase in the amount of cells is expected. To reduce the amount of cells only the aft part of the GETS model is modelled. A velocity inlet is placed  $2w$  ahead of the base with the inlet conditions obtained from the full model simulations. This reduced the amount of cells of the model without the circulation control grid by nearly 70% compared to the full model. Although the base pressure will influence the upstream pressure, it is assumed that this effect is negligible  $2w$  ahead of the base. This assumption and the implications on the solution will be further discussed in E.1.3.

The formation of the grid is parameterized as in the GETS model case, and the geometry used to describe the grid is shown in figure 4.11 with the following parameters:

- $R_1 = R_2 = 0.115w$
- $H = 0.00154w$
- $\theta = 90deg$

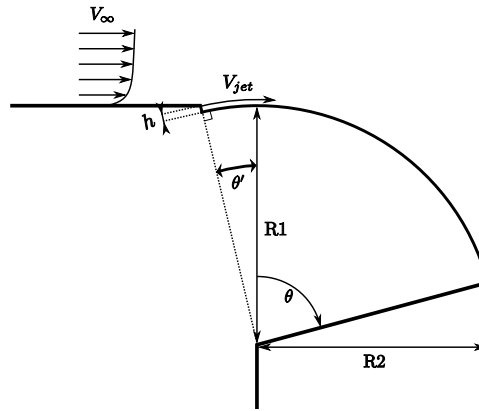


Figure 4.11: AFC geometry definitions

The angle  $\theta'$  is calculated from relation 4.3 such that (1) the velocity inlet is perpendicular to the radius  $R_1$  and (2) the inlet height  $h$  is as specified in the input file:

$$\cos \theta' = \frac{R_1}{h + R_1}. \quad (4.3)$$

The same grid topology for the AFC device is used as for the GETS model. A structured hexahedral boundary layer grid, connected to an unstructured wake grid with dense tetrahedrals. The outer domain has the same length aft of the base and the same blockage ratio is used to determine the width and the height of the outer domain. An overview of the model and model domain are shown in figure 4.12. The only difference compared to the GETS grid is the absence of a prism layer floor. This will be discussed in section 5.4.

### 4.4.1 Velocity inlet geometry

In practice the velocity inlet on the AFC device will consist of a plenum area where the compressor creates a high pressure and a velocity outlet where air flows through. In the plenum area the pressure is regulated controlling the velocity and hence the momentum coefficient.

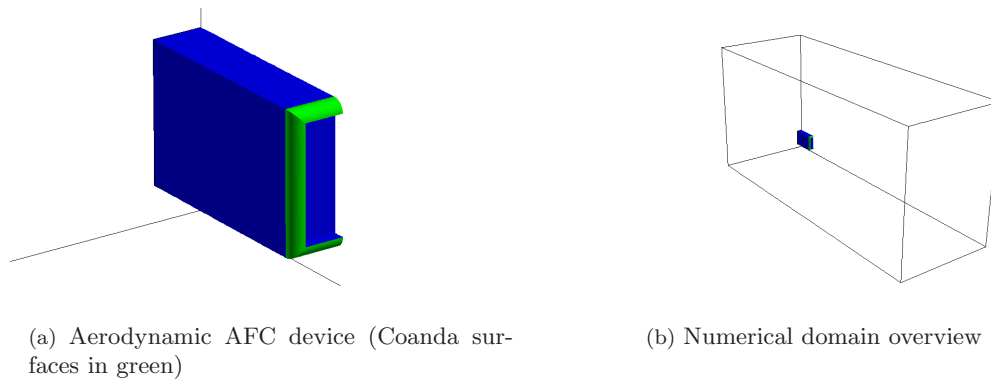


Figure 4.12: Half AFC model in rear iso view

In past numerical studies concerning circulation control systems there are several approaches used to model the velocity control, mostly used is the approach where the plenum is fully modelled [17, 37, 52] and the pressure in the plenum is varied till the required momentum coefficient is obtained. Schematically the approach is shown as *Geometry A* in figure 4.13.

A more simple approach is shown as *Geometry B* in figure 4.13. This layout is more simple to model and it requires less elements. Furthermore this geometry represents a possible practical application on a real truck the most, as the device would be most likely attached to the existing base of the truck as an add on device.

*Geometry C* in figure 4.13 shows a combination of above discussed geometries. The internal plenum is not modelled, a velocity is specified at the inlet face. The plenum ramp is modelled as after simulations with *Geometry B* the flow showed unrealistic behavior. The Coanda jet exiting the velocity inlet never attached to the Coanda surfaces, causing immediate separation from the model.

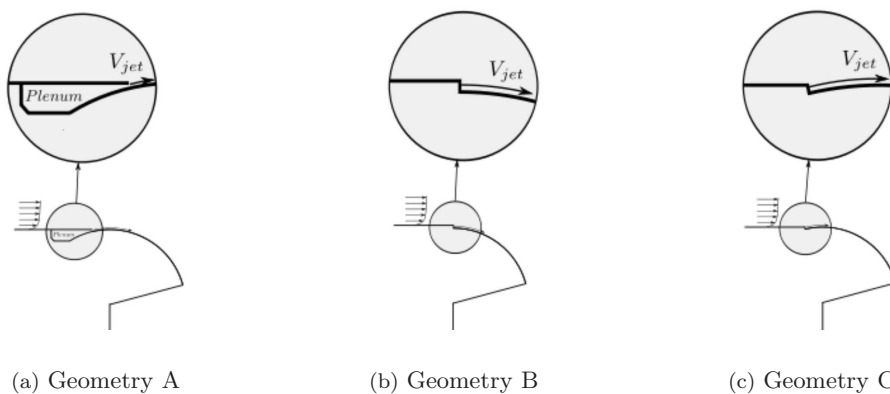


Figure 4.13: Different velocity inlet geometries

The velocity profile exiting the plenum will influence the mixing with the shear layer and the separation behavior in the adverse pressure gradient on the curved surface. In [17] the authors claim to have investigated several plenum inlet conditions and its effect on the Coanda effect and stipulate the difficulty in finding experimental values for the velocity profile due to the small size

of the velocity inlet (typically  $< 1 \text{ mm}$ ). Their CFD values for the velocity profile show a channel flow like turbulent velocity profile.

For this research the fullest possible velocity profile is used for the inlet, as the distance the jet traveled before reaching the adverse pressure gradient is larger compared to other research [38, 40]. The velocity profile has developed to a channel flow like velocity profile at  $\theta < 0$ . The traveled distance is large due to the relatively large ratio of  $\frac{h}{R_1}$  and therefore  $\theta'$ , see figure 4.11.

#### 4.4.2 Boundary layer grid

The hexahedral boundary layer grid consists of more grid sectors compared to the GETS model due to the increased complexity. Also more refinements are required as the jet boundary layer, the GETS boundary layer and the shear layer mixing need to be captured in detail by the grid. For the boundary layer modeling the near wall approach will be used (as discussed in section 3.3) leading to a very small first cell height of approximately  $0.05 \text{ mm}$ , using equation 3.11 and 3.10.

Where the structured grid is connected to the unstructured grid a more even node spacing is required to ensure a successful coupling in IcemCFD. To achieve this an extra expansion grid sector has been added to the structured grid, in the area where the jet expands to form a wake.

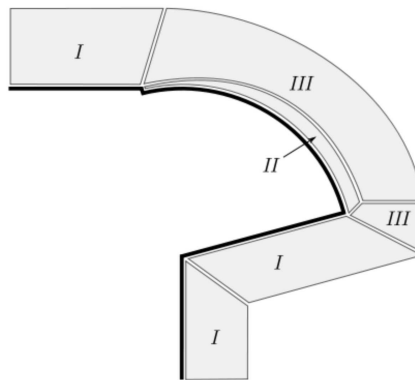
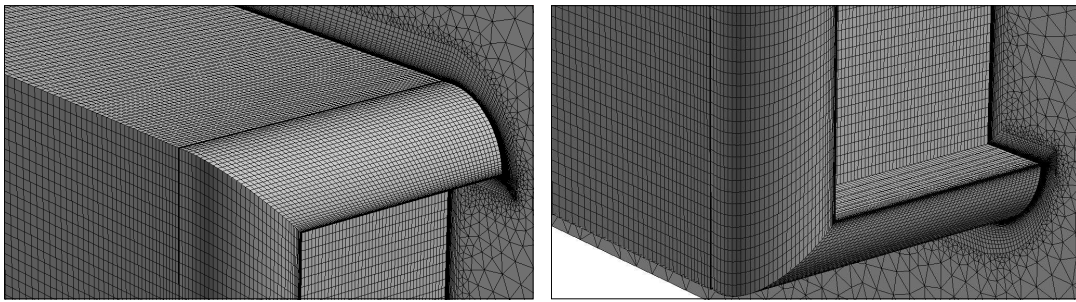


Figure 4.14: AFC grid sectors in symmetry plane (schematic)

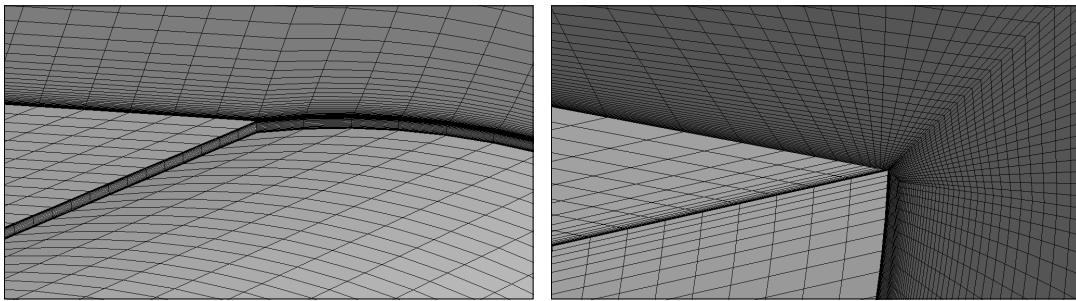
In figure 4.14 the grid sectors for the boundary layer on the GETS model is shown in (I), the velocity inlet and the exiting jet are part of a separate grid sector (II). In the jet sector the boundary layer separating from the GETS model and the boundary layer on the Coanda surface are both captured, requiring a dense grid in this region. Above and aft the jet region an expansion region (III) is created to ensure a successful coupling of the structured to the unstructured grid in IcemCFD. During the grid generation process often errors occur during this coupling, or apparent successful couplings led to low quality cells. This approach is preferred over creating an O-grid on the base of the model using the jet-velocity sector (II). Although this would lead to higher quality cells, due to the small cell sizing in the amount of additional cells required is unpractical taking the computation time into account.

The expansion regions are modified per grid as the different values for the velocity inlet height  $h$  require different expansion ratios to ensure grid quality. In IcemCFD the grid sectors are modelled as separate blocks and mapped onto the surfaces after which the surface mesh is extruded in perpendicular direction to create the hexahedral grid. The choice of expansion regions lead to some skewness in the grid, however connecting the structured mesh to the unstructured mesh proved to be very sensitive to node spacing and growth ratio on the connecting surface. (mainly



(a) Surface mesh of the top Coanda surface

(b) Surface mesh of the bottom and side Coanda surface



(c) Velocity inlet sector detail

(d) Close up of jet expansion mesh

**Figure 4.15:** Surface and boundary layer mesh of AFC-half model

due to the very small element heights in the boundary layer) The element skewness in the grid rarely exceeds the allowed value and no convergence errors occurred in the flow solver.

In figure 4.15 the surface mesh on the Coanda surfaces is shown as well as some close-ups of the jet grid sector and the expansion region. Note that the displayed grid has a Coanda surface angle of  $\theta = 90deg$ .

### 4.4.3 Unstructured grid

Similar to the GETS grid the structured grid of the AFC model is enclosed by a wake domain, with smaller cell spacing to capture the wake. The wake domain extends  $3.5w$  aft of the base of the model; the wake is expected to be shorter for the aerodynamic tool, but as also simulations are performed without blowing the maximum wake size will be similar to the wake of the clean GETS model.

The minimum cell spacing in the wake is chosen such that the unstructured mesh is able to connect to the unstructured mesh, this results in the quality of pyramid elements (the connecting elements) being related to the tetrahedral element size in the wake domain.

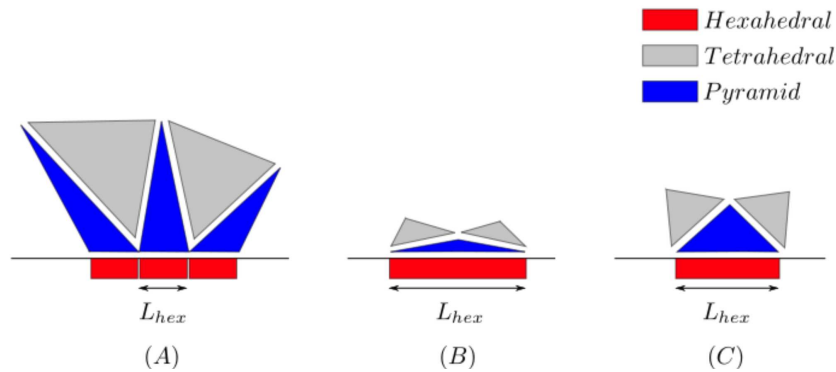


**Figure 4.16:** Grid connection 2D (schematic)

In figure 4.16 this is clarified; in situation (A) the tetrahedral size is too large compared to the hexahedral element (indicated by  $L_{hex}$ ), leading to highly skewed pyramid elements. In situation (B) the reverse is the case, again leading to highly skewed pyramids. In (C) the ratio between both element sizes is adequate, leading to high quality tetrahedral and pyramid elements. In the 3D situation the same principle holds, but now also requiring the aspect ratio of the hexahedral face to be close to 1 for high quality pyramid elements. Connecting the structured to the unstructured grid is more critical for the AFC grid as the smallest boundary layer element is approximately 50 times smaller compared to the GETS boundary layer elements due to the use of the near wall approach instead of wall functions.

For the AFC grid it is unrealistic to also apply a floor boundary layer grid; the use of the near wall treatment would require additional cells if this method would also be applied for the floor surface. Unfortunately it is not possible in Fluent to choose a different wall modeling approach per boundary surface, as the wall function approach would be sufficient for the moving floor. The difference in floor boundary conditions is discussed in section 5.4.

As for the GETS grid the outer domain is filled with tetrahedral elements, with a maximum size of  $2m$  and a growth rate of 20%. An overview of the complete grid and some details is shown in figure 4.17 and the distribution of elements and distribution in sectors is tabulated in 4.2. From the table it can be seen that the near wall approach leads to nearly 45% of the elements located only in the boundary layer for the AFC grid opposed to 23.4% for the GETS grid.

The percentage of element types and sector distribution does not vary with different total grid elements, due to the parametric script file. All the node spacings and amounts of elements are related to each other, making it relatively easy to simulate different grid sizes.

Type	Percentage	Grid Block	Percentage
Hexahedral	44.9 %	Boundary Layer	44.9 %
Tetrahedral	54.1 %	Wake Grid	41.1 %
Prism	0 %	Floor	0 %
Pyramid	1 %	Domain	14 %

**Table 4.2:** Element and type distribution in GETS model

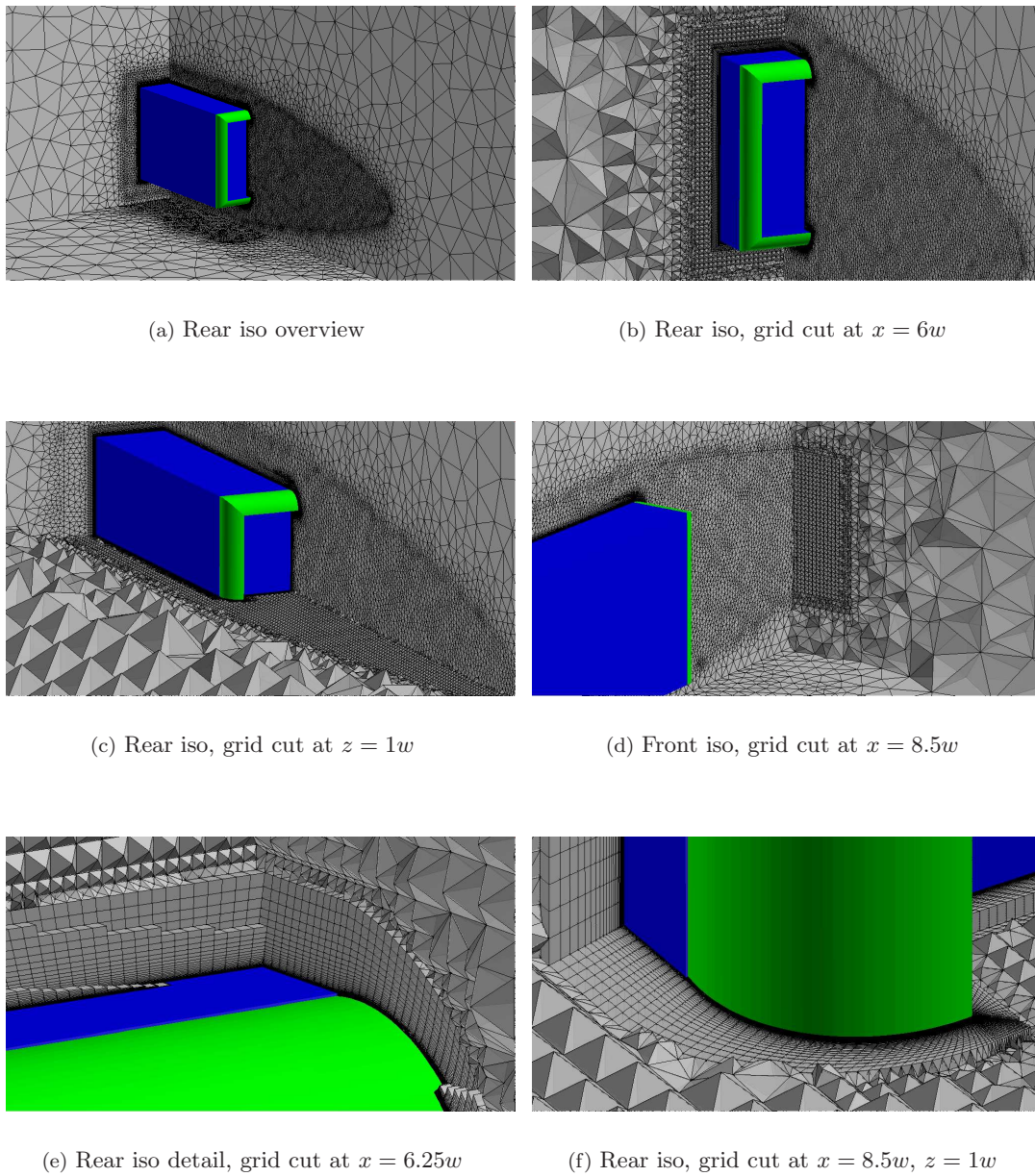


**Figure 4.17:** Domain grid AFC-half model

## Simulation Results GETS Model

In this chapter the simulation results of the clean GETS model are discussed in order to achieve some insight in its flow structure. Furthermore the implications of several modeling simplifications made during the pre-processing of the GETS model are discussed. At first the wall modeling approach is verified for applicability and convergence is demonstrated for the used computational grids.

### 5.1 Wall function validity

As the GETS model is simulated with use of the wall functions approach the  $y^+$  values as described in section 3.3 are required to be within a certain range for the boundary layer modeling approach to be applicable. According to [3] the  $y^+$  values need to be within the  $30 < y^+ < 300$  range for use of the non-equilibrium wall functions.

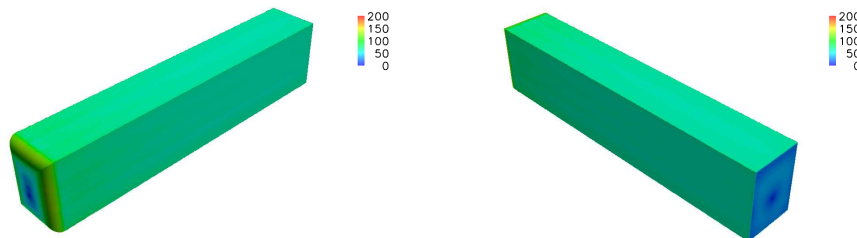


Figure 5.1:  $y^+$  values on GETS model

In figure 5.1 a contour plot of the  $y^+$  values on the surface of the GETS model is shown, the maximum value is below 200 and a value of zero is found only in the stagnation region, however this is inevitable according to the definition of the  $y^+$  parameter, see equation 3.11. The use of the wall functions is therefore possible with the applied boundary layer grid sizing.

### 5.2 Grid independence

The choice of grid size is a compromise between computational power and the required accuracy. More cells lead to more computing time and longer convergence time due to increased amount

of equations and required iterations. In general for denser grids the solution scheme requires lower under-relaxation factors to ensure a stable solution, this leads to more iterations to achieve a converged solution. As this research is aimed at reducing the drag coefficient, the solution is assumed to be converged when the drag coefficient is constant with an accuracy of a single drag count for 200 iterations. For increasing grid density, the evolution of the drag and lift coefficient with the amount of iterations can be seen in figure 5.2.

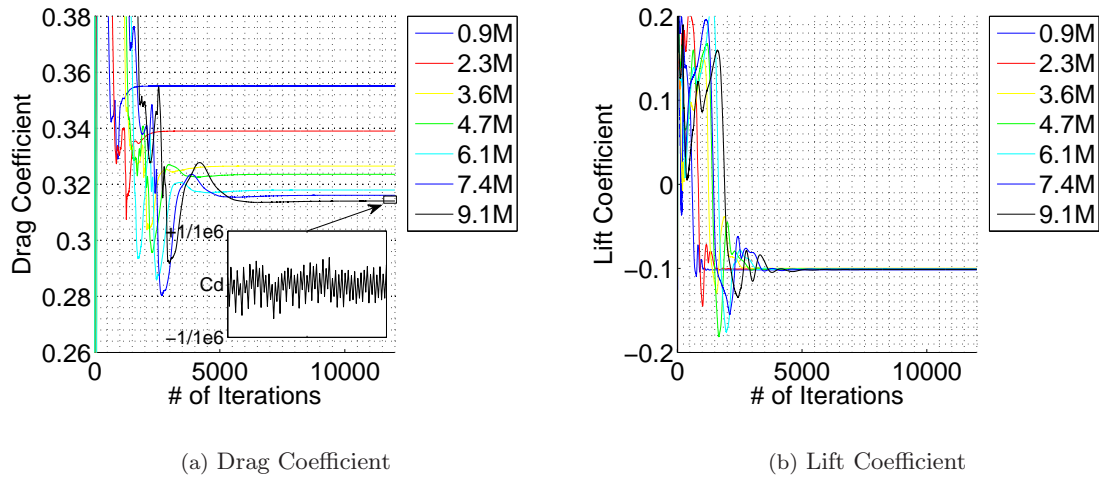


Figure 5.2: Convergence of drag and lift coefficient

The figure shows the increased amount of required iterations for the coefficients to converge, the grid consisting of approximately 1M cells converges with 4000 iterations while the 9.1M grid requires nearly 10000 iterations. The lift coefficient converges faster compared to the drag coefficient and requires only 5000 iterations to converge. The oscillations in the drag coefficient for the 9.1M cells is shown in the detail area and shows the effect of the unsteadiness in the solution. The variations are small compared to the converged value indicating that the time-dependent effects are small for the GETS model.

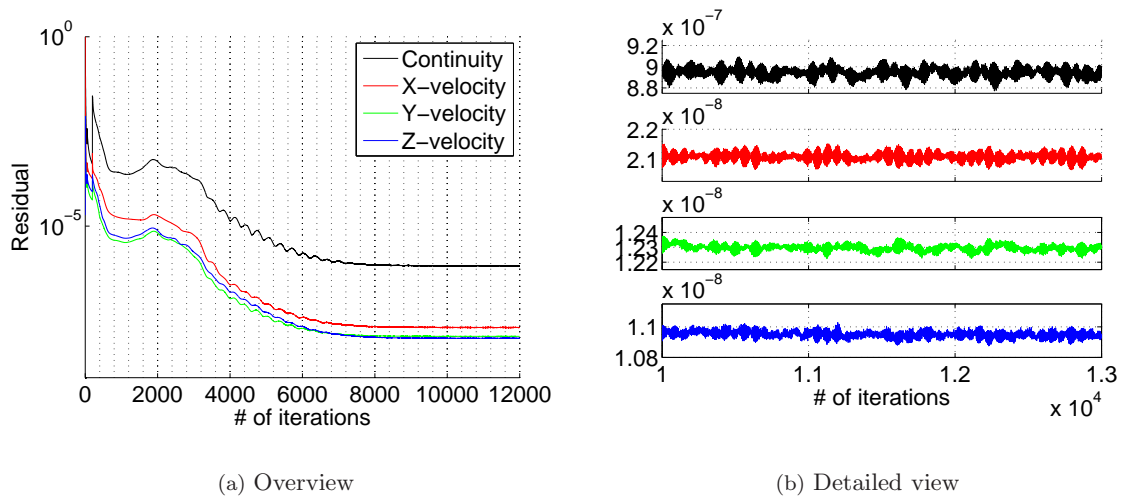
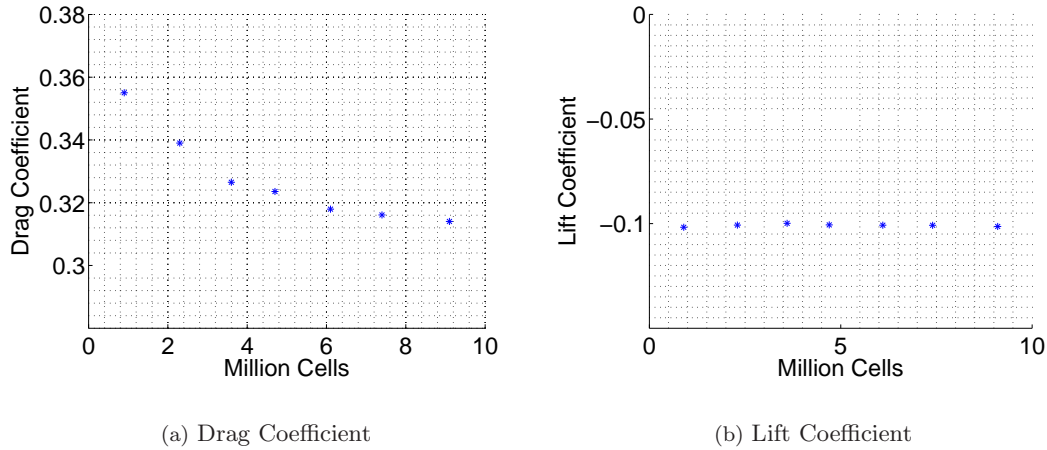


Figure 5.3: Residuals GETS simulation, 6.1M cells

The residuals for a 6.1M cells grid are shown in figure 5.3 in a detailed and zoomed view, furthermore showing the small amplitude in the oscillation, indicating that the effect of time-averaging has a small effect on the flow field of the GETS model. As can be seen in the residuals the 6.1M cells grid is converged for approximately 8000 iterations.



**Figure 5.4:** Drag and Lift convergence for different grid sizes

In figure 5.4 the final value of the drag and lift coefficient can be seen for different grid sizes. The drag coefficient converges to a final value of 0.3140 for the full scale model, whereas the lift coefficient converges to  $-0.1014$ . It can be seen in figure 5.4 that the drag value only changes from 0.3180 for a 6.1M cells grid to the value of 0.3140 (a 1.25% difference) for a 50% increase of grid cells. Using Richardson extrapolation the asymptote is found to be at a drag coefficient of 0.3063 (see appendix C and table C.1). The amount of cells required to obtain this value with the used grid topology is approximately 20M, which is unpractical in an engineering point of view.

In figure 5.5 the velocity profiles in the symmetry plane for various distances ( $0.5w$ ,  $1.5w$  and  $2.5w$ ) behind the GETS base (see figure D.1) are shown for different grid sizes. In this figure the difference between the velocity profiles for a 2.3M coarse grid and the finer 6.1M and 9.1M grid cells is shown to be nearly identical for the two finer grids.

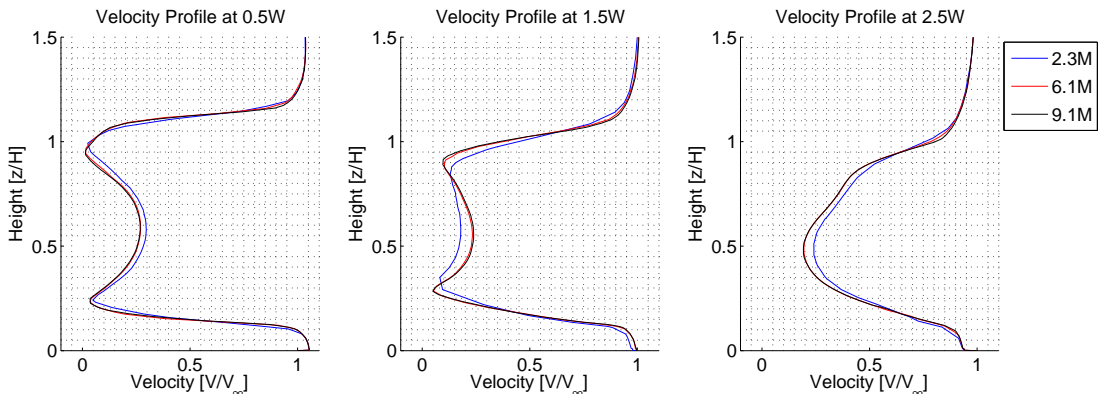


**Figure 5.5:** Velocity profiles at three stations behind the GETS model

Because the drag value only changes with 1.25% for the grid with 50% more cells and the velocity

profiles are very similar the solution is assumed to be grid-converged for the grid density used for the  $6.1M$  cells grid. The 1.25% improvement is not considered to be worthwhile the additional computational costs as the accuracy which can be expected from a CFD study for a drag coefficient of a bluff body [29, 39, 50] is not within the 1.25%. It is interesting to note that the lift coefficient seems to be similar for all grid sizes, although this not necessarily means the flow field is similar for the different grids.

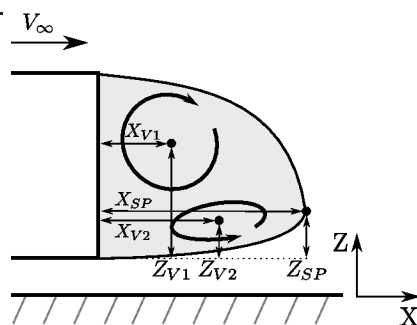
### 5.3 Grid dimensions

To save computation time the grid is split in half and a half model of the GETS is used in the simulations. In order to reduce the computation time more a two dimensional grid could be used to investigate the flow around the model. In [32] it is stated that there is a large difference between two and three dimensional bluff bodies, which is compared in this section. In this section a two dimensional simulation is compared to a three dimensional half and full model. The two dimensional grid is created by using the symmetry plane of the three dimensional grid and thus consists of the same grid topology.

The drag coefficient for the full model is 0.3177 compared to 0.3180 for the half GETS model, difference of less than 1%, which as stated before is smaller compared to the expected accuracy of a CFD prediction of the drag of a bluff body.

As the drag coefficient is similar for the half and full model, the flow structure could be different between both simulations. A primary vortex will develop in the wake of the model, and the locations of the vortex core intersections with the symmetry plane and the saddle point closing the wake is tabulated in 5.3 for comparison between the simulations. For reference the results from the simulations of the GTS model from [56] are also shown in the table.

	2D	3D half	3D full	GTS [56]
$X_{SP} (X/W)$	2.9	2.2	2.0	1.75
$Z_{SP} (Z/H)$	0.44	0.41	0.42	0.25
$X_{V1} (X/W)$	1.0	0.45	0.49	0.58
$Z_{V1} (Z/H)$	0.86	0.93	0.92	0.85
$X_{V2} (X/W)$	1.7	0.99	0.97	0.82
$Z_{V2} (Z/H)$	0.29	0.22	0.22	0.10
$C_D$	0.0245*	0.3180	0.3177	0.254
$C_L$	-0.0608*	-0.1007	-0.1010	-



\*coefficient based on H

**Table 5.1:** Locations of saddle point and vortex cores

The saddle point (SP) in the 2D simulation is further downstream compared to the 3D simulations, which has also been noted in [32] and in [44]. In the latter the effects of separated shear layers in high Reynolds regime is claimed to be highly three dimensional even for two dimensional cases.

In the two dimensional simulation the flow also separates from the front top radius of the GETS model, leaving a large separated area above the GETS model. Although the radius fulfills the critical Reynolds number criteria as used in [10] and later in [22] this separation influences the flow downstream.

Furthermore the difference between the GETS results and the GTS simulations are visible. The characteristic points are all located lower for the GTS model and the wake length is shorter compared to the GETS model.

In figure 5.6 the base pressure coefficient is shown for both the half model and the full model. The irregularities on the center line can be explained due to the mirroring in the used software. The only difference between both is the pressure center on the base is slightly higher in the full model simulation.

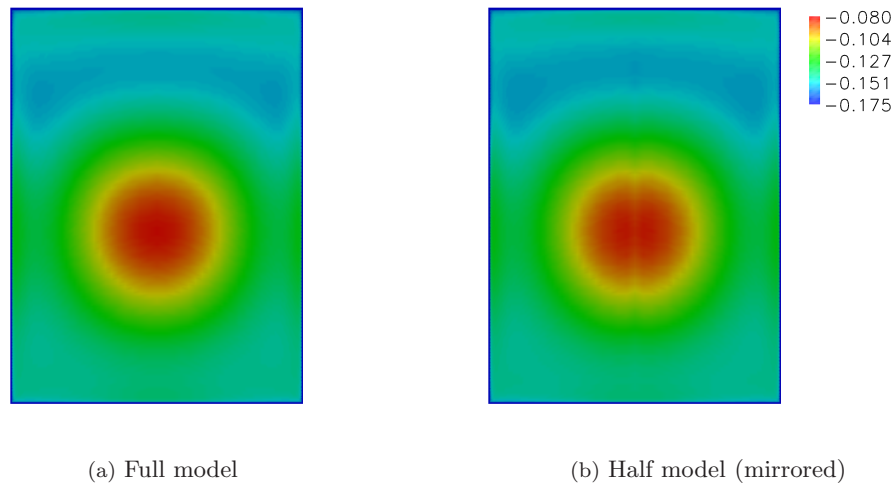


Figure 5.6: Base pressure coefficient

Concluding from the above results a half model is sufficient to model the GETS model for symmetric cases using the RANS equations. This leads to a reduction of cells by 50% and thus significantly reduces computing time. A two dimensional model is not applicable to model a three dimensional bluff body as the three dimensional effects dominate the final results.

## 5.4 Floor boundary condition

The influence of the road on the flow field can be significant for vehicles in close ground proximity [7], this can be different for a truck as the ground clearance is much higher compared to passenger or race cars. In the application of CFD the ground boundary condition can be treated in three ways:

- Moving wall
- Symmetry plane
- Fixed wall

The moving wall is a no slip condition where the slip velocity is equal to the freestream velocity. In this situation no boundary layer develops on the floor, except where the adjacent velocity is different from the freestream velocity due to the presence of the model. This approach requires the use of a grid where a boundary layer can be modelled on the wall, thus requiring a prism layer or a structured and refined grid. This increases the number of cells required and is thus less computationally effective.

A symmetry plane can be used to enforce the normal velocities on the floor to be zero. The tangential velocity can be non-zero, thus a boundary layer will not develop on the floor. This eliminates the requirement for a boundary layer grid on the floor, thus reducing the required amount of cells.

For simulations of a wind tunnel environment a fixed wall is often used as most wind tunnels do not possess a rolling floor. This fixed wall will allow for a boundary layer to develop on this floor which will not develop when a rolling floor is used and this needs to be taken into account.

The total drag coefficient as well as the location of the vortex cores and the saddle points for equal grids with different floor boundary conditions is summarized in table 5.2. The total drag coefficient is slightly effected by the floor boundary condition, showing a less than one percent variation. The velocity profiles in the wake symmetry plane are shown in figure 5.7 and a close up of the profiles in ground proximity is shown in figure 5.8.

	$C_D$	$C_L$	$\Delta C_D$	$\Delta C_L$	$X_{SP}$	$Z_{SP}$	$X_{V1}$	$Z_{V1}$	$X_{V2}$	$Z_{V2}$
Moving floor	0.318	-0.101	–	–	2.0	0.41	0.45	0.93	0.99	0.22
Stationary floor	0.320	-0.093	0.62%	-7.9%	2.0	0.44	0.45	0.93	0.92	0.22
Symmetric floor	0.320	-0.099	0.62%	-2.0%	2.0	0.42	0.45	0.93	0.99	0.22

**Table 5.2:** Flow properties for different floor BC's

The upper vortex core ( $V1$ ) remains in the same position for all boundary conditions, while the  $x$ -coordinate of the second vortex core ( $V2$ ) moves closer to the base. The  $z$ -coordinate of the saddle point ( $SP$ ) moves upward when the floor is modelled as a fixed wall. This indicates a change in the behavior of the vortex core when the floor is treated as a fixed wall and a boundary layer develops which interacts with the wake.

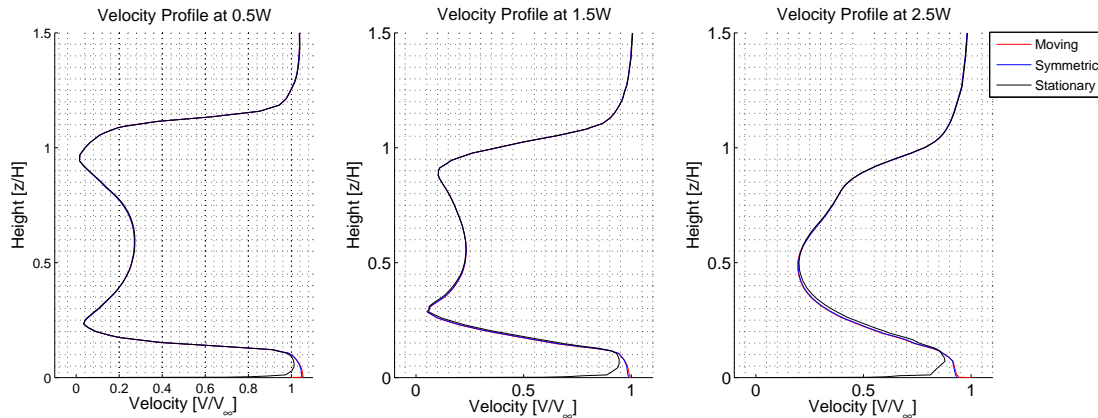


**Figure 5.7:** Velocity profiles behind the GETS model ( $Z = 0$  indicating ground plane)

It can be seen in figures 5.7, 5.8 how the velocity profile changes near the floor with different boundary conditions. In case of a symmetric floor no boundary layer is formed, while the boundary layers for the moving and stationary floors differ significantly. The velocity in the wake area is below freestream velocity therefore the flow is accelerated by the floor in the moving wall situation opposed to decelerated in the stationary wall simulation.

The velocity profile of the moving wall and the symmetric wall are similar in shape, the difference is only seen for  $z/H < 0.15$ . The reduction in cells is significant, specially when the near-wall approach is used, as this boundary layer modeling requires  $y^+$  values below 5. As the AFC system

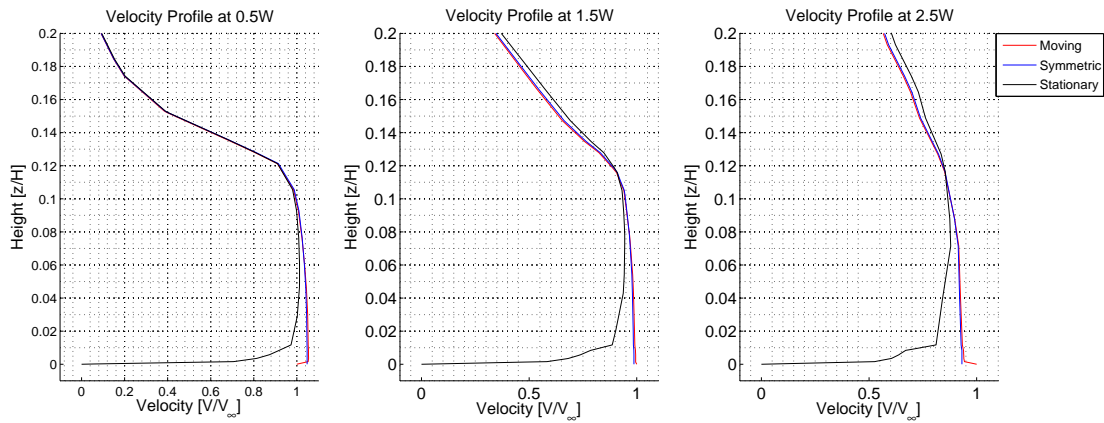


**Figure 5.8:** Close up of velocity profiles behind the GETS model ( $Z = 0$  indicating ground plane)

is modelled with the near-wall approach the reduction in cells by using the symmetric wall boundary condition is preferred as this does not require the meshing of a prism layer.

Although the wake velocity profiles show good agreement between the moving and symmetric wall conditions, the drag coefficient of the symmetric wall is closer to the fix wall simulation. This is remarkable as the velocity profiles of the fixed and the symmetric wall differ more than expected from the difference in  $C_D$  value. To compare the difference in pressure distribution of the moving and symmetric wall condition the difference in pressure coefficient is shown in figure 5.9.

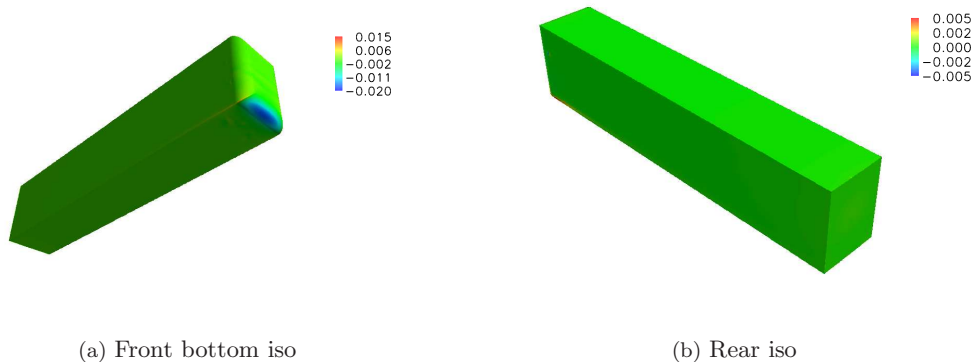


**Figure 5.9:** Pressure difference ( $C_{p,moving} - C_{p,symmetric}$ )

In this figure it is clear that in the moving wall simulation the suction peak on the lower curved face is higher compared to the symmetrical case. A higher suction peak leads to forward thrust (and thus reduced drag) and less lift. Furthermore the base pressures vary little between both different floor boundary conditions, which is the region of interest for this research. The suction peak can be explained by the effect that the boundary layer which develops on the moving floor will be largest near the rounded edges on the model. A boundary layer develops on the wall under the model creating a displacement thickness which accelerates the flow passing through the floor and the model, leading to a higher suction peak.

## 5.5 Flow analysis of the GETS model

In the following section some results of the full scale GETS model simulations are discussed, the simulations are performed using the moving floor boundary condition using a half model grid consisting of  $6.1M$  grid cells. These results are used to set up the simulations for the AFC system as the velocity field obtained with the clean GETS model will be used as a boundary condition for the AFC simulations.

In [54] the drag distribution of a full scale truck is calculated to be 23% caused by the front, 47% by the middle part and 35% determined by the base of the trailer. As this is a full scale model including mirrors, wheels and a tractor-trailer gap, the drag of the middle part of the combination is a larger compared to a cleaner model like the GETS model or the US GTS model. The latter model has a base drag contribution of 69% [56] due to the more rounded front geometry compared to a full scale truck and the GETS model.

In figure 5.10 the drag coefficient build up along the GETS model is displayed as well as the final drag split between the front, center and back of the model, which are defined in figure 5.10(b). Furthermore the ratio between the pressure and friction drag of the GETS model is shown, the total drag is dominated by pressure drag, which is typical for a bluff body.

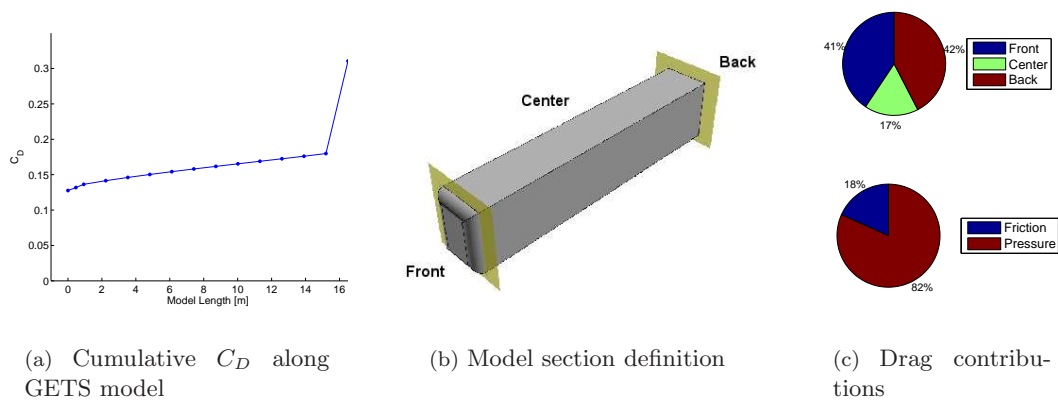


**Figure 5.10:** Drag distribution on GETS model

The front of the GETS model generates a drag as well as a thrust force due to the rounded edges where a suction peak is created. The pressure coefficient in the symmetry plane is shown in figure 5.11(a) showing the suction peak on the top and bottom of the model. A similar pressure peak occurs on the side of the model. In 5.11(b) the pressure distribution on the surface is also shown.

The stagnation region on the front of the model is clearly visible with a maximum  $C_p$  of 1.02 in the stagnation point. This is not possible for incompressible flows and this unphysical value is related to a modeling error in the  $k - \epsilon$  turbulence model which has also been noted in [50]. The over prediction of the stagnation pressure leads to an overestimated drag value and is a drawback of the  $k - \epsilon$  turbulence model. The base pressure distribution is shown in figure 5.6 and the average base pressure coefficient is  $-0.133$ . A more detailed pressure distribution at various stations on the base can be found in appendix D. In these figures the influence of the vortex core on the base pressure is visible.

The radii of the front surface are chosen in the definition of the GETS model that the flow remains attached to the model in order to keep the boundary layer aft of the model close to the flat plate estimation. In case of frontal radius separation the downstream boundary layer grows thicker which influences the separated shear layer and thus the wake properties. In [23] and more recent

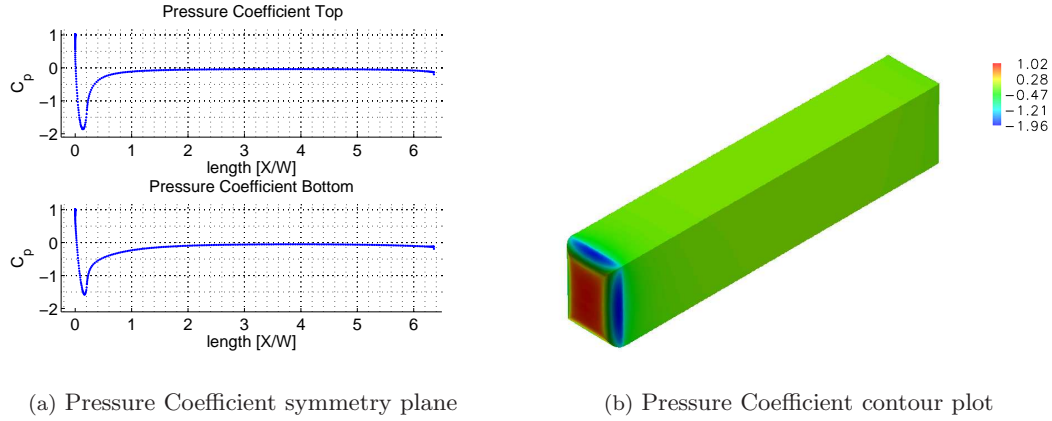


Figure 5.11: Pressure distributions GETS

experiments [55] it follows that thinner boundary layers reduces drag but cause a more negative base pressure.

In table 5.3 the boundary layer profiles on the centerline of the top, the middle and the bottom side of the model are shown, just before the forced separation point, at the start of the base. The boundary layer thickness was determined from the turbulent flat plate equations (4.1 and 4.2 from section 4.3.1) and using the power law estimation from [57]. The velocity profiles are shown in table 5.3 and the simulated boundary layer properties are obtained from the following equations:

$$\delta^* = \int_0^\infty \left(1 - \frac{u}{U_e}\right) dy, \quad (5.1)$$

$$\theta = \int_0^\infty \frac{u}{U_e} \left(1 - \frac{u}{U_e}\right) dy, \quad (5.2)$$

$$\delta = 0.99 \frac{u}{U_e}, \quad H = \frac{\delta^*}{\theta}. \quad (5.3)$$

	$\delta/W$ ( $1e-3$ )	$C_f$ ( $1e-3$ )	$\delta^*/W$ ( $1e-3$ )	$\theta/W$ ( $1e-3$ )	$H$
Top	98	2.56	6.7	6.0	1.13
Side	94	1.62	6.6	5.9	1.13
Bottom	76	2.32	5.1	4.6	1.11
Flat plate	76	1.87	9.45	7.40	1.278

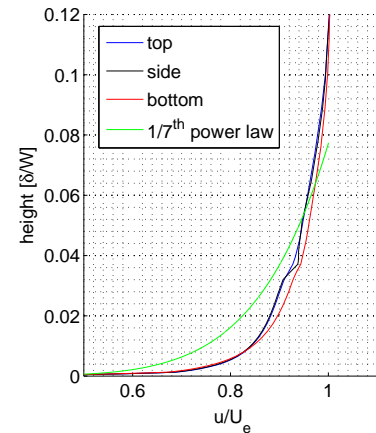
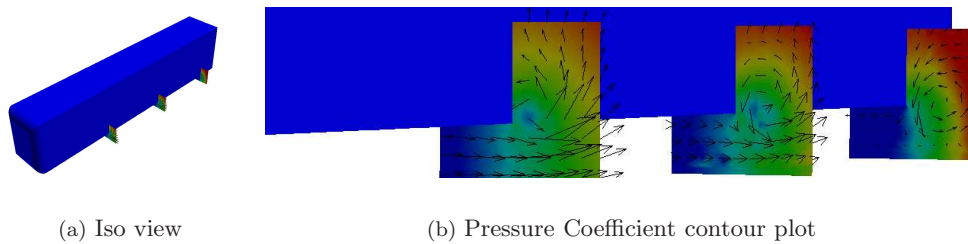


Table 5.3: Boundary Layer properties at  $x = L$  ( $y = 0$ ,  $z = 0.5H$ )

From table 5.3 it can be noted that the boundary layers are thicker and fuller in the simulations compared to the turbulent flat plate estimation. The boundary layers on the top and the side are similar, whereas the boundary layer on the bottom of the model is thinner and more turbulent. Compared to the  $1/7^{th}$  power law the velocity profile is more full and the shape factor of all the simulated boundary layers is lower indicating a more stable boundary layer. This can be explained by the relatively high turbulence intensity in the freestream flow, which increases mixing in the boundary layer and thus leads to a fuller boundary layer. Furthermore due to the high Reynolds number the effect on numerical diffusion leads to the simulation of thicker boundary layers, see section 3.5.

The skin friction coefficient at the trailing edge is determined by taking the average over the trailing line vertices, which together form the base surface. The skin friction coefficient is not constant over the width and height of the model, but has a higher value at the edges of the model.

This is related to flow in the  $y$  and  $z$  direction on the edges, on the bottom edge of the model caused by a trailing vortex which starts at the rounded edge on the frontal plane. This vortex is shown in figure 5.12 together with a contour plot of the pressure coefficient indicating the location of the vortex core.. The cut planes are at  $x = 1.8W$ ,  $x = 3.9W$  and  $x = 5.8W$  and show the airflow coming from underneath the model



**Figure 5.12:** Contour slices indicating trailing vortex

On the top side edge of the model the vortex is not present, however the cross flow close to the edge remains. This leads to the hypothesis that the presence of the trailing vortex is related to the presence of the (moving) floor. A similar flow pattern has been observed in [49] and in more detail in [48], however these results were obtained for a model with rounded side edges opposed to sharp edges for the GETS model.

The boundary layers separate from the back of the model and a shear layer is formed which encloses the wake. The current simulations only capture the average properties and some of these can be found in figure 5.13. A single vortex core is formed inside the shear layers which is visualized in figure 5.13(a) by means of the velocity magnitude and in 5.13(d) with an iso-surface of the pressure coefficient. In figure 5.13(c) a iso-surface of  $p_{total} = 0$  is shown giving an indication of wake boundaries, except for the location of the saddle point.

In figure 5.13(e) streamlines in the symmetry plane are shown indicating the locations of the vortex cores and the saddle point where the wake closes. For the exact locations of these points see table 5.3 in the column for the 3D half model. In figure 5.13(e) it is visible how the wake is curved slightly downwards towards the floor, which is a result of the presence of the floor.

The wake closing and opening (while shedding vortices) is a dynamic process and is not captured in the present steady simulations. Time-averaged vorticity plots are shown in appendix D for different iso-surfaces of constant vorticity, for clarity in figure 5.13(f) one iso-surface is shown for constant vorticity. The shear layer separating from the base contains a high level of vorticity, shown in the first sub-figures. As the wake closes the high vortical eddies diffuse and thus reduce their strength. The actual closing of the wake is not visible as the time-averaged solution shows

the entrained vortex core, but the smaller shed vortices are not individually captured, and thus the wake appears open in the time-averaged simulations, similar results were obtained by Krajinovic in [49].

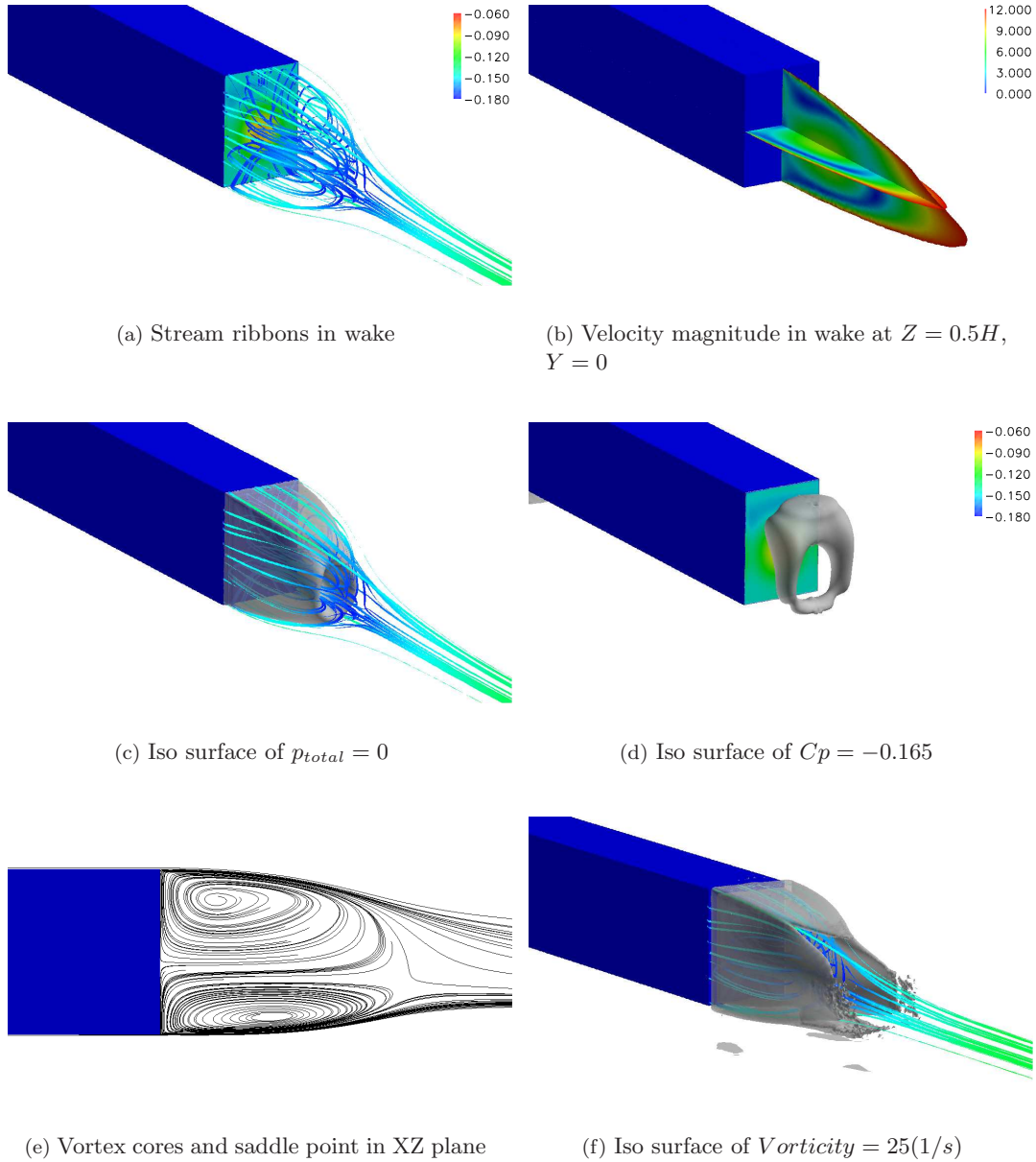


**Figure 5.13:** Wake visualization GETS model

## 5.6 Wind tunnel comparison

In this section a CFD model in wind tunnel conditions is compared the CFD results of the full scale simulations and with wind tunnel data obtained in [55]. The wind tunnel model is a 1/15<sup>th</sup> scale model of the real case model with some different boundary conditions compared to the real case model. For comparison the two model parameters are summarized in table 5.5 including the difference in boundary conditions.

	Full scale	1/15 <sup>th</sup> scale
Model scale [-]	1 : 1	1 : 15
Freestream velocity [m/s]	25	60
Reynolds number (width) [-]	$4.5 \cdot 10^6$	$0.7 \cdot 10^6$
Floor BC [-]	Moving	Symmetry / stationary
Turbulence Intensity [%]	5	1
Blockage ratio [%]	1.5	2

**Table 5.4:** Full scale and wind tunnel model data

The floor boundary conditions differ in both simulations, as the 1/15<sup>th</sup> scale model is mounted above a dummy fixed floor which extends ahead and aft of the model. The dummy floor is elevated from the wind tunnel wall in order to minimize the influence of the wind tunnel wall boundary layer on the model. Instead a new boundary layer develops on the dummy floor yielding a non moving floor condition with minimal boundary layer interference.

In the CFD simulations this is modelled as a symmetry plane ahead and aft of the dummy floor where no boundary layer is present and a fixed wall condition where the dummy floor is, allowing the growth of a boundary layer near the model, see figure 3.2 in section 3.4.1.

The wind tunnel model geometry differs from the computational model due to the presence of support struts which attach the model to the wind tunnels balance system. The struts are not modelled in the CFD simulations and are expected to lead to an increase in drag for the wind tunnel model compared to the CFD model. See [55] for more details on the wind tunnel model, setup and wind tunnel results of the GETS model measurements.

It must be noted that for this research the relative difference between the wind tunnel measurements and the CFD simulations is of interest. The data used for the comparisons is uncorrected for blockage effects and other possible wind tunnel corrections. Possible corrections will apply a multiplication factor on the measured data, relative differences will remain and the data can thus be used for comparison.

### 5.6.1 Simulation results comparison

The drag coefficient of the 1/15<sup>th</sup> scale model differs from the full scale simulations due to the difference in the floor boundary condition, the mounting struts and (possibly) the different Reynolds numbers, the drag and lift coefficients are summarized in table 5.5 for the wind tunnel measurements, 1/15<sup>th</sup> scale and the full scale simulations. The data used in the comparison for the wind tunnel measurements is for the experiments with 0.65mm zigzag tap applied to the front end of the model to prevent the occurrence of a separation bubble on the front radii curvature [55].

The data obtained from [31, 56] is corrected for blockage effects, but the models are not identical to the GETS model. The model from [31] is 1/15<sup>th</sup> m shorter, however, for the simulation at zero yaw angle the effect of this is expected to be neglectable as the change in  $W/L$  ratio is small. The GTS model from [56] is more streamlined and it is therefor remarkable that the drag coefficient equals the shortened GETS model.

	$C_D$	$C_L$
Full scale simulated	0.318	-0.100
1/15 <sup>th</sup> scale simulated	0.277	-0.136
Wind tunnel measured*	0.327	-0.08
Wind tunnel measured**	0.277	-0.093
Wind tunnel measured***	0.277	-

\*uncorrected data, 0.65mm zigzag tape  
\*\*corrected data for similar model [31]  
\*\*\*corrected data for GTS [56]

**Table 5.5:** Full scale and wind tunnel model data

The difference between the two simulated values is significant and the drag value for the 1/15<sup>th</sup> simulations is nearly 15 percent different from the full scale simulations. To further compare the results from both simulations the locations of the vortex cores and saddle point is shown in table 5.6.1.

	$C_D$	$C_L$	$\overline{C_{p,base}}$	$X_{SP}$	$Z_{SP}$	$X_{V1}$	$Z_{V1}$	$X_{V2}$	$Z_{V2}$
Full scale	0.318	-0.100	-0.133	2.0	0.41	0.45	0.93	0.99	0.22
1/15 <sup>th</sup> scale	0.277	-0.136	-0.146	2.0	0.27	0.48	0.81	0.81	0.10

**Table 5.6:** Data from wind tunnel and full scale simulations, coordinates expressed in  $X/W$  and  $Z/H$

From the table it can be seen that the locations of the three characteristic locations are all lower in the 1/15<sup>th</sup> scale simulations compared to the full scale simulation. The position downstream of the base is (except for the lower vortex core) in good agreement with both simulations. In figure 5.14 the velocity profiles at three stations in the wake (see figure D.1) are shown for both the simulations. As can be seen in the figure is the difference at the first station (close to the base) is smaller compared to the difference at the more downstream stations.

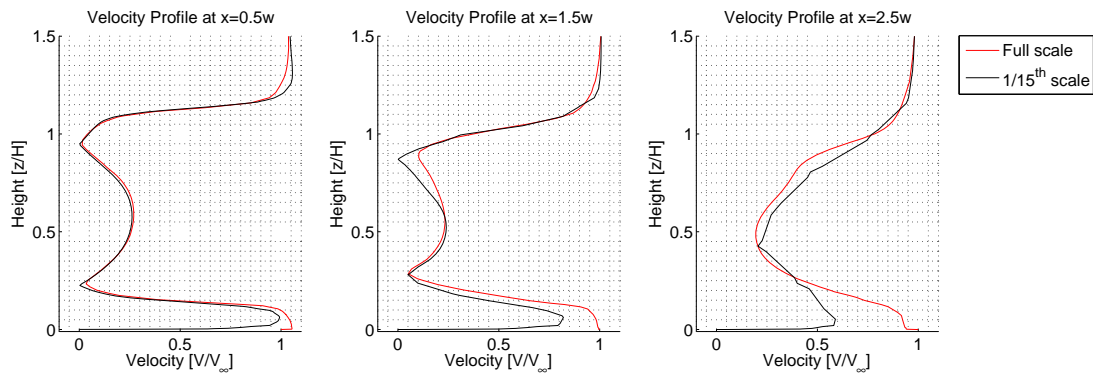


**Figure 5.14:** Velocity profiles behind the GETS model (stationary and moving BC)

The effect of the stationary floor and the moving floor is much more pronounced in the 1/15<sup>th</sup> scale model compared to the full scale stationary ground simulations. In the two latter stations the difference in velocity profile is also larger further from the ground as the different floor boundary condition in the wind tunnel simulations influence the flow above the floor.

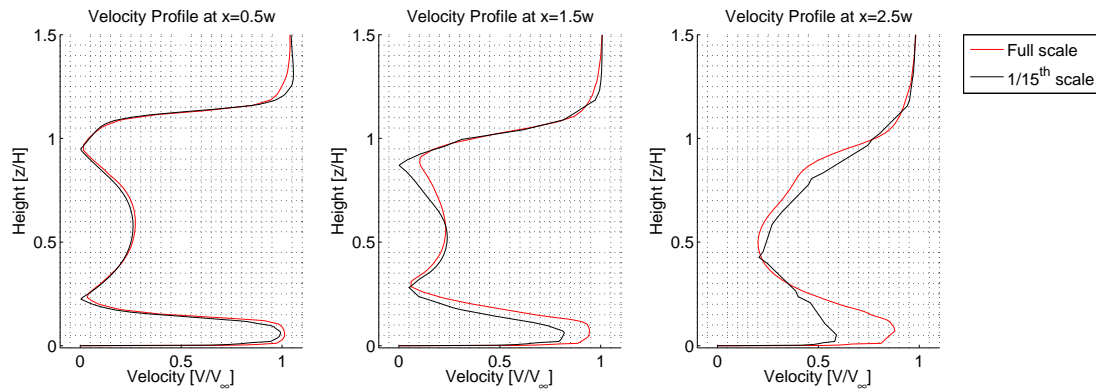


**Figure 5.15:** Velocity profiles behind the GETS model (stationary floor BC)

For comparison the full scale simulations with the fixed floor boundary condition are compared to the wind tunnel simulations in figure 5.15. In these figures the same results follow; the velocity profiles at the first station are similar between both simulations, however in the last two stations the influence of the floor on the flow is stronger present in the  $1/15^{th}$  scale model compared to the full scale simulations. The boundary layer developing on the floor underneath the  $1/15^{th}$  scale model will grow (using equation 4.1) to approximately  $30\text{ mm}$  and the boundary layer on the GETS model using 4.1 is approximately  $20\text{ mm}$ , which means that with a ground clearance of  $33\text{ mm}$  both boundary layers interact, which will influence the flow structure and the resulting drag coefficient.

It is expected that this interaction of both boundary layers will influence the lift coefficient, which is also suggested by the difference in lift coefficients in table 5.5. The comparison between the  $1/15^{th}$  scale model and full scale model is discussed in the next section.

### 5.6.2 Boundary layer comparison

The boundary layer on the side surface  $15\text{ mm}$  ahead of the base was measured in [55] and is compared to simulated values in table 5.7. Next to the table different velocity profiles in the boundary layer are plotted indicating the shape of the simulated, measured and theoretical boundary layers.

The wind tunnel measured values are in close agreement with the theoretical turbulent flat plate values obtained from equations 5.1 to 5.3 and the flat plate approximations from [57]. The simulated boundary layer on the model is thicker compared to the flat plate estimation and the wind tunnel measured value. As well as the displacement thickness and momentum thickness are higher compared to the measured and estimated values.

The shape factor is higher in case of the simulated values, however, it must be noted that as can be seen in the figure (5.7) there is an irregularity in the simulated results for the wind tunnel boundary layer. This irregularity is due to the interface of the hybrid mesh and the interpolation during the data export. This irregularity influences the results and the integration of equations 5.1 to 5.3 which can explain a small difference in the  $\delta^*$ ,  $\theta$  and  $H$  values.

Compared to the flat plate estimation the CFD results overestimate the thickness of the boundary layer, however, the  $\delta^*$ ,  $\theta$  and  $H$  values agree fairly well. In the figure the flat plate estimation for a longer plate (thus thicker boundary layer) is also shown (the corrected  $1/7^{th}$  power law), which has a similar boundary layer profile compared to the simulated wind tunnel results.

Compared to the  $1/15^{th}$  scale simulation the full scale simulation has much fuller profile, also indicated by the lower shape factor. The difference can be explained by the low freestream turbulence

	$\delta/W$ ( $1e-3$ )	$C_f$ ( $1e-3$ )	$\delta^*/W$ ( $1e-3$ )	$\theta/W$ ( $1e-3$ )	$H$
CFD full scale	94	1.62	6.6	5.9	1.13
CFD 1/15 <sup>th</sup> scale	147	2.51	15.6	11.6	1.34
Wind tunnel (0.65mm)	105	—	14	10.4	1.3
Flat plate	110	2.70	13.6	10.7	1.278

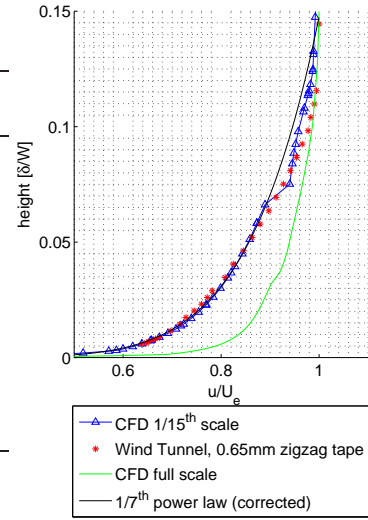


Table 5.7: Boundary Layer properties at the top surface ( $x = 6.27W$ ,  $y = 0$ )

intensity of the wind tunnel compared to the full scale simulations. The higher turbulence intensity in the full scale model simulation leads to more mixing in the boundary layer and thus a fuller profile. Furthermore numerical diffusion (see section 3.5) leads to thicker boundary layers at high Reynolds numbers.

To further analyse the differences in boundary layers on the different scaled models the boundary layer development underneath the model in the symmetry plane is shown in figure 5.16. In this figure the height is scaled with the ride height and the velocity is scaled to the freestream velocity. The freestream velocity is used it is not possible to determine the velocity outside the boundary layer in the scaled simulation, as the floor and model boundary layer merge.

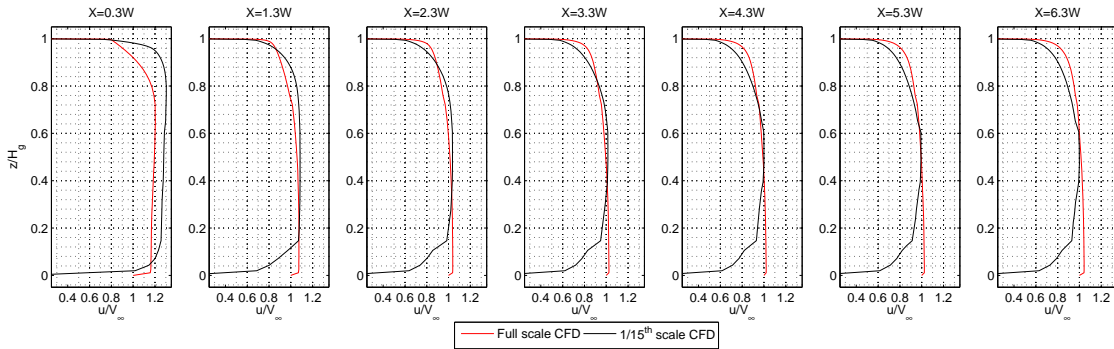


Figure 5.16: Boundary layer development underneath the model

This merging of both boundary layers can be seen as the flow under the scaled model resembles a channel flow and will lead to a blockage effect underneath the model. This blockage effect will increase the side flow under the model, increasing the trailing side vortex strength (see figure 5.12).

It must be noted that the used grid consists of a structured mesh, connected to an unstructured mesh and a prism layer on the ground plane (see section 4.3). This grid topology is not optimal for the interacting boundary layers, as this would require a complete structured grid, opposed to a hybrid grid. Furthermore the application of the wall functions (section 3.3) is not suited for modeling interacting boundary layers [3].

### 5.6.3 Yaw sensitivity

In real case situations a truck is always experiencing crosswind [54] introducing a side flow component on the model. The maximum side wind angle experienced by a typical truck is in the order of 10 degrees, and can have a large influence on the total drag and side force on the truck due to flow separation on the front end of the truck.

By definition, the drag coefficient is defined as the component in freestream flow direction. However for vehicle aerodynamics the drag in the vehicle coordinate system is more common and practical as this is the largest part of the drag that has to be overcome by the truck. Therefore the forces working on the body are split in a tangential component  $C_T$  and a side component  $C_S$  perpendicular to the tangential component. The definition remains the same in the yaw angle simulations.

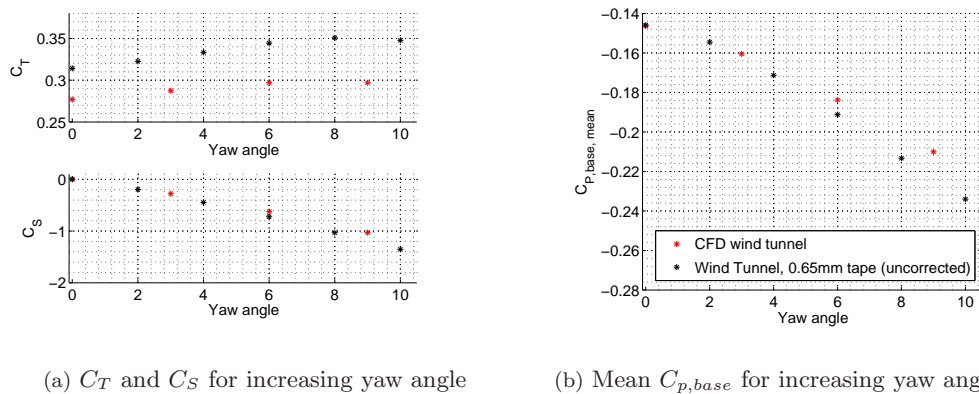


Figure 5.17: Force and pressure coefficient for increasing yaw angle

The  $C_T$  and  $C_S$  coefficients and the mean base pressure coefficient are shown in figure 5.17 for a yaw angle  $0 < \beta < 10$  degrees. The tangential coefficient remains approximately constant after 6 degrees while the side force coefficient increases. The increased suction peak on the leeward front edge curvature creates a larger forward suction as well as a side ward suction force. The CFD and wind tunnel results follow the same trend, however, the uncorrected data is offset compared to CFD for the  $C_T$  coefficient.

In figure 5.17(b) the base pressure coefficient is shown, which decreases with increasing yaw angle, increasing the suction force on the back of the model. The  $C_T$  coefficient does not increase accordingly due to the increased suction peak on the front of the model for increasing yaw angle. For the zero degree yaw case the wind tunnel simulation and measurement agree well, but the trend agreement decreases for increasing yaw angle.

Under non-zero yaw conditions a vortex originates from each corner of the front end of the model, which trail downstream and interact with the wake. The vortex is similar as shown in figure 5.12 and now also exists on the top of the model, see figure 5.18.

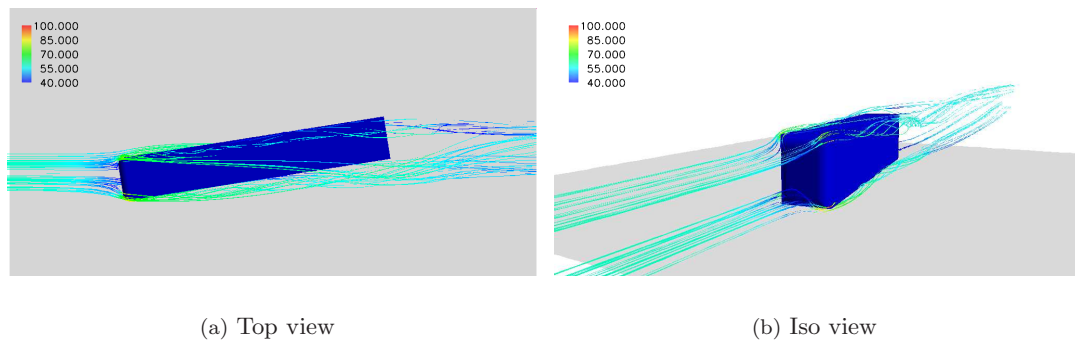


Figure 5.18: Streamlines indicating vortices for  $\beta = 9^\circ$ , streamlines colored by velocity magnitude

#### 5.6.4 Base pressure comparison

The actual base pressure distribution on the back of the model is shown in figure 5.19 for the zero degree yaw case and in 5.20 for the six degrees yaw angle case. The data from the wind tunnel is interpolated between the measurement points using a cubic interpolation method. The measurement point at the  $(0.3W, 0.2H)$  location is interpolated from the neighboring points as the pressure orifice was not functioning during the measurements, which explains the a-symmetric behaviour in the zero degree angle of attack figures.

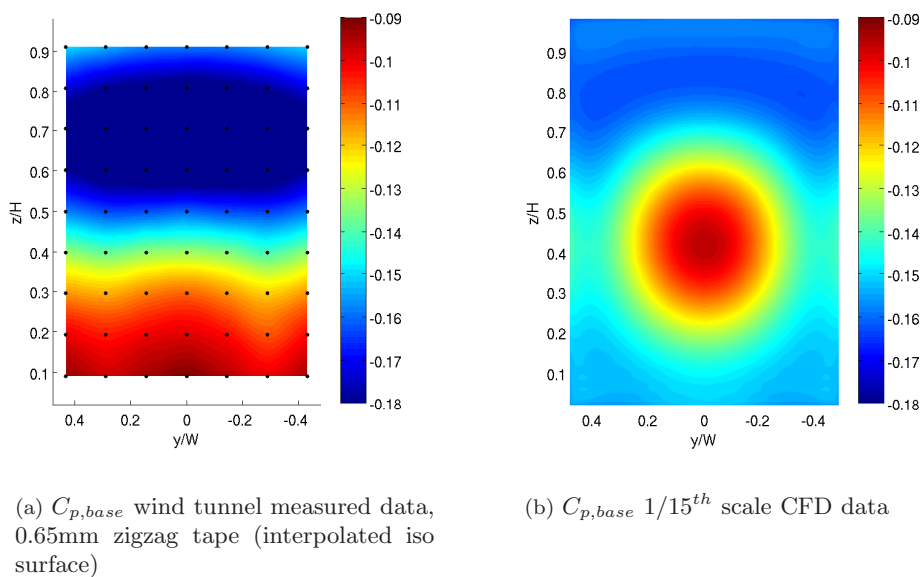
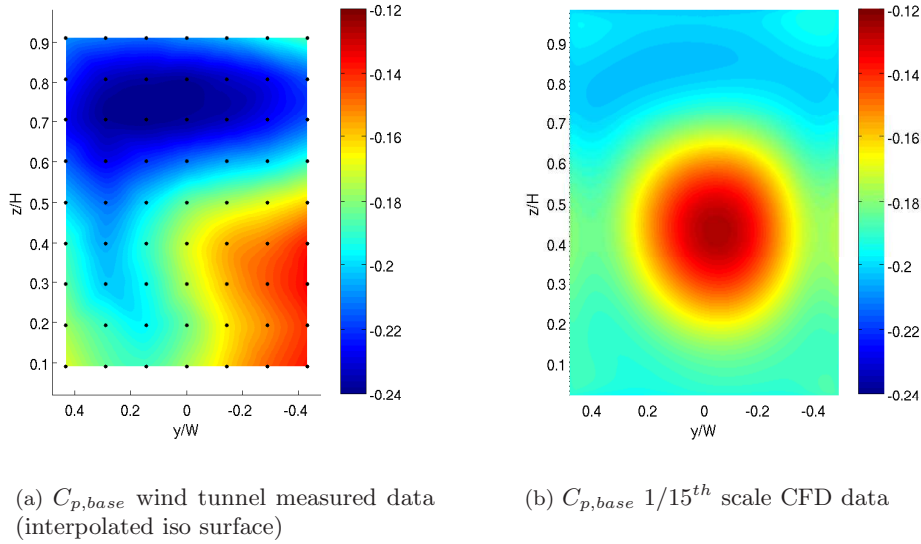


Figure 5.19: Base pressure comparison wind tunnel, measured and CFD for  $\beta = 0^\circ$

As can be seen in the contour plots the pressure distribution measured in the wind tunnel differs significantly compared to the simulated distribution obtained for the  $1/15^{th}$  scale CFD model. There is no pressure maximum close to the center of the base and the minima and maxima of the measured values are completely different compared to the CFD values. In the case of six degrees yaw the flow remains attached on the front of the GETS model, whereas it separates in the wind

tunnel data, causing a more asymmetric pressure distribution in the wind tunnel data compared to the CFD results.



**Figure 5.20:** Base pressure comparison wind tunnel, measured and CFD for  $\beta = 6^\circ$

In figure 5.21 the base pressure distribution on the base is shown compared to the CFD results at different positions on the base. The higher base pressure close to the floor for the measurements indicate that the lower vortex core is at a different position or has less influence on the base pressures as results from the CFD simulations.

Similar observations have been made in [31, 56] and also in different test facilities in [5, 50]. In [11] a significant change in the base pressure distribution was observed for ground clearances equal to the displacement thickness of the floor and the model, which leads to the conclusion that the influence of the floor and the boundary layer with respect to the ground clearance has a significant effect on the base pressures and the resulting base drag.

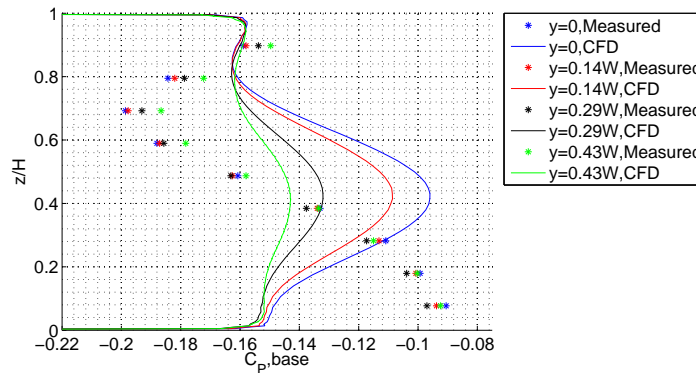


**Figure 5.21:**  $C_{P,base}$  at different positions on the base for  $\beta = 0^\circ$ , 0.65mm zigzag tape

## 5.7 Concluding remarks

In this chapter the implications of several grid and model setup options are compared and the effect on the flow field around the GETS model is analysed. The solution converges for the grid consisting of approximately 6 million cells and the use of a symmetric grid for the bluff body aerodynamics in combination with the RANS solver seems to be applicable. The difference between simulations with a moving, stationary and a symmetry plane as floor boundary conditions leads to the largest difference in flow for the stationary floor. Using a symmetry plane as a boundary condition reduces the amount of cells and yields a similar flow field to a moving floor.

The flow field generated by the GETS model is similar as found for other bluff body truck models [56, 31, 54]. The RANS simulations predict the vortex core and the trailing vortex on the lower side edge of the model. The drag split between the front, center and back of the model is less biased to the center due to the absence of wheels, mirrors and other drag causing features which are omitted for sake of simplicity.

The wind tunnel CFD simulations show a difference between the simulated  $1/15^{th}$  scale and full scale model. This is not expected as the guidelines for flow similarity for wind tunnel and full scale tests are followed. The discrepancy is expected to be found in the interaction between the (stationary) floor and the resulting interference of the boundary layer on the model and the boundary layer on the floor. Furthermore the difference in boundary layer properties between the full scale and wind tunnel simulations is significant, explaining the difference in flow fields. The turbulence intensity of the wind tunnel compared to the full scale situation and the numerical discussion are expected to be the cause of this effect.

The aerodynamic coefficients compared to corrected data from [31] agree well for the drag but a large difference is found for the lift coefficient. This can be explained by the decreased length of the GETS model used in [31]. The base pressures are compared to the uncorrected measurements from [55] and differ significantly from the simulated results. The cause for this presumably is found in the effect of the two boundary layers interacting underneath the model. The simulations use the wall function approach to model the boundary layer which are not suited for interacting boundary layers.

The interacting boundary layers do not occur in the full scale moving floor simulations, which should reduce the error in the full scale simulations. Furthermore the trend found in the average base pressure and the  $C_T$  and  $C_S$  for increasing yaw angle and the overall drag coefficient show that the RANS simulations can be used for further analysis and design of the active flow control system.



# Design of the Active Flow Control System

In this chapter the drag reduction device is implemented in the CFD computations. Different versions of the system are compared to a reference case as tested by Englar in [15]. The computational grid is verified for convergence and verification of the near wall modeling approach in appendix E, also the implications of the grid cut as described in section 4.4 are discussed in the appendix. First the determination of the drag coefficient in combination with the energy consumption of an active flow control system is explained.

## 6.1 Drag determination

The drag of the clean GETS body could be determined by summing the pressure and friction force on the individual surfaces of the model added to the total drag. For the determination of the drag coefficient of the AFC system the energy loss related to the compressor and the added momentum from the jet to the flow must be taken into account. The added momentum from the jet flow generates a thrust force which can become significant when the velocity or area ratio are chosen large (due to the large mass flow).

The thrust force from the jet can be determined from [28]:

$$F_{thrust} = \dot{m}_j V_j = \rho A_j V_j^2 \quad (6.1)$$

which is subtracted from the computed drag force. The drag reduction from the model is determined by adding the drag of the AFC system to the drag of the GETS model while subtracting the drag generated by the last  $2w$  of the clean model as determined in section 5.5,

$$C_D = C_{D,AFC} + C_{D,GETS} - C_{D,GETS(L-2w)}. \quad (6.2)$$

Using this method the assumption is made that the AFC system does not influence the drag upstream of the model further than  $2w$  upstream (where the grid is cut) and the total drag equals the drag of the GETS model including the AFC model. The resulting drag coefficient is calculated to a drag force using the dynamic pressure and the reference area.

As discussed in section 2.3.2 the Coanda jet flow requires energy which needs to be included in the evaluation of the drag coefficient. The required energy depends on the manner in which the compressor power is generated and at which efficiency. By placing the compressor intake in a stagnation point the pressure increase required from the compressor is reduced and therefore the total required power is reduced. In this research the intake pressure coefficient is taken in consideration and will be discussed further in section 6.6.

## 6.2 Englar's reference case

One of the main drivers behind this thesis project was the research done by Englar at Georgia Tech. In one of Englar's paper claims are made of drag reductions of 50% [15]. In these papers wind tunnel tests are conducted on a 0.065 scaled GTS model. The momentum coefficient was increased up till 0.15 where the drag of the GTS model kept decreasing, without correcting for the required power the maximum drag reduction achieved by Englar was 84% which indicated the possible applications of a AFC drag reduction system.

The drag was corrected by calculating the total horse power required using equation A.23 for the combined system and it is indicated that by using exhaust or turbo waste gate pressure the system could operate without requiring additional energy, thus making 50% drag reductions feasible. Blowing only the side jet slots or the top and bottom slots resulted in an increase in lift coefficient and also the drag coefficient could be increased significantly by blowing on only the sides or the top and bottom, instead of blowing on all four jet slots.

In a later paper [12] the results from a full scale test conducted after the wind tunnel experiments are summarized and an increase of fuel economy of 5 – 6% is given, which would account for a drag reduction of 12 – 15%. It is noted however that the energy consumption of the compressor is neglected in this fuel economy. Furthermore several problems appear to have arisen which made the results not as expected based on the wind tunnel experiments.

In the papers the model dimensions and momentum coefficients are given which have been used in the wind tunnel and full scale experiments. The dimensions and according  $C_\mu$  data are given in the table below. It must be noted that the wind tunnel measurements were conducted on a modified GTS model and therefore the drag coefficients can not be compared to the ones achieved with the GETS model, the same holds for the full scale test model.

	Min	Max
$R_1 [R/W]$	0.058	0.116
$R_1/R_2 [-]$	1	1
$h [h/W]$	$1.5 \cdot 10^{-3}$	$1.5 \cdot 10^{-3}$
$C_\mu [-]$	0	0.15
$\theta [deg]$	90	90
$Re_{length} [10^6]$	2.51	2.51

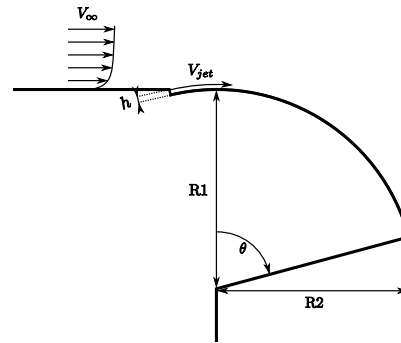


**Table 6.1:** Englar's tested geometries

Englar conducted his wind tunnel experiments at a Reynolds number, based on the model length, of  $2.51 \cdot 10^6$  which gives a width based Reynolds number (using the GTS dimensions) of approximately  $0.4 \cdot 10^6$ , according to his paper a freestream velocity was used of 31 m/s in order to achieve meaningful velocity ratios [15]. This Reynolds number is low compared to what is recommended by the SAE and as is used in this research.

Both geometries have been evaluated for multiple momentum coefficients and also for different velocity inlet heights, as it is hinted by Englar this would be the next step in his research. It must be noted that the tested blowing coefficients are lower compared to what has been referenced in Englar's research. It is found that the power required to achieve a momentum coefficient of 0.15 is far from efficient and requires more energy than is gained back by the drag reduction (see section 2.3.2).

### 6.3 Analysis of the reference case

The results of the different simulations are summarized in table E.2 in appendix E and will be discussed below. Two different drag coefficients are tabulated,  $C_{D^*}$  the drag coefficient achieved by neglecting the power consumption of the Coanda jet and  $C_D$ , the drag coefficient by assuming a compressor efficiency of 35% and a compressor inlet pressure coefficient of 0.7. The relative drag coefficient is compared to the clean model drag coefficient of 0.3180. In figure 6.1 different quantities are plotted against  $C_\mu$  and the velocity ratio  $\zeta$ .

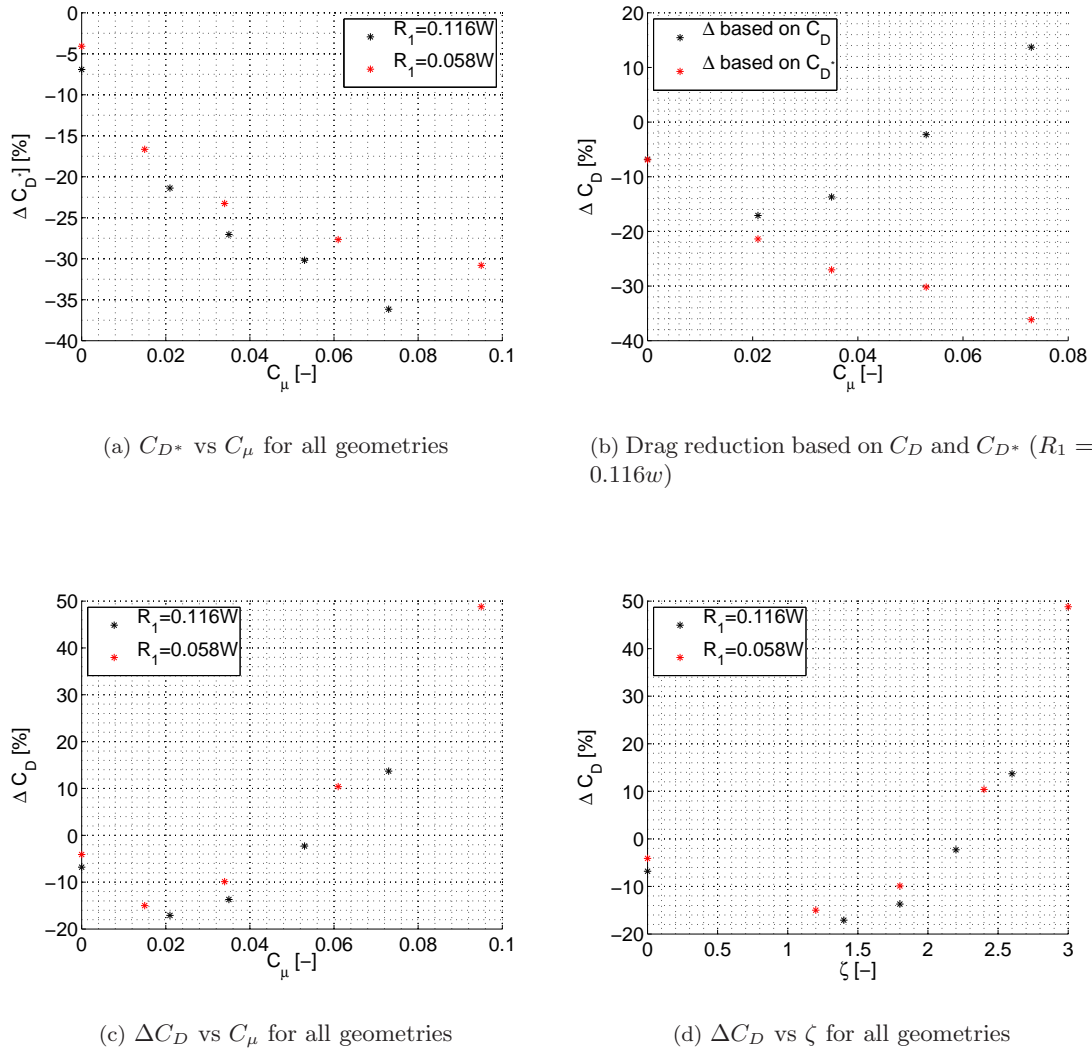


**Figure 6.1:** Reference Case Results

The first observation which is visible in all figures is the drag reduction which is present at zero blowing velocity, a reduction of nearly 4% and 7% for the 0.058w and the 0.116w radii geometries respectively. This reduction is the effect of boat tailing by means of curved base flaps, which has been researched by Ortega in [27]. The GTS model with rounded base plates led to a drag reduction of nearly 18%, however the  $R/w$  ratio was in the order of unity. The smallest radius tested in Ortega's research was 0.32w (yielding a drag reduction of 14%), which is approximately six times as large as the radius used by Englar. It will be demonstrated in section 6.5.2 that these

large radii are not optimal for use in combination with the AFC system.

In figure 6.1(a) the drag coefficient uncorrected for the energy consumption is shown for increasing momentum coefficient. It can be noted in the graph that for both radii the drag coefficient rapidly decreases for increasing  $C_\mu$ . The larger radius geometry reaches a lower drag value compared to the  $0.058w$  radius geometry.

In figure 6.1(b) the difference between  $C_D$  and  $C_{D^*}$  is plotted against  $C_\mu$ . The influence of the energy consumption of the Coanda jet is clearly visible here, as was expected based on section 2.3.2. For a four millimeter slot height, the momentum coefficient should stay below 0.05 when the compressor power is generated independent from the trucks engine. In the figure only the  $0.058w$  radius geometry is shown, however, the same effect is visible for both radii, the power corrected drag coefficient increases rapidly for increasing  $C_\mu$ . In figure 6.1(c) the energy corrected  $C_D$  is shown for both geometries, showing the more rapid increase in drag coefficient for the smaller radius geometry as  $C_\mu$  increases, but following the same trend.

The drag on the base of both systems is attributed mainly by two phenomena; the suction peak on the Coanda surface and the base pressure distribution imposed by the wake. The pressure peak on the Coanda surface is related to the jet flow which is attached to the surface, but at a high velocity thus creating a region of lower pressure on the curved Coanda surfaces. This is illustrated in figure 6.2, where the drag force on the base and the Coanda surfaces are shown separately. The  $F_{sum}$  is the actual force working on the complete base and equals the pressure drag force working on the complete back of the model (the momentum of the jet flow, which reduces the total force is not included in these figures for simplicity).

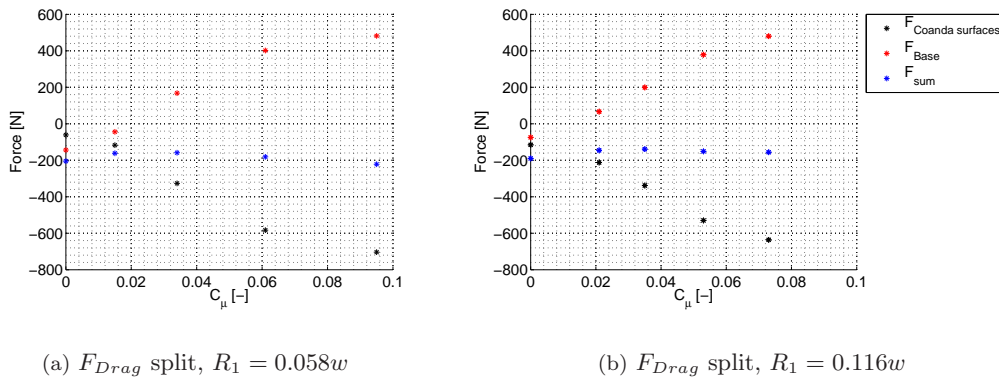


**Figure 6.2:** Drag force split for  $R_1 = 0.058w$  and  $R_1 = 0.116w$

As can be seen in above figures (6.2(a) and 6.2(b)) the suction force working on the Coanda surfaces becomes very large for high momentum coefficients and the required base pressure increase to achieve a net drag reduction (uncorrected for energy consumption) becomes large. In some cases the increase in base pressure is smaller than the decreased pressure on the Coanda surface, which leads to a system that effectively increases the total drag force. This application could be used to increase the braking capabilities of a truck as the conventional brakes could be assisted with aerodynamic braking.

## 6.4 Jet turning

The underlying principle of the Circulation Control airfoils as applied in the past ([16, 41]) is based on the attached Coanda jet even till the jet flows in opposite direction to the freestream flow on the pressure side of the airfoil. This situation exists for high momentum coefficients only and shows a significant increase in circulation and thus lift. By achieving full jet turning the shear layer could be curved inwards more rapidly and this would close the wake nearer to the base of the model and thereby increasing the average base pressure, reducing drag. It must be noted however that the drawback of the higher momentum coefficients is the power consumption of the blowing mechanism reducing the effective drag reduction. In figure 6.3 the difference between jet separation and full jet turning is shown for the  $R_1 = 0.116w$  model. It can be seen that the jet adheres to the Coanda surface for  $\theta \sim 90deg$  leading to the strongest inward curvature of the shear layer

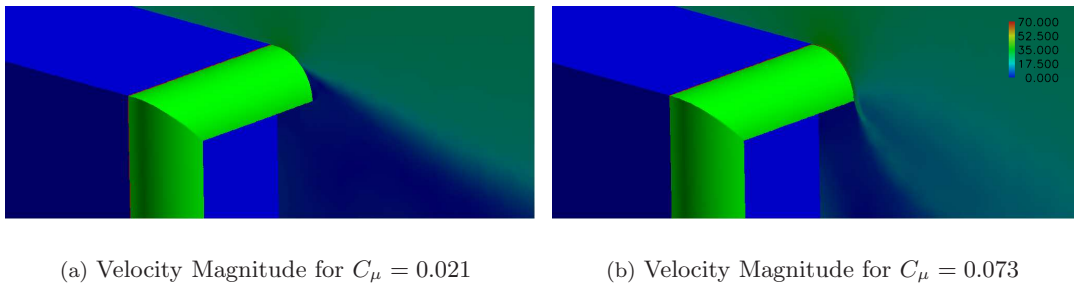


**Figure 6.3:** Jet sheet for separation for  $C_\mu = 0.021$  and flow turning for  $C_\mu = 0.073$ ,  $R_1 = 0.116w$

In the following two subsections the flow pattern in the wake for the adherent and separated jet sheet is discussed.

### 6.4.1 Full jet turning

The complete jet sheet turning leads to the maximum curvature of the shear layer and moves the vortex core closer to the base of the model. In table 6.2 the locations of the vortex cores and the saddle point are shown including the average pressure coefficients on the rear surfaces. The mean  $C_{p,base}$  is defined as the mean pressure coefficient on the base surfaces excluding the Coanda surfaces. For clarity the GETS values are shown in the table as well.

$R_1$	$C_\mu$	$C_{D^*}$	$C_D$	$\overline{C_{p,base}}$	$X_{V1}$	$Z_{V1}$	$X_{V2}$	$Z_{V2}$	$X_{SP}$	$Z_{SP}$
0.058	0.061	0.230	0.351	0.277	-	-	0.14	0.17	-	-
0.116	0.073	0.203	0.362	0.428	0.15	0.69	0.13	0.21	0.31	0.59
GETS	-	-	0.318	-0.133	0.45	0.93	0.99	0.22	2.2	0.41

**Table 6.2:** Data from 2 full jet turning simulations, coordinates expressed in  $X/W$  and  $Z/H$

The difference in drag reduction for between both geometries is due to different behavior in the wake behind the model. In the  $R_1 = 0.058w$  case the upper vortex core is no longer present resulting in a different flow pattern, as is illustrated in figure 6.4. In figures 6.4(c) and 6.4(d) a schematic projection of the vortex cores on the base is shown, indicating the difference between the two flow patterns. In the  $R_1 = 0.058w$  case the ring vortex is split on the top and the left and right middle. The three vortices trail downstream as counter rotating horse shoe vortices, where the vortex cores are forced in the corners of the base. Due to the absence of the upper vortex core also the saddle point used to estimate the location where the wake is closed is no longer present.

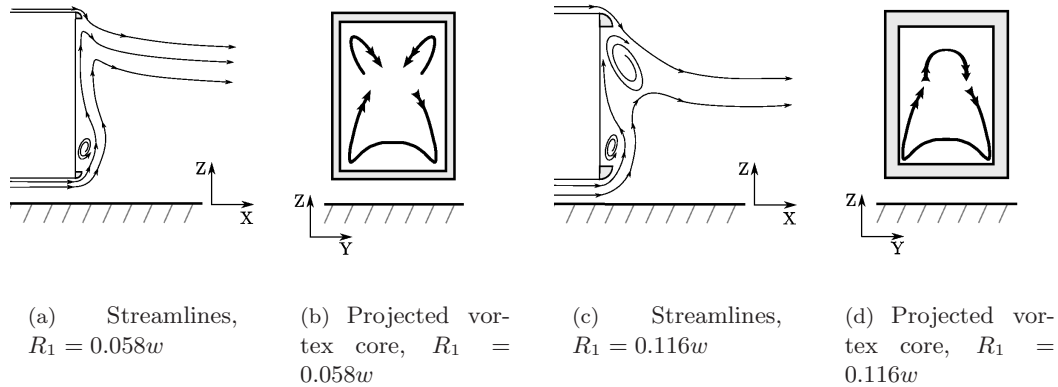


**Figure 6.4:** Flow structure in wake for  $R_1 = 0.058w$  and  $R_1 = 0.116w$

In the  $R_1 = 0.116w$  configuration the vortex core is forced closer to the base, specially in the corners on the bottom of the base, furthermore the vortex is split in two separate horse shoe vortices. In figure 6.5 the streamlines originating from the base are shown for both configurations, showing how in both cases the vortex is forced in the corners of the AFC system at the bottom and the different behavior on the upper part of the model.

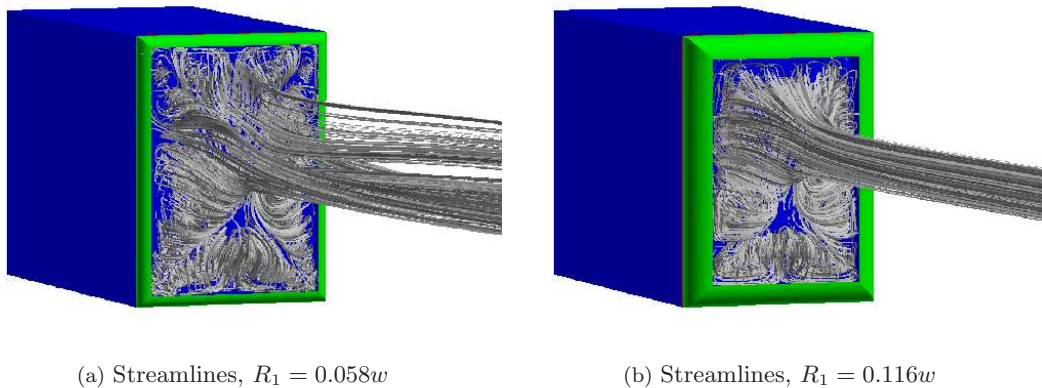


**Figure 6.5:** Streamlines originating from base for  $R_1 = 0.058w$  and  $R_1 = 0.116w$

To analyse the different behavior of the two geometries an additional simulation has been performed where for the  $R_1 = 0.058w$  geometry the velocity ratio on the lower jet sheet has been reduced to 80% of the original value, reducing the total momentum coefficient to 0.057. The goal of this simulation is to create a similar flow structure as in the  $R_1 = 0.116w$  simulations, by reducing the amount of jet turning on the lower Coanda surface. In this situation the vortex structure changes to a pattern similar to the  $R_1 = 0.116w$  simulation shown in figure 6.4(c). The  $C_{D^*}$  value in this case changes from 0.230 to 0.228, and due to the lower velocity ratio and momentum coefficient the energy corrected drag  $C_D$  improves from 0.351 to 0.334. This shows that the very strong inward curvature of the jet sheet in the small radii cases where the jet sheet adheres to the base of the model does not reduce the drag and should be prevented.

In figure 6.6 the base (including the Coanda surfaces) pressure coefficient for both cases is shown. In both cases the suction peak on the Coanda surfaces can be seen, which are caused by the jet sheet. Because these results are for the  $C_\mu \sim 0.6$  and  $\zeta \sim 2.3$  cases the jet adheres to the Coanda surfaces for  $\theta = 90deg$  and separates when the Coanda surfaces ends.

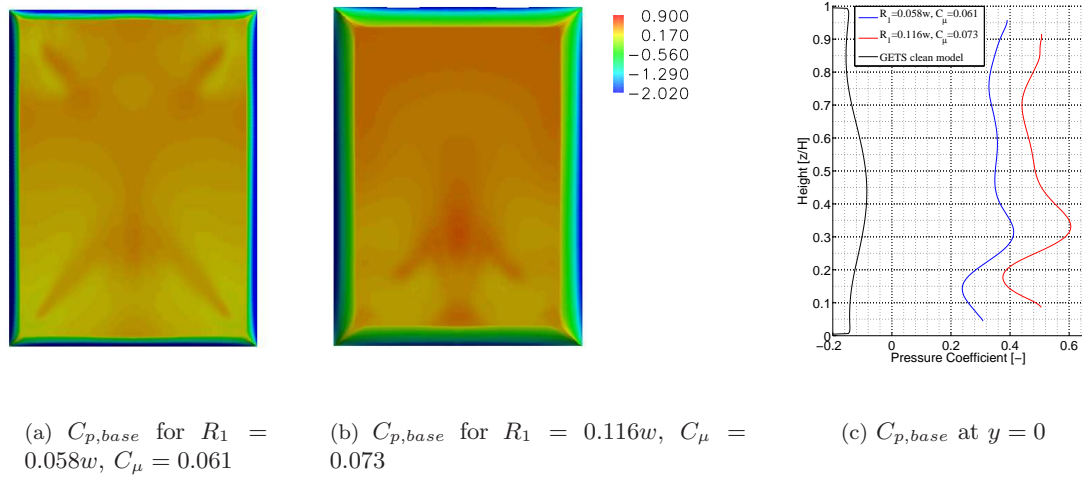


**Figure 6.6:** Base pressure coefficients for  $R_1 = 0.116w$  and  $R_1 = 0.058w$

In the base pressure coefficient contour plots (figure 6.6) the difference in vortex structures can be seen. In the  $R_1 = 0.058w$  the lower pressures on the top part of the base can be explained by the presence of the horse shoe vortex in the top corners. These horse shoe vortices are not present in the  $R_1 = 0.116w$  case and the pressure is higher in the top corners, reducing the total pressure drag on the base of the model. In figure 6.6(c) the two base pressure coefficients are compared to the pressure on the baseline GETS model. As can be seen the higher pressure on the base which is responsible for the drag reduction and the different shape of the graph indicating the effects of the vortex core.

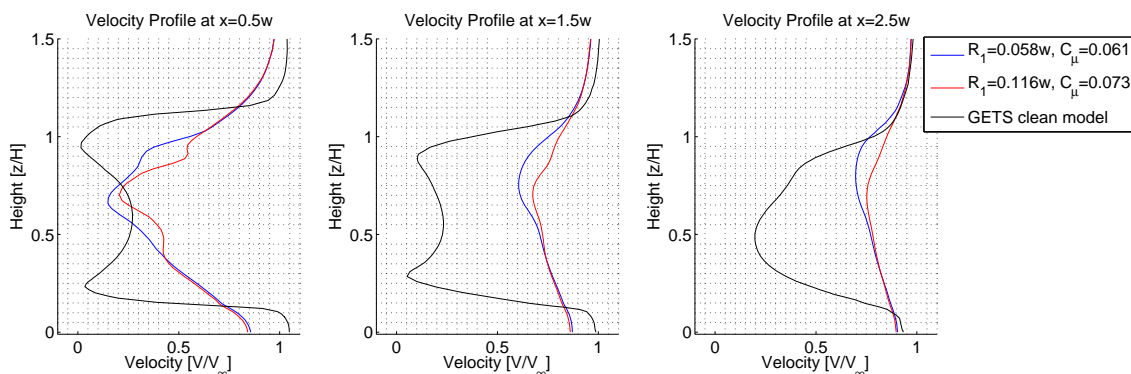


**Figure 6.7:** Velocity profiles in wake for  $R_1 = 0.058w$ ,  $C_\mu = 0.061$  and  $R_1 = 0.116w$ ,  $C_\mu = 0.073$

The difference in wake structure is further emphasized by a comparison of the velocity at different stations in the wake aft of the base of the model shown in figure 6.7. For reference the velocity profiles from the clean GETS model are also shown indicating the difference. The different vortex structure is apparent from the difference at the  $x = 0.5w$  station. Compared to the GETS velocity

profiles the wake is smaller and the wake velocity deficit smaller in case of the blown AFC systems, where the  $R = 0.116w$  case shows a smaller and more symmetric with the  $Z = 0.5h$  plane compared to the  $R = 0.058w$  geometry.

The inward curvature of the shear layers can be seen in figure 6.8 where the velocity magnitude in the  $y = 0$  and  $z = 0.5H$  is shown for the  $R = 0.0058w$  case. The velocity magnitude is similar for the  $R = 0.116w$  case and is therefore not separately displayed. The velocity magnitude clearly shows the small size of the wake compared to the wake of the GETS model which is shown in figure 5.13.

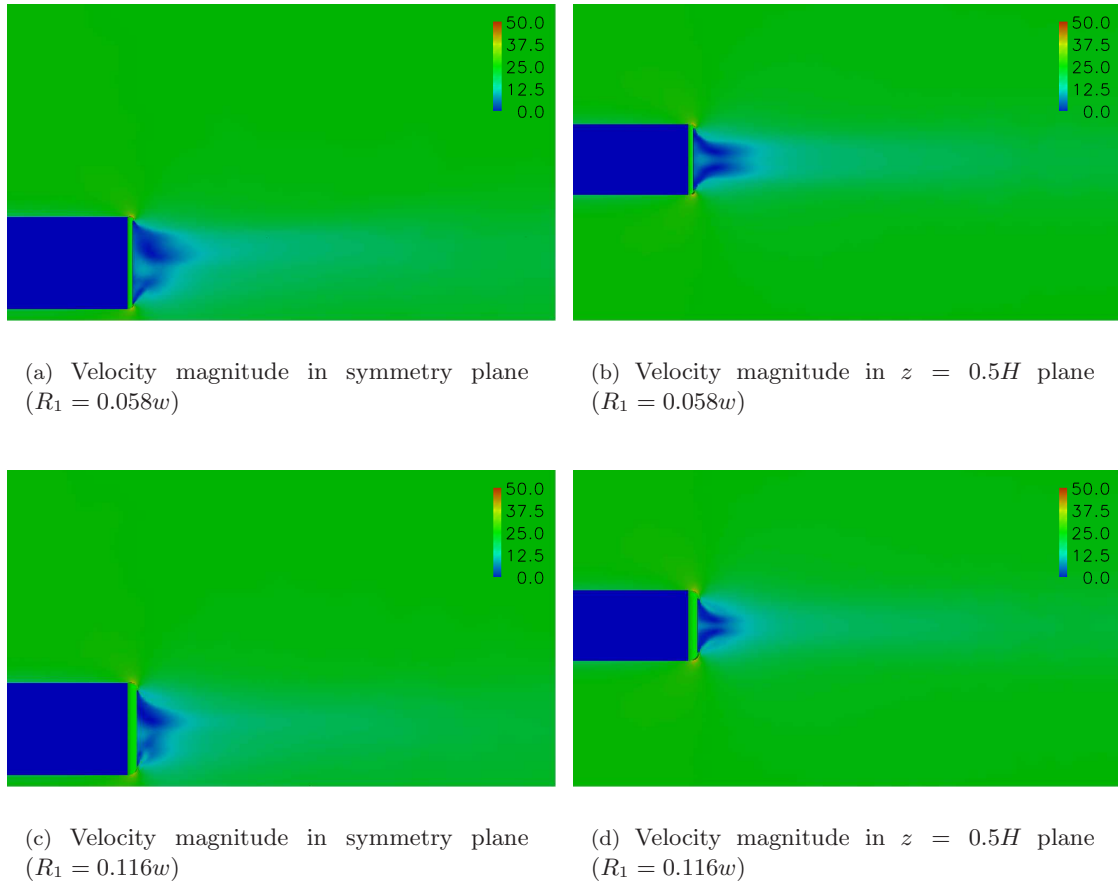


**Figure 6.8:** Velocity magnitude for both radii (full jet turning)

### 6.4.2 Jet separation

Most of the simulations performed on the AFC system experience separated flow on the Coanda surfaces. In order to have the flow remain attached in the strong adverse pressure gradient on the Coanda surface the velocity ratio needs to be in the order of  $\zeta \sim 3$  which leads to a high energy consumption. The jet velocity reduces as the distance traveled ( $s = R \cdot \theta$ , see figure 6.9) on the Coanda surface increases, due to mixing with the separated boundary layer from the GETS and the adverse pressure gradient. Therefore larger radius geometries will require a higher velocity ratio for the flow to remain attached.

As smaller radius geometries endure a higher adverse pressure gradient, also a higher velocity ratio is needed. However, this higher  $\zeta$  leads to an increased centrifugal force ( $F_c \sim \frac{\rho V_{jet}^2}{R}$ ) working on the fluid and can also lead to initial separation (the jet sheet is blown past the surface) from the Coanda surface, smaller radius enhances this effect. This effect is also related to the velocity inlet geometry and this is why the geometry shown in figure 4.13(c) from section 4.4.1 is used to model the velocity inlet.

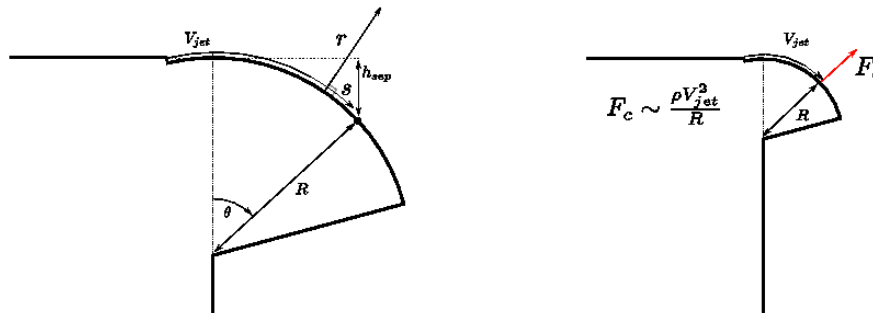


Figure 6.9: Large (left) and small (right) radius geometry

The  $C_D$  and  $C_{D^*}$  values are more equal compared to the attached jet sheet simulations due to the lower momentum coefficient and velocity ratio and the related energy consumption. For the  $R_1 = 0.058w$  and  $R_1 = 0.116w$  geometries the simulations with equal momentum coefficient and blowing ratio are tabulated in table 6.3, the first two rows are the results for the separated jet simulations, the third and fourth row are the results of the full jet turning simulations and as reference the GETS model values are given in the fifth row.

$R_1$	$C_\mu$	$C_{D^*}$	$C_D$	$C_{p,base}$	$X_{V1}$	$Z_{V1}$	$X_{V2}$	$Z_{V2}$	$X_{SP}$	$Z_{SP}$
0.058	0.034	0.244	0.287	0.118	0.23	0.83	0.19	0.15	0.64	0.52
0.116	0.035	0.232	0.274	0.177	0.23	0.78	0.33	0.19	0.61	0.53
0.058	0.061	0.230	0.351	0.277	-	-	0.14	0.17	-	-
0.116	0.073	0.203	0.362	0.428	0.15	0.69	0.13	0.21	0.31	0.59
GETS	-	-	0.318	-0.133	0.45	0.93	0.99	0.22	2.2	0.41

Table 6.3: Data from two jet separation simulations, coordinates expressed in  $X/W$  and  $Z/H$

As can be seen in the table, the  $R_1 = 0.116w$  geometry has the lower drag coefficient for lower momentum coefficients, mainly caused by a higher base pressure coefficient. The jet sheet curves the wake inwards and the wake closes significantly closer to the base compared to the clean GETS model. The  $R_1 = 0.116w$  geometry saddle point is located slightly closer to the base compared to the  $R_1 = 0.058w$  geometry however compared to the clean model both are approximately  $1.6w$  closer to the base. The heights of the vortex cores is in both cases at a distance of approximately

$0.1w$  away from the end of the Coanda surface. The longitudinal location of the lower vortex core is further from the base in the  $R_1 = 0.116w$  case, while the upper vortex cores are at a similar location for both geometries.

In figure 6.11 the velocity profiles in the symmetry plane of the model on the upper and lower Coanda surface are shown. The  $r$  coordinate is perpendicular to the Coanda surface (see figure 6.9) and is expressed in  $r/W$ . The velocity displayed is the absolute velocity magnitude, which implies that the reverse flow (negative velocity) is not clearly visible, as only absolute values are shown.

In both cases the jet sheet is decelerated as it mixes with the shear layer and the jet sheet grows in thickness. At the  $\theta = 0deg$  station the jet sheet equals has the slot height thickness of  $1.13 \cdot 10^{-3}H$  and the complete boundary layer is accelerated by the jet sheet. This acceleration is visible upstream of the AFC system, as the boundary layer profile upstream of the blowing system is fuller compared to the velocity profile of the clean GETS model. See figure 6.10 for a comparison for the boundary layer of the GETS and the AFC ahead of the  $x = L$  location.

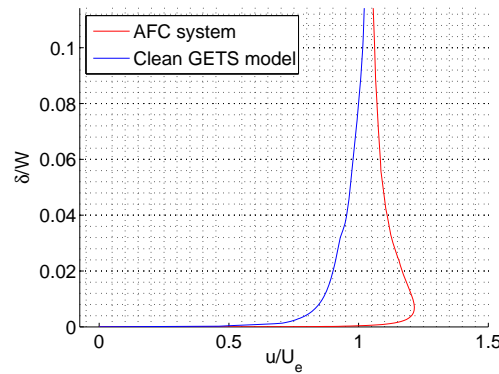


**Figure 6.10:** Boundary layer comparison at  $x = L, y = 0$  (top side)

The velocity ratio for both geometries equals 1.8, however the highest velocity at (at  $\theta = 0deg$ ) is approximately 2.3 for the  $R_1 = 0.058w$  case and 2 for the  $R_1 = 0.116w$  geometry. The jet sheet is accelerated between the boundary layer developing on the Coanda surface and the the shear layer originating from the GETS model. This results in the flow being accelerated to a higher velocity then the blowing velocity, before being decelerated by the adverse pressure gradient and the shear layer mixing.

For the  $R = 0.058w$  geometry the jet sheet separates at approximately  $\theta = 67deg$  (from the graphs  $60 < \theta < 75deg$ ) on both the top and bottom side, the bottom side separates earlier compared to the top side. The  $R = 0.116w$  separates before  $\theta = 60deg$  where the jet sheet also separates earlier on the bottom surface compared to the top Coanda surface. The earlier separation on the bottom side is explained by the higher velocity underneath the model due to the ground effect. This higher velocity results in a lower pressure under the model and thus a higher adverse pressure gradient on the Coanda surface. This higher adverse pressure gradient leads to earlier separation on the bottom side.

Although the jet sheet separates at a larger angle for the  $R = 0.058w$  geometry the final drag value is higher compared to the larger radius geometry. This is related to the effect that the shear layer is curved more inwards due to the larger radius. The distance from the separation point to the plane where the shear layer originates from (the GETS sides) is determined from

$$h_{sep} = R_1(1 - \cos(\theta)), \text{ (for } R_1 = R_2) \quad (6.3)$$

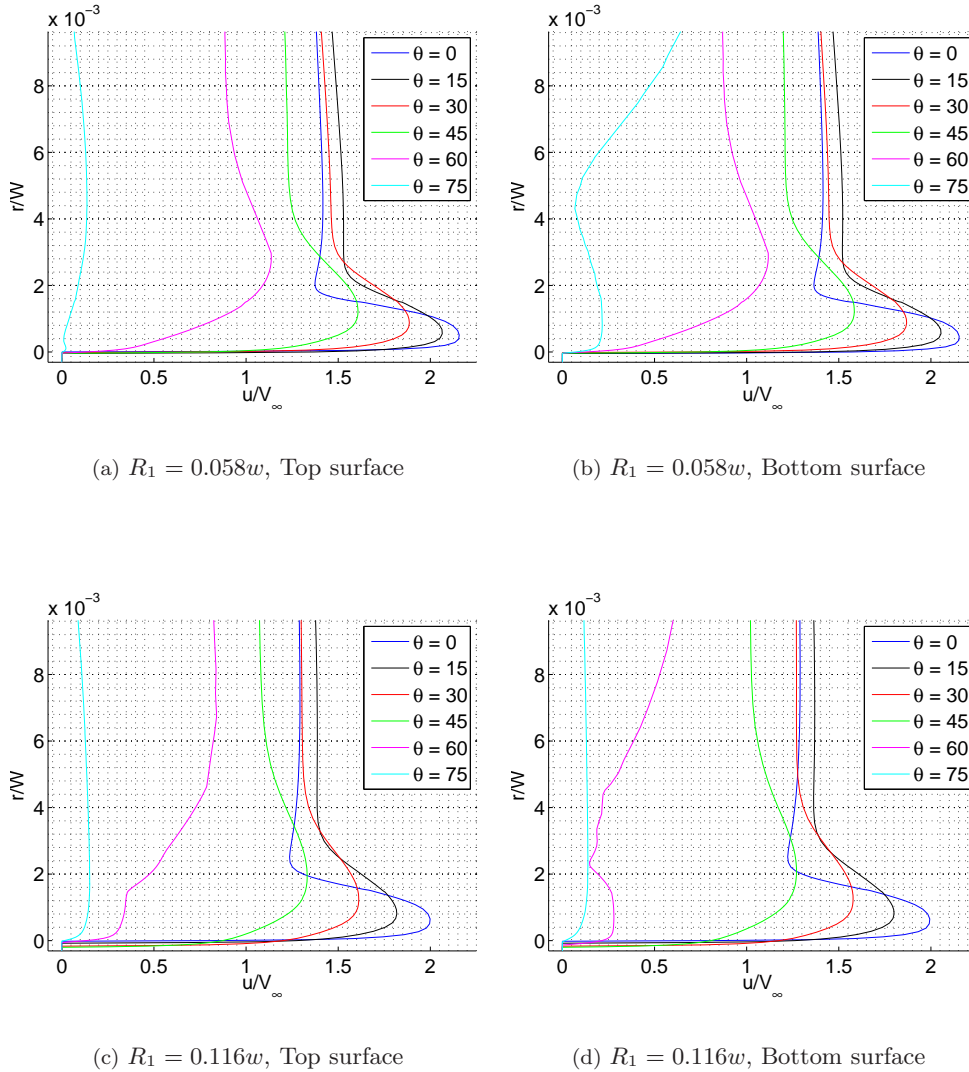


**Figure 6.11:** Velocity profiles in symmetry plane,  $C_\mu = 0.035$

(see figure 6.9) and indicates the amount the shear layer has curved inwards, as after the jet sheet separates the shear layer curves inwards at a smaller rate. The larger radius leads to the observation that for the larger radii geometries with equal amount of jet sheet turning the larger radii geometries yield a larger drag reduction. In the above figures only the top and bottom Coanda surfaces have been shown, for the side surface the same observations hold, and the jet sheet flow and the separation is similar to the top surface.

The separation angle on the Coanda surfaces is uniform over the width of the model, except for the corners of the model. Where the Coanda surfaces coincide with each other the flow separates from the surface at a smaller angle. This separation causes a trailing vortex originating from the corner of the model, at the intersection of the Coanda surfaces. These edge vortices are displayed in figure 6.12 and merge with the main vortex structure downstream.

The resulting vortex structure differs from the GETS model and both of the attached jet sheet structures. The ring vortex core is split in two separate horse shoe vortices, which merge with the edge vortices originating from the four corners of the model. In figure 6.13 the streamlines

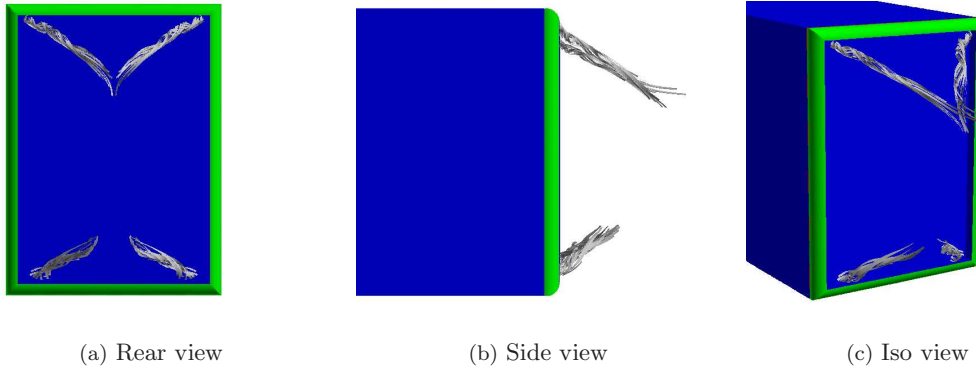


**Figure 6.12:** Edge vortices originating from Coanda surface intersection,  $R_1 = 0.058w$

and projected vortex pattern is shown. The pattern is similar for both the  $R_1 = 0.058w$  and the  $R_1 = 0.116w$  models.

The resulting wake structure is more symmetric with the  $Z = 0.5H$  plane compared to the clean and attached jet sheet simulations. Although the lower vortex core is moved downstream in for the  $R = 0.116w$  the heights of the vortex cores are symmetric and the difference between both cases is approximately equal to the difference in the  $R_1$  radii of both geometries. The vortex core is further downstream of the base compared to the attached jet sheet cases and the resulting base pressure is lower, one of the causes of the smaller drag reduction achieved in the separated flow cases. In figure 6.14 contour plots of the the pressure coefficient on the base of the model is shown and the pressure coefficient on the base in comparison with the clean model in figure 6.14(c).

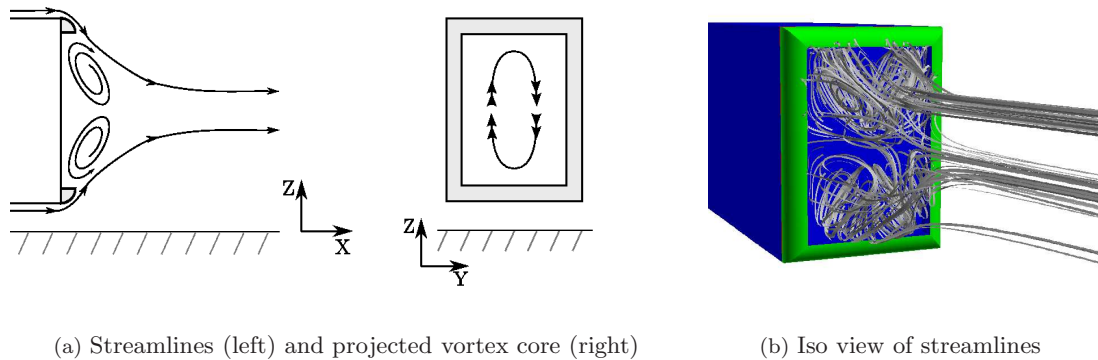


**Figure 6.13:** Streamlines and projected vortex core,  $R_1 = 0.116w$

In both the contour plot and the figure in figure 6.14(c) the increased base pressure of the  $R_1 = 0.116w$  configuration is visible. The pressure distribution compared the GETS model pressure is also shown, where the highest pressure is present at  $z/H \sim 0.45$ . The shape and symmetry (with respect to the  $z = 0.5H$  plane) of the flow structure is visible for both geometries.

As the vortex cores are closer to the base compared to the clean model the wake closes quicker as well, which is visible in the velocity profiles at  $0.5w$ ,  $1.5w$  and  $2.5w$  aft of the base in figure 6.15. The velocity profile in the first station at  $0.5w$  shows how the the minimum velocity in the wake is not increased as it is in the case of the not separated jet sheet (figure 6.7), but the height over

which the minimum velocity spans the base is much smaller compared to the clean model without the AFC system.

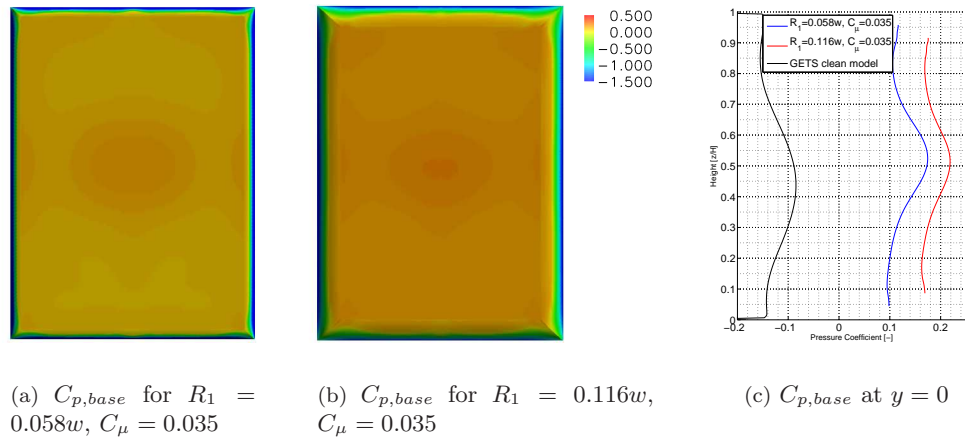


**Figure 6.14:** Base pressure coefficients for  $R_1 = 0.058w$  and  $R_1 = 0.116w$

In figure 6.16 the velocity magnitude in two cut planes is shown for the case where the jet sheet separates from the Coanda surface. The inward curvature of the shear layers is still visible, but not as pronounced as in the full jet sheet turning cases. The difference in between the curvature of both shear layers is shown in figure E.9 where the vorticity of the fully turned and separated jet sheets are compared to each other and the shear layer separating from the GETS model.

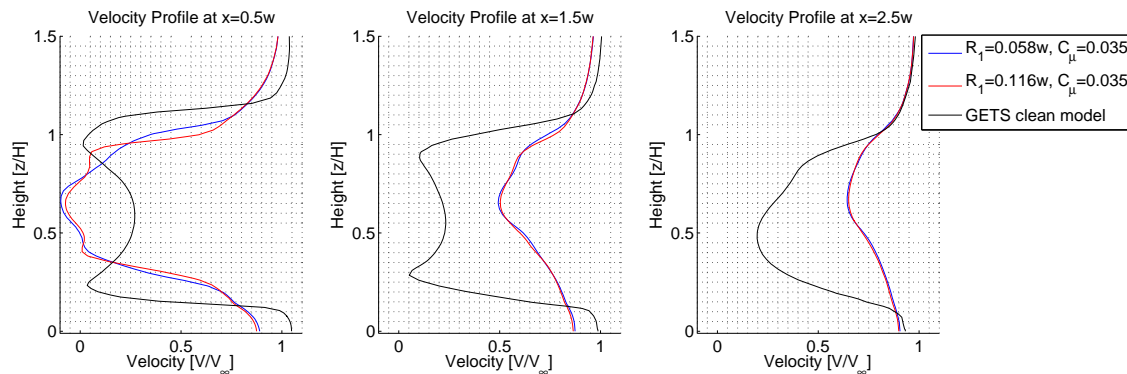
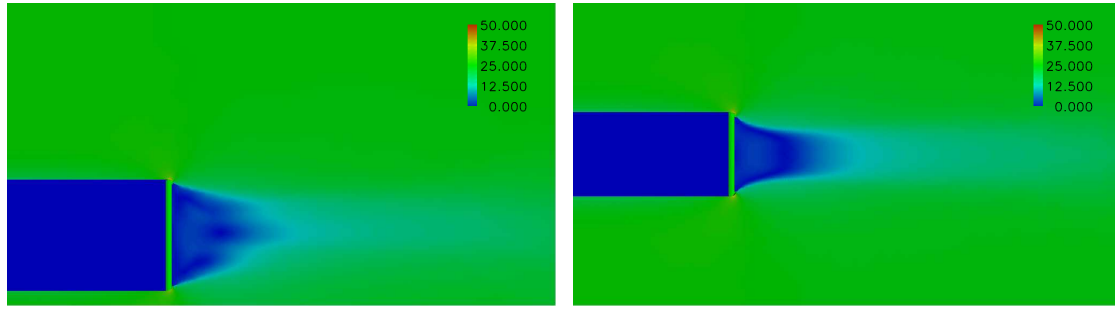


**Figure 6.15:** Velocity profiles in wake for  $R_1 = 0.058w$ ,  $C_\mu = 0.061$  and  $R_1 = 0.116w$ ,  $C_\mu = 0.073$

For a more detailed overview of the jet sheet turning and jet sheet separation results in comparison with the GETS model see figures E.9, E.10 and E.11 in appendix E indicating the differences in the wake.



(a) Velocity magnitude in symmetry plane

(b) Velocity magnitude in  $z = 0.5H$  plane**Figure 6.16:** Velocity magnitude for  $R_1 = 0.058w$  (jet separation)

## 6.5 Geometric variations

Besides the momentum coefficient which mainly determines whether the jet sheet remains attached or separates, the system is also influenced by geometric alterations which influence the adverse pressure gradient which is present on the Coanda surface. Different geometric modifications are simulated and discussed below.

### 6.5.1 Slot height variation

It is hinted in [15] that the slot height can be of significant influence on the final drag coefficient. As the smaller slot heights require higher velocity ratios for equal momentum coefficients the required power will increase more rapidly with increasing momentum coefficient as the slot height decreases. In order to verify this hypothesis both geometries were also simulated with a slot height of 2 and 6 mm. Smaller slot heights are unwanted due to the practical implications of a  $< 2\text{mm}$  slot on a full scale truck (dirt accumulation, production tolerances) therefore 2mm is used as a minimum. For slots larger than 6mm and requiring  $\zeta > 1$  the momentum flow and associated required power becomes too large for practical applications.

In figure 6.17 it can be noted that the maximum momentum coefficient is lower for the smaller slot heights. This is explained by the fact that  $C_\mu$  is proportional to  $\zeta^2$ , while the power required is proportional to  $\zeta^3$ . To achieve the same momentum coefficient with a smaller slot height the required power increases significantly, beyond the level where an aerodynamic gain is made. It can be seen in the above figure that the  $C_{D^*}$  reduction is similar for both the  $0.75 \cdot 10^{-3}w$  and  $1.5 \cdot 10^{-3}w$  slot heights at increasing momentum coefficients. The results of the  $2.3 \cdot 10^{-3}w$  height differ significantly from the smaller slot heights and the small reduction in drag changes to an increase in  $C_D$  when the compressor power is included in the calculation.

The full results for simulations with slot height variation can be found in table E.3 in appendix E. For the compared simulations of the  $R_1 = 0.116w$  radius the drag coefficients and the locations of the vortex cores and saddle point can be found in table 6.4. The  $R_1 = 0.116w$  radius is used as it performs better compared to the smaller radius geometry as can be seen in figures 6.17(a) and 6.17(b). The  $0.75 \cdot 10^{-3}w$  slot height is not simulated for high momentum coefficients as the velocity ratio required to keep the momentum coefficient equal leads to velocities close to  $M \sim 0.3$ , which are not accurately simulated by the incompressible solver.

From the table several observations can be made for both the low and high momentum cases. At the lower momentum coefficient the velocity ratio is the critical factor as it determines the separation angle on the Coanda surface. The flow with the lower velocity ratio separates first and

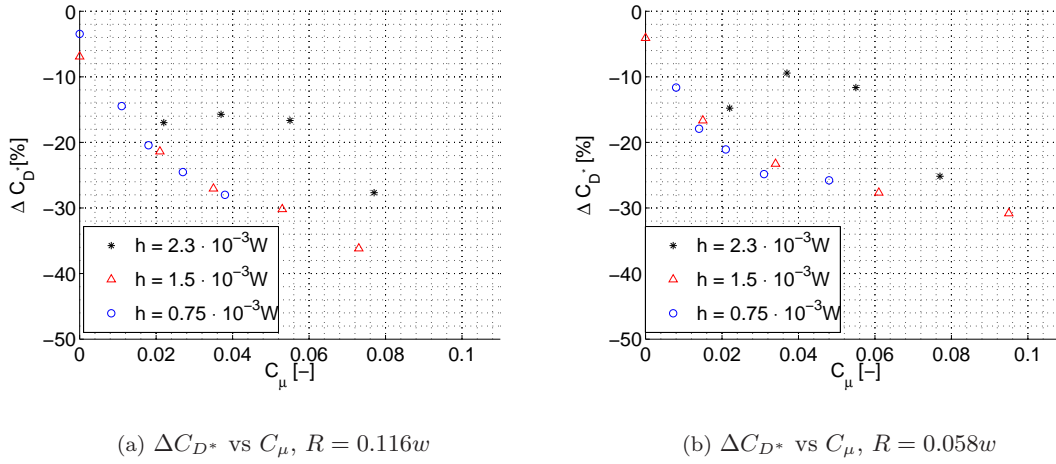


**Figure 6.17:** Slot height variation for  $R = 0.116w$  and  $R = 0.058w$

this leads to a smaller reduction in wake size. This can be seen for the  $2.3 \cdot 10^{-3}w$  case where  $\zeta = 1.4$  and the saddle point is  $0.4w$  located further downstream compared to the two smaller slot heights. The resulting base pressure is lower for the larger slot height leading to a smaller drag reduction. It must be noted that due to the lower velocity ratio the required power to generate the jet sheet is lower compared to the other simulations. When this is taken into account the lower  $\zeta$  solution would lead to the most efficient system of the five cases considered in this section.

$h(10^{-3})$	$C_\mu$	$\zeta$	$C_{D^*}$	$C_D$	$C_{p,base}$	$X_{V1}$	$Z_{V1}$	$X_{V2}$	$Z_{V2}$	$X_{SP}$	$Z_{SP}$
0.75	0.038	2.6	0.229	0.388	0.201	0.24	0.78	0.39	0.21	0.61	0.53
1.5	0.035	1.8	0.232	0.274	0.177	0.29	0.74	0.34	0.19	0.61	0.53
2.3	0.033	1.4	0.253	0.267	0.033	0.22	0.78	0.29	0.21	0.92	0.46
1.5	0.073	2.6	0.203	0.362	0.428	0.15	0.69	0.13	0.21	0.31	0.59
2.3	0.077	2.2	0.230	0.388	0.223	0.12	0.78	0.14	0.33	0.30	0.57
GETS	-	-	-	0.318	-0.133	0.45	0.93	0.99	0.22	2.20	0.41

**Table 6.4:** Data for slot height variation, coordinates expressed in  $h/W$ ,  $X/W$  and  $Z/H$

At higher momentum coefficients the jet sheet is completely turned for both slot heights as can be seen in the rapid closure of the wake ( $0.30w$  downstream of the base). The resulting base pressures differ significantly, with the higher base pressure for the  $1.5 \cdot 10^{-3}w$  slot height, which is remarkable as in both cases there is complete jet sheet turning. Both simulations show the double horse shoe vortices (see figure 6.4(c)) as described for the full jet turning case for  $R_1 = 0.116w$ . The difference is that the upper vortex core is lower in the  $h = 1.5 \cdot 10^{-3}w$  case and the lower vortex is more forced in the lower corners at the intersection of the Coanda surface with the base, it is unclear how this influences the resulting base pressure and difference in  $C_{D^*}$

### 6.5.2 Radius variation

By varying the radius of the Coanda surface the separation of the jet sheet and the curved base flaps effect can be influenced. A smaller radius would decrease the surface area which is subjected to the negative pressure in the jet, reducing the drag increasing suction area. On the smaller radius geometry the adverse pressure gradient is larger, requiring a higher velocity ratio and thus more energy. Increasing the radius is expected to improve the performance in the unblown case as the the Coanda surfaces act as curved base flaps [27] which deflect the shear layers by means of streamlining the flow coming from the back of the clean model. The slot height in these simulations is  $h = 1.5 \cdot 10^{-3}w$  for all geometries, however the slot height appeared to be slightly less for the  $R_1 = 0.173w$  simulations during post processing, due to an error in the grid generation process. For a tabulated overview of all the results of the  $R_1 = 0.039w$  and  $R_1 = 0.173w$  see appendix E. For low and high momentum coefficients the results are tabulated in table 6.5.

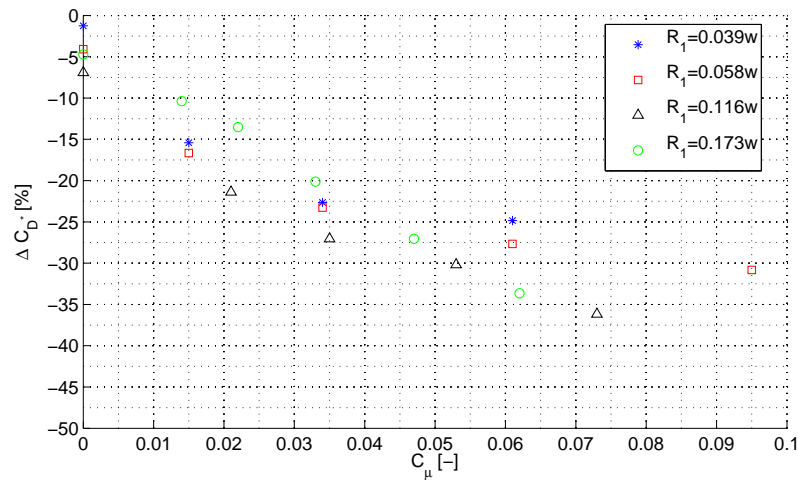


Figure 6.18:  $\Delta C_{D^*}$  vs  $C_\mu$  for various radii

In figure 6.18 the uncorrected drag coefficient is shown for different radii and increasing momentum coefficient. It can be seen that the expected advantage of the  $R_1 = 0.173w$  geometry at zero jet velocity ( $C_\mu = 0$ ) due to the stream lining is not present. The smaller  $R_1 = 0.116w$  radius configuration performs better when blowing is absent.

$R_1$	$C_\mu$	$\zeta$	$C_{D^*}$	$C_D$	$C_{p,base}$	$X_{V1}$	$Z_{V1}$	$X_{V2}$	$Z_{V2}$	$X_{SP}$	$Z_{SP}$
0.039	0.015	1.2	0.265	0.270	-0.048	0.23	0.80	0.33	0.16	1.24	0.45
0.173	0.014	1.4	0.285	0.300	0.005	0.43	0.79	0.49	0.19	0.95	0.46
0.039	0.073	2.4	0.239	0.360	0.207	0.32	0.74	0.21	0.19	0.29	0.53
0.173	0.062	3.0	0.211	0.465	0.246	0.13	0.76	0.33	0.27	0.56	0.43
GETS	-	-	-	0.318	-0.133	0.45	0.93	0.99	0.22	2.20	0.41

Table 6.5: Data for radius variation, coordinates expressed in  $R_1/W$ ,  $X/W$  and  $Z/H$

For lower momentum coefficients the  $R_1 = 0.039w$  geometry performs similar to the larger  $R_1 = 0.058w$  and  $R_1 = 0.116w$  geometries except at  $C_\mu = 0$ , which can be explained by the high curvature of the geometry, which reduces the effectiveness of a base flap [27]. The  $R_1 = 0.173w$  geometry lowers the drag coefficient by a smaller amount because the adverse pressure gradient causes the jet sheet to separate at a certain distance from the velocity inlet. Due to the larger

radius this distance is at a smaller  $\theta$  compared to the smaller geometries and results in a reduced inwards curvature of the shear layers.

For higher momentum coefficients the  $R_1 = 0.039w$  geometry results in the smallest drag reduction and differs from the trend the two largest radii geometries follow. The jet sheet remains attached in this simulation, and the saddle point in the symmetry plane is close to the base, indicating a very small wake. The base pressure is not as high compared to the pressure achieved with the  $R_1 = 0.116w$  model and this is the reason for the relatively high drag coefficient. This is the same phenomena as observed in the  $R_1 = 0.058w$  geometry case with high momentum coefficients. Instead of two horse shoe vortices in the wake (one in top and one in the bottom half of the base), the upper horse shoe vortex is split in two separate vortices, which counter rotate as they move downstream. The vortices turning points are forced in the corners of the base which is one of the reasons the base pressure is lower compared to the larger radii geometries where only the lower vortex is forced in the corners, the turning point of the upper vortex is located further from the base.

The large  $R_1 = 0.173w$  geometry performs according to the trend, however in this case full jet turning is not achieved at the high momentum coefficient, explaining the further downstream location of the saddle point. The base pressure is higher compared to the  $R_1 = 0.039w$  geometry, but the larger Coanda surface contributes for a larger part to the total drag due to the increased projected area and the negative pressure in the jet sheet. This causes the rearward suction drag on the Coanda surface to be the largest for the  $R_1 = 0.173w$  geometry.

### 6.5.3 Angle variation

The angle the Coanda surface makes with the base plane can also be varied in the grid definition process and can influence the final results. This has not been analysed due to some difficulties experienced with the grid generation. The underlying principle of the Coanda effect, the jet sheet turning in order to curve the shear layer inwards furthermore requires the angle to be in the order of  $\theta = 90deg$  which has been used in all simulations. It is assumed that for simulations where the jet is not completely turned (the lower momentum coefficients) the angle of the Coanda surface has a small influence as the vortex cores are located relatively far from the base and they will not interact with Coanda surface.

The vortex does interact in the small radii, high momentum coefficient simulations, where the vortex is forced in the corner the Coanda surface makes with the base. These cases require full jet sheet turning and it would be more interesting to simulate angles of more than 90 degrees. This option was however not included in the grid generation process.

## 6.6 Design optimization

The results achieved up till now with the different momentum coefficients and geometric variations lead to the following observations in terms of maximum drag reduction:

- Higher momentum coefficients yield more jet sheet turning and increased base pressure.
- Slot heights between  $0.75 \cdot 10^{-3}w < h < 1.5 \cdot 10^{-3}w$  give the best results for equal momentum coefficient.
- At comparable momentum coefficient the  $0.116w$  radius leads to the lowest drag value. Smaller radii increase drag due to altered vortex structure, large radii increase drag due to increased surface area (and the resulting negative pressure in the jet sheet).

When the power consumption of the blown system is taken into consideration, the results differ due to the high power consumption of the high momentum coefficient jet sheet. For a compressor inlet  $C_p$  of 0.7 the results can be summarized as follows:

- For the simulated slot heights the momentum coefficient should be below  $C_\mu < 0.030$  to reduce power consumption, while benefiting from maximum jet sheet turning.
- The velocity ratio is optimal within  $1 < \zeta < 1.5$ .
- The  $0.116w$  radius geometry is the best combination between the curved base flaps effect and the jet sheet turning.

The velocity ratio requirement is related to the momentum coefficient and the slot height. Reducing the slot height requires a higher velocity ratio for an equal momentum coefficient, which requires more power, as  $C_\mu \sim \zeta^2$  and  $P_{req} \sim \zeta^3$ . For power requirements the velocity ratio should be kept low, however too low leads to the effect that the jet sheet no longer adheres to the Coanda surface and does not entrain the shear layer no longer causing the shear layers to curve inwards.

To illustrate the window of  $C_\mu$  and  $\zeta$  range all the results (of all simulations) are plotted in a contour plot where the color indicates the power corrected drag value (for  $C_{p,inlet} = 0.7$ ) in figure 6.19. The data points are interpolated using a cubic interpolation method, and no extrapolation is applied. In this plot it can be seen that the smallest drag value occurs at  $0.010 < C_\mu < 0.030$  and  $0.8 < \zeta < 1.5$ . (note that the drag reduction at  $\zeta = 0.8$  is mainly due to curved base flaps effect, not due to the Coanda effect) The smallest drag value found is for the  $0.116w$  radius geometry with a momentum coefficient of 0.021 and a velocity ratio of 1.4, (corresponding to a slot height of  $1.5 \cdot 10^{-3}w$ ) the drag coefficient for this configuration equals 0.270, which is 15% reduction compared to the clean GETS drag coefficient of 0.3180. Applied to a full scale truck this would lead to a reduction of fuel consumption of 5 to 7.5%.

Based on the limitations set by the energy requirements on the velocity ratio and the geometric effect of curved base flaps a series of simulations have been performed where the ratio  $R_1/R_2$  is varied for different momentum coefficients. As the slot height is kept fixed at  $1.5 \cdot 10^{-3}w$ , the velocity ratio varies with  $\zeta \sim \sqrt{C_\mu}$  (using 2.4). The following range of parameters is studied using the baseline geometry of the most efficient configuration obtained previously:

	$R_1$	$h$	$R_2/R_1$	$C_\mu$	$\zeta(C_\mu)$
Range	0.116	$1.5 \cdot 10^{-3}$	0.8 – 1.6	0 – 0.26	0 – 1.53

**Table 6.6:** Parameter range for design optimization, expressed in  $R/W$  and  $h/W$

The velocity ratio is explicitly mentioned in table 6.6 as it is a critical parameter for the total energy consumption of the complete system. To limit the total length of the Coanda surface to

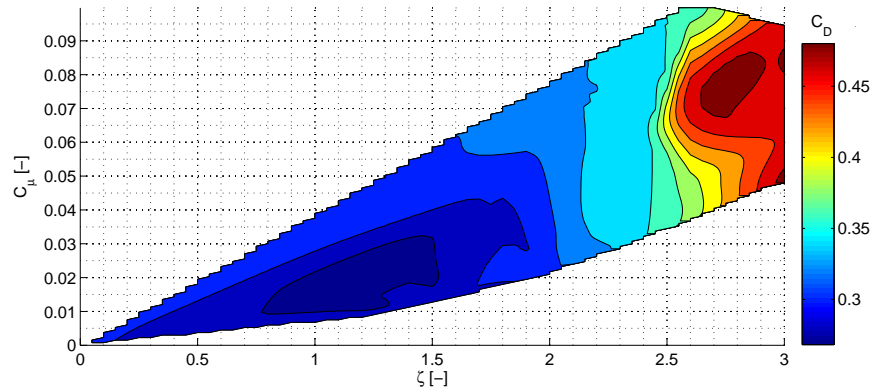
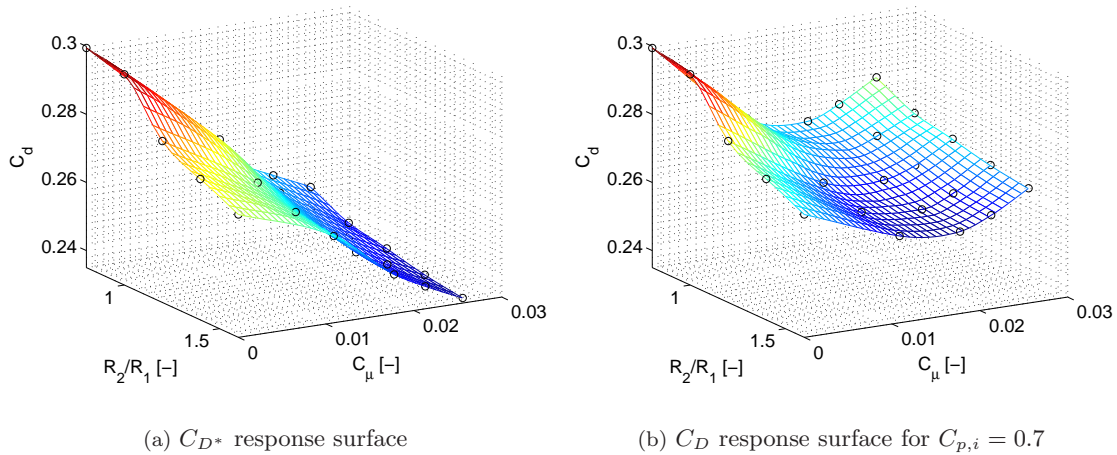


Figure 6.19:  $C_\mu$  vs  $\zeta$  colored by  $C_D$

approximately 0.5 meters the maximum  $R_2/R_1$  ratio is limited to 1.6. The 0.5 meter is well within the European Legislation which allows for devices to extend 0.6 meters aft of the trailer.

The two parameters are varied in the CFD simulations for various combinations in order to construct a complete response surface, the full results of the parameter variation can be found in appendix E in table E.5.



(a)  $C_{D^*}$  response surface

(b)  $C_D$  response surface for  $C_{p,i} = 0.7$

Figure 6.20: Response surfaces for  $C_{D^*}$  and  $C_{D,0.7}$

In figure 6.20 two response surfaces are shown for  $C_{D^*}$  and  $C_D$  for an inlet pressure coefficient of 0.7. The response surface is a cubic interpolation of the data points resulting from the CFD simulations, which are indicated by the black circles in the figures. From the two figures the significant difference between the  $C_{D^*}$  and the  $C_D$  values can be seen. The impact of the power consumption of the Coanda system is significant and influences the optimal configuration. Without taking into account the power consumption the response surface shows a decrease in drag coefficient for increasing radius ratio and momentum coefficient. The sensitivity of  $C_{D^*}$  for the momentum coefficient is larger compared to the radius ratio, showing that the momentum coefficient is the most influential parameter for the drag reduction. In case of the power corrected drag coefficient, the increase in momentum coefficient leads to decrease in drag, until the required power becomes

too large and the configuration no longer yields a net drag reduction. In the situation where the compressor inlet pressure coefficient equals 0.7 the maximum drag reduction compared to the clean GETS drag coefficient equals 18%, which would lead to a 6 to 9% reduction in fuel consumption.

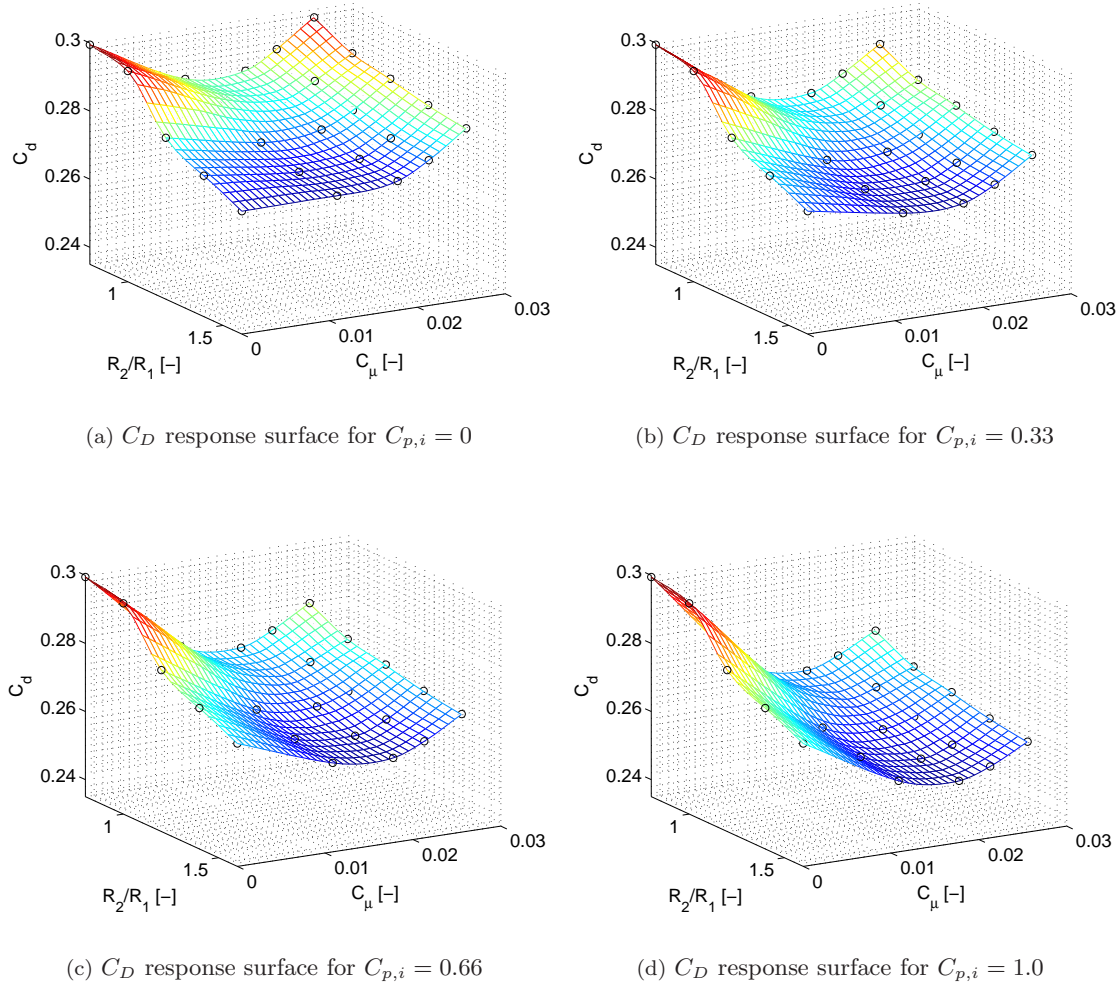


**Figure 6.21:** Response surfaces for  $C_D$  for increasing  $C_{p,i}$

In figure 6.21 the response surfaces are shown for an increasing compressor inlet pressure coefficient, ranging from zero ( $p_{inlet} = p_{\infty}$ ) till one in case of the inlet at the stagnation point ( $p_{inlet} = p_{\infty} = q_{\infty}$ ). The compressor efficiency used for these surfaces equals 35%, similar to values used in [21]. As can be seen in the figure the shape of the response surface varies significantly with  $C_{p,i}$ , in the least efficient case ( $C_{p,i} = 0$ ) the most efficient configuration is without the AFC system activated, merely using the curved base flaps effect to reduce drag. In table 6.7 the different results for the best configurations are summarized for different values of  $C_{p,i}$ .

From the table the maximum drag reduction found is 20% for the configuration applied to the clean GETS model, which would lead to a fuel consumption reduction of 7 to 10%. The influence of compressor inlet pressure is visible in the inefficient case where the inlet pressure equal freestream pressure, as the power required for the blowing mechanism is larger than the power saved by reducing the drag coefficient. The drag reduction is solely achieved by boat tailing the geometry. This effect is illustrated in figure 6.22 where the radius ratio is compared to a typical boat tail

$C_{p,i}$	$C_\mu$	$\zeta$	$R_2/R_1$	$C_{D^*}$	$C_D$	$\Delta C_D$
0	0	0	1.6	0.2711	0.2711	-14.7%
0.33	0.011	1.0	1.6	0.2605	0.2662	-16.2%
0.66	0.018	1.28	1.6	0.2465	0.2599	-18.3%
1.0	0.018	1.28	1.6	0.2465	0.2531	-20.4%

**Table 6.7:** Design optimization results for different compressor inlet pressures

with a ten degrees slant angle. The 10 degree slant angle represents the boat tail geometry where the flow stays attached to the boat tail [53]. A higher slant angle  $> 10$  degrees will cause the flow to separate from the boat tail. The larger the radius ratio the more the Coanda surface represents a boat tail geometry. Increasing the radius ratio will reduce drag as the system will function as a boat tail, the effect of the jet sheet curvature is reduced for larger radii, as the the jet sheet mixes with the shear layer before curving the latter inward, a similar effect observed for the large radius ( $R_1 = 0.173w$ ) geometry simulated in section 6.5.2.

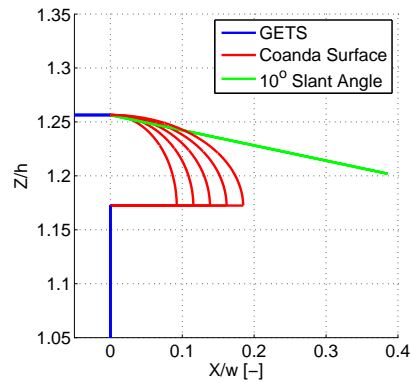


**Figure 6.22:** Different  $R_2/R_1$  ratios compared to a boat tail with 10 degrees slant angle

In figure E.12 in appendix E the resulting wake structure is visualized by means of velocity magnitude (E.12(a) and E.12(b)). It is interesting to observe that the vortex structure in the wake no longer consists of two horse shoe vortices, but a single ring vortex, similar as observed for the GETS model, see figure E.12(c) and E.12(d). The ring vortex is no longer split in two vortices and this appears to be caused by the absence of the vortices originating from the intersection of the Coanda surfaces. In the case of a high momentum coefficients these vortices are present (see figure E.11) but their presence is less pronounced in the case resulting from the optimization.

It must be noted that a higher compressor efficiency would improve the total drag reduction achieved by the system considerably. The dependency of the response surface on the compressor efficiency and the compressor inlet pressure indicate the sensitivity of the complete system to the total power consumption of the AFC system. If an unsteady pulsed jet sheet would be applied the total momentum would be reduced (almost halved) and thus reducing the total power consumption. In [2, 34] the effect of pulsed blown jet sheets has been researched leading to a similar drag reduction at lower energy costs.

## 6.7 Concluding remarks

In this chapter the results of the design process of the AFC system based on the results obtained by Englar [14] have been discussed. The drag reductions achieved by Englar are not reproduced, however the maximum momentum coefficient is limited and lower compared to Englar's for energy consumption reasons. From all simulations it is apparent that the energy consumption of the AFC system is dominant for high momentum coefficients, while the drag keeps decreasing for increasing momentum coefficients.

As the power consumption is included in the analysis the optimum configuration is a combination between a boat tail geometry utilizing the Coanda effect. The boat tail leads to inward curvature of the shear layers while the active flow control creates a fuller boundary layer profile which postpones separation and allows for a larger effective slant angle (see figure 6.22). In this situation there is no longer full jet turning present and the Coanda effect is not fully utilized. It must be noted that the separation of the flow from the Coanda surface will be an unsteady process in when changing yaw and vehicle speed is taken into account. A solution to this would be to reduce the geometry angle ( $\theta$ ) to ensure separation is forced to occur a fixed angle. This would reduce the unsteadiness of the flow field.

In order to gain more benefit from the Coanda effect the power consumption must be reduced, by increasing the compressor system efficiency or by reducing the mass flow. Increasing the compressor efficiency could be done by intelligent use of the trucks on board systems, although this would lead to added complexity and thus added cost.

The Coanda effect can also be applied using pulsed blowing instead of steady blowing to reduce the mean mass flow and the the total required power. Pulsed blowing is more efficient as it achieves higher (temporary) momentum coefficients which increase the jet turning effect. When the momentum coefficient is low the flow does not fully return to the steady situation which would occur at the low momentum coefficient. As the the system oscillates between the higher momentum flow field and the low momentum flow field the average drag reduction is higher than would be achieved with steady blowing with the mean momentum coefficient. In [34] the effect on the shear layers of pulsed blowing has been researched and a commercial application of a pulsed AFC system using the Coanda effect has been developed in 2008 resulting from the work in [2].

## Conclusions and Recommendations

In this chapter the thesis project is finalized by drawing the conclusions and making some recommendations. The application of a circulation control type active flow control system to the base of a generic truck model shows the drag can be reduced although the reductions claimed in literature [14] are not reproduced. The conclusions which can be made from the research are stated below.

### 7.1 Conclusions

**GETS model** In order to analyze the flow field around the GETS and AFC systems a hybrid grid is used and to a large extent the grid generation process is automated. The automation process reduces the setup time per simulation significantly and for a design driven approach this results in more design iterations in less time.

The time averaged RANS equations are solved on a half grid which leads to similar results as on a full grid and an acceptable level of grid independence is achieved. Full and half grid simulations show that the effect of using a symmetry plane in the center of the model to reduce computational costs results in a similar flow field and the resulting drag coefficient is within 4 drag counts or 0.1%.

Comparing the wind tunnel results to the CFD simulations the tangential and side force components follow the trend of the wind tunnel results, although (possibly) being offset due to the absence of wind tunnel corrections. The base pressure show a difference between the simulated and measured values which are expected to be related to the model and floor interaction, which is not captured accurately in the current CFD simulations. This interaction is expected to be less in the full scale simulations leading to the observation that the time averaged RANS simulations can be applied as a aerodynamic design tool for the active flow control system.

**AFC model** The active flow control system is added to the base of the GETS model and the initial design is based on experiments by Englar [14]. Full jet turning can be achieved at high momentum coefficients leading to a reduced wake length by a factor 7 and increasing the base pressure coefficient from  $-0.133$  to  $0.428$ , thereby reducing the drag coefficient from  $0.3177$  to  $0.2034$ . This drag reduction is uncorrected for the compressor power required to achieve the jet momentum, which leads to a net drag increase due to the high power consumption of high momentum and velocity jet sheets.

The power consumption requirements on the jet sheet lead to the restriction on the maximum momentum coefficient of  $C_\mu < 0.030$  and velocity ratios of  $1 < \zeta < 1.5$  to ensure a net drag reduction. Lower momentum coefficients lead to jet separation from the Coanda surface, altering

the flow field and reducing the increase in base pressure. A nett gain is still achieved due to the smaller wake and thereby increased base pressures.

Different flow structures occur for different Coanda surface radii and the  $R = 0.116w$  radius leads to the best compromise between the Coanda effect and the effect of curved base flaps [27]. Increasing the slot height reduces the energy consumption due to a reduced velocity ratio for equal momentum coefficient. However, the Coanda effect is also reduced leading to a smaller increase in base pressure and therefor slot heights larger than  $1.5 \cdot 10^{-3}w$  are not beneficial in reducing the total drag of the GETS model equipped with an AFC system.

Optimizing the Coanda geometry and the momentum coefficient leads to a final reduction of 20% at a compressor inlet pressure coefficient of 1.0 In case of a compressor inlet pressure coefficient of 0 the drag reduction is reduced to 14%, showing the impact of the power consumption of the AFC system on the resulting drag reduction. The optimization shows that the Coanda effect applied to a elliptic base flap is the most efficient shape, which is explained by the location of the separation point, as full jet turning is not achieved at the lower momentum coefficients.

Concluding the AFC system added to the GETS model researched in this thesis can lead to a large reduction in drag (15 to 20%) and this will lead to a reduction in fuel consumption of 5 to 10%, which results in a large reduction of operating costs and emissions.

## 7.2 Recommendations

The drag reductions achieved by the current system can be improved and the analysis methods should be validated. In order to continue the research in the investigated active flow control system the following general recommendations can be made:

- Wind tunnel tests or full scale tests should be performed in order to validate the numerical results, the full scale effects and the yaw performance of the AFC system.
- Pulsed blowing can be investigated in order to reduce the energy requirements of the AFC system. The overall efficiency can improve greatly by reducing the energy consumption of the compressor system.
- Different geometries could prove more beneficial, the Coanda angle could be varied and the jet slot can be placed at an angle relative to the base (instead of perpendicular to the base).
- From a practical point of view the addition of an internal pneumatic system to supply the AFC system with compressed air leads to increased complexity and costs and more research is required to be able to determine the final applicability of this system in a commercial environment.

As this thesis is focused on the application of CFD for a design purpose the following CFD related recommendations can be made:

- The effect of numerical diffusion on the flow field can be investigated for the full scale simulations. As the full scale Reynolds numbers are high, the flow solver is subjected to numerical diffusion.
- The wind tunnel simulations are subjected to merging boundary layers; the used wall functions are not suited to model this, therefor the near wall method should be applied in these simulations including a full hexahedral grid in this region.
- The use of more advanced turbulence models (Reynolds stress model, LES or DES) can be applied to simulate the (unsteady) flow field and for comparison with the  $k - \epsilon$  models. Although the residuals show small unsteady effects the unsteady flow field can be researched to gain more insight in the unsteady wake processes described in section 2.1.

---

# Bibliography

- [1] *SAE Wind tunnel test procedure for trucks and buses, recommended practice*. SAEJ1252. [4, 19]
- [2] O. Stalnov A. Seifert. Large trucks drag reduction using active flow control. [77, 78]
- [3] *Fluent Manual*. Ansys Inc, . [xv, 13, 15, 16, 18, 19, 21, 22, 29, 37, 51, 91, 93, 101, 102]
- [4] *ICEM CFD/AI\*Environment 10.0 User Manual*. Ansys Inc, . [24, 27, 93]
- [5] J. T. Heineck B. L. Storms, J. C. Ross. An experimental study of the ground transportation system (GTS) model in the NASA Ames 7- by 10-ft wind tunnel. (NASA/TM-2001-209621), 2001. [4, 54]
- [6] J. T. Heineck S. M. Walker B. L. Storms, D. R. Satran. A study of Reynolds number effects and drag-reduction concepts on a generic tractor-trailer. *34th AIAA Fluid Dynamics Conference and Exhibit*, (AIAA-2004-2251), 2004. [4]
- [7] P. W. Bearman. Some effects of freestream turbulence and the presence of the ground on the flow around bluff bodies. In *Aerodynamic Drag Mechanisms of Bluff Bodies and Road Vehicles*, . [19, 41]
- [8] P. W. Bearman. Bluff body flow research with application to road vehicles. In *The Aerodynamics of Heavy Vehicles II: Trucks, Buses, and Trains*, pages 3–13. . [19, 29]
- [9] M. H. Coanda. Propelling device, French patent 796843. [9]
- [10] K. R. Cooper. The effect of front-edge rounding and rear edge shaping on the aerodynamic drag of bluff vehicles in proximity. *SAE Paper 850288*, 1985. [4, 40]
- [11] A. R. Geore E. G. Duell. Measurements in the unsteady near wakes of ground vehicle bodies. *SAE Paper 930298*, 1993. [54]
- [12] R.C. McCallen ea. DOE's effort to reduce truck aerodynamic drag-jonit experiments and computations lead to smart design. *34th AIAA Fluid Dynamics Conference and Exhibit*, 2004. [7, 10, 58]
- [13] A. R. George E.G. Duell. Experimental study of a ground vehicle body unsteady near wake. *SAE 1999-01-0812*, 1999. [xiii, 6]
- [14] R. J. Englar. Development of pneumatic aerodynamic devices to improve the performance, economics, and safety of heavy vehicles. *SAE 2000-01-2208*, 2000. [2, 9, 12, 78, 79, 87]
- [15] R. J. Englar. Advanced aerodynamic devices to improve the performance, economics, handling and safety of heavy vehicles. [9, 11, 57, 58, 70]
- [16] R. J. Englar. Circulation control pneumatic aerodynamics: Blown force and moment augmentation and modification; past, present and future. *AIAA 2000-2541*, 2000. [9, 61]

- [17] B. G. Allan et al G. S. Jones, J. C. Lin. Overview of CFD validation experiments for circulation control applications at NASA. [32, 87]
- [18] D. Geropp. Pneumatic aerodynamic control and drag-reduction system for ground vehicles, 1999. US Patent 5,407,245. [10]
- [19] T Gustavsson. Alternative approaches to rear end drag reduction. Technical report, KTH Engineering Sciences, 2006. [8, 10]
- [20] T Gustavsson. Application of vortex generators to a blunt body. Technical report, KTH Engineering Sciences, 2006. [8]
- [21] D. Geropp H.-J. Oldenthal. Drag reduction of motor vehicles by active flow control using the Coanda effect. *Experiments In Fluids*, 28(3):74–85, 2000. [10, 12, 76]
- [22] B. Henneman. Modeling of front edge flow separation on rounded bluff bodies using commercial CFD software. Master’s thesis, Delft University of Technology, 2005. [4, 40]
- [23] S. Hoerner. *Fluid Dynamic Drag*. Hoerner Fluid Dynamics, 1965. [44]
- [24] <http://www.eia.doe.gov/>. US government energy information administration, November 2008. [xiii, 1]
- [25] W. H. Hucho. *Aerodynamik des Automobiles*. Vogel Verlag, 1981. [1]
- [26] et al I. B. Celik, U. Ghia. Procedure for estimation and reporting of uncertainty due to discretization in CFD applications. 130(078001-4), 2009. [94]
- [27] K. Salari J. M. Ortega. An experimental study of drag reduction devices for a trailer underbody and base. *AIAA 204489*, 2004. [59, 72, 80]
- [28] J.D. Anderson Jr. *Fundamentals of Aerodynamics*. McGraw-Hill, 3rd edition, 2001. [57, 85, 86]
- [29] D. Hyams B. Mitchell S. Sawyer L. Taylor K. Sreenivas, D. Nichols and D. Whitfield. Computational simulation of heavy trucks. *AIAA 2007-1087*, 2007. [40]
- [30] M. lanfrit. Best practice guidelines for handling automotive external aerodynamics with Fluent, february 2005. Fluent Deutschland GmbH. [21, 25, 29, 93]
- [31] K. Lauwers. Computational and experimental analysis of trailer shape modifications for drag reduction. Master’s thesis, Delft University of Technology, 2009. [19, 48, 49, 54, 55]
- [32] D. J. Maull. Mechanisms of two and three dimensional base drag. In *Aerodynamic Drag Mechanisms of Bluff Bodies and Road Vehicles*. [40]
- [33] E. J. Saltzman R. R. Meyer. A reassessment of heavy-duty truck aerodynamic design features and priorities. *NASA/TP-1999-206574*, 1999. [7]
- [34] L. Henning M.Pastoor. Feedback shear layer control for bluff body drag reduction. *Journal of Fluid Mechanics*, 608:161–196, 2008. [77, 78]
- [35] F. T. M. Nieuwstadt. *Turbulentie*. Epsilon uitgaven, 1998. [15, 16]
- [36] Department of Transport. Aerodynamics for efficient road freight operations. [xiii, 2]
- [37] ea P. A. Chang. Numerical simulation of two- and three dimensional circulation control problems. *AIAA 2005-80*, 2005. [32]
- [38] T. Marino M. P. Ebert P. A. Chang, J. Slomski. Numerical simulation of two-and three-dimensional circulation control problems. *43rd AIAA Aerospace Sciences Meeting and Exhibition*, 2005. [33, 87]

- [39] W. D. Pointer. Evaluation of commercial CFD code capabilities for prediction of heavy vehicle drag coefficients. *AIAA Fluid Dynamics Conference*, 2004. [40]
- [40] C. L. Rumsey R. C. Swanson. Numerical issues for circulation control calculations. *3rd AIAA Flow Control Conference*, 2005. [33]
- [41] B. A. Campbell R. J. Englar. Development of pneumatic channel wing powered-lift advanced STOL aircraft. *AIAA 2002-2929*, 2002. [1, 9, 61]
- [42] J. Ortega et. al. R. McCallen, K. Salari, editor. *Working Group Meeting on Heavy vehicle Aerodynamics Drag: Presentations and Summary of Comments and Conclusions*, 2003. [7]
- [43] H. Fernholz R Wille. Report on the first European colloquium, on the Coanda effect. *Fluid Mechanics*, pages 801–819, 1965. [9]
- [44] A. Roshko. Perspectives of bluff body aerodynamics. *Journal of Wind engineering and Industrial Aerodynamics*, 1993. [xiii, 7, 40]
- [45] J. Ross. Heavy vehicle drag reduction experimental evaluation and design, 2006. [xiii, 10]
- [46] B. Le Roux. Experimental aerodynamics: Separation control on trailers of trucks. Master's thesis, KTH Engineering Sciences, 2003. [10]
- [47] L. Davidson S. Krajnovic. Numerical study of the flow around a bus shaped body. *Journal of Fluids Engineering*, 125, 2003. [5, 6]
- [48] L. Davidson S. Krajnovic. Exploring the flow around a simplified bus with Large Eddy Simulation and topological tools. *The aerodynamics of heavy vehicles: Trucks Busses and Trains*, 2002. [26, 46]
- [49] L. Davidson S. Krajnovic. LES of the flow around a ground vehicle body. *SAE*, (2001-01-0702), 2001. [46, 47]
- [50] J. Janslon S. Perzon and L. Hoglin. On comparisons between CFD methods and wind tunnel tests on a bluff body. *SAE*, 1999. [24, 40, 44, 54]
- [51] L. P. Bernal ea S. R. Balkanyi. Dynamics of manipulated bluff body wakes. *Fluids*, 2000. [7]
- [52] C. Tongchitpakdee. Computational studies of the effects of active and passive circulation enhancement concepts on wind turbine performance. Master's thesis, Georgia Institute of Technology, 2007. [9, 32]
- [53] R. van Assen. Base drag reduction of articulated trucks by means of boat-tailing. Master's thesis, Delft University of Technology, 2007. [7, 77]
- [54] G. M. R. van Raemdonck. Design of an aerodynamic aid for a tractor trailer combination. Master's thesis, Delft University of Technology, 2006. [1, 3, 12, 19, 44, 52, 55]
- [55] G .M .R van Raemdonck. Time-averaged phenomenological investigation of a wake behind a bluff body. *BBAA VI International Colloquium on Bluff Bodies Aerodynamics and Applications*, 2008. [4, 18, 45, 48, 50, 55]
- [56] M. van Straaten. Computational and experimental investigation on base drag reduction of a generic transportation system by guiding vanes. Master's thesis, Delft University of Technology, 2007. [7, 8, 40, 44, 48, 49, 54, 55]
- [57] F. M. White. *Viscous Fluid Flow*. McGraw-Hill, Inc, second edition, 1991. [13, 20, 22, 27, 45, 50]
- [58] www.tcl.tk. Tool Command Language internet site, October 2007. [23]
- [59] T. Young. Outline of experiments and inquiries respecting sound and light. *Philosophical Transactions*, 1800. [9]



---

# Appendix A

---

## Momentum Coefficient Background

In this chapter some background is presented on the momentum coefficient, it is shown that the momentum coefficient is the non dimensional quantity of interest in blown aerodynamics and the energy consumption discussed in section 2.3.2 is elaborated on.

### A.1 Dimensional analysis

Using the Buckingham II theorem [28] the dimensionless physical quantities which are responsible for the variation of the parameters can be determined. For this analysis the flow is assumed to be incompressible and the viscosity and the density in the jet sheet is assumed to be equal to the freestream viscosity and density. The following quantities are expected to be responsible for the aerodynamic force acting on the active system:

- Freestream density
- Freestream velocity
- Geometric parameter, radius of the Coanda surface
- Fluid viscosity
- Yaw angle
- Jet sheet velocity
- jet sheet mass flow
- Coanda surface angle

The jet sheet velocity and the mass flow are related by the slot height, as the mass flow is defined as

$$\dot{m}_j = \rho_\infty V_j A_j = \rho_\infty V_j h L_j. \quad (\text{A.1})$$

Using above the aerodynamic force on the AFC model can be written as

$$R = f(\rho_\infty, V_\infty, R_1, \mu, \beta, V_j, \dot{m}_j, \theta) \quad (\text{A.2})$$

where the two angle parameters ( $\beta$ ,  $\theta$ ) are dimensionless and therefor can be used as dimensionless parameters. For clarity these are kept out of the further analysis and this leads to seven equations

and with the three fundamental dimensions (mass, length and time) according to the Buckingham  $\Pi$  Theorem this yields four dimensionless  $\Pi$  products:

$$\Pi_1 = f(\rho_\infty, V_\infty, R_1, R) \quad (\text{A.3})$$

$$\Pi_2 = f(\rho_\infty, V_\infty, R_1, V_j) \quad (\text{A.4})$$

$$\Pi_3 = f(\rho_\infty, V_\infty, R_1, \dot{m}_j) \quad (\text{A.5})$$

$$\Pi_4 = f(\rho_\infty, V_\infty, R_1, \mu). \quad (\text{A.6})$$

The  $\rho_\infty$ ,  $V_\infty$  and  $R_1$  variables are selected based on [28] to construct the  $\Pi$  products.

Using the fundamental dimensions the equations A.3 to A.6 can be manipulated into a set of equations which can be solved such that non dimensional quantities exist. The first  $\Pi$  product can be written as:

$$\Pi_1 = \rho_\infty^a V_\infty^b R_1^c R \quad (\text{A.7})$$

and writing the latter in dimensional terms results in

$$[\Pi_1] = (ml^{-3})^a (lt^{-1})^b (l)^c (mlt^{-2}). \quad (\text{A.8})$$

As the  $\Pi$  product is dimensionless, the right hand side of equation A.8 also needs to be dimensionless, which requires the exponents of the fundamental dimensions to be zero, leading to the following linear set of equations:

$$\begin{aligned} \text{m: } 0 &= a + 1 \\ \text{l: } 0 &= -3a + b + c + 1 \\ \text{t: } 0 &= -b - 2. \end{aligned}$$

Solving this leads to  $a = -1$ ,  $b = -2$  and  $c = -2$  and substituting in the  $\Pi$  product leads to the non dimensional quantity:

$$\Pi_1 = \frac{R}{\rho_\infty V_\infty^2 R_1^2}. \quad (\text{A.9})$$

A similar procedure can be applied for the other  $\Pi$  products yielding the following results:

$$\Pi_2 = \frac{V_j}{V_\infty} \quad (\text{A.10})$$

$$\Pi_3 = \frac{\dot{m}_j}{\rho_\infty V_\infty R_1^2} \quad (\text{A.11})$$

$$\Pi_4 = \frac{\rho_\infty V_\infty R_1}{\mu}. \quad (\text{A.12})$$

Note that all  $\Pi$  products can be multiplied by an arbitrary constant as constants are dimensionless. Summarizing the following four non dimensional quantities are found by applying this method and they can be described as follows:

- $\Pi_1$  states that the force on the body can be expressed as a coefficient using the dynamic pressure and a reference area
- $\Pi_2$  defines the velocity ratio ( $\zeta$ ) as a non dimensional parameter

- $\Pi_3$  relates the mass flow in the jet sheet to the a reference mass flow
- $\Pi_4$  defines the Reynolds number based on the freestream conditions and a reference length

The Buckingham  $\Pi$  Theorem states that a product of two non dimensional quantities remains a non dimensional quantity. In literature [14, 17, 38] the momentum coefficient is commonly defined as the product of  $\Pi_2$  and  $\Pi_3$  or:

$$C_\mu = \frac{V_j}{V_\infty} \frac{\dot{m}_j}{\rho_\infty V_\infty R_1^2} = \frac{\dot{m}_j V_j}{\rho_\infty V_\infty^2 R_1^2} = 2 \frac{\dot{m}_j V_j}{q_\infty R_1^2} \quad (\text{A.13})$$

The defined length  $R_1$  can be replaced by any reference length, in this research the width and the frontal area of the GETS model will be used, as is commonly applied in truck aerodynamics.

Concluding it can be stated that the force on the AFC model will be dependent on the Reynolds number and the momentum coefficient and the geometric angles (yaw angle and the Coanda surface angle). The resulting force on the body can be defined as a coefficient related to the dynamic pressure and a reference area, as is common in aerodynamics.

## A.2 Energy equation

As discussed in section 2.3.2 the influence of the compressor used for the Coanda jet requires energy and thus influences the total efficiency of the system. The total power required by the truck can be written as:

$$P_{total} = P_{friction} + P_{mechanical} + P_{aero} \quad (\text{A.14})$$

As in this research the main focus is on the aerodynamic drag, or more specifically the aerodynamic power required to overcome drag. Therefor we focus on  $P_{aero}$ :

$$P_{aero} = P_{aero, clean} + P_c \quad (\text{A.15})$$

Where  $P_c$  is the power required by the compressor used to pressurize the air which is accelerated out of the velocity inlet and  $P_{aero, clean}$  is the aerodynamic power without the compressor. The total power is related to the velocity as

$$D_{total} V_\infty = P_{aero, clean} + P_c \quad (\text{A.16})$$

and the compressor power can be formulated as:

$$P_c = \frac{1}{\eta_c} \Delta p_c V_j A_j \quad (\text{A.17})$$

With  $\Delta p_c$  the pressure increase over the compressor. Using the pressure coefficient (A.18) and bernoulli's equation:

$$C_{p,j} = \frac{p_j - p_\infty}{\frac{1}{2} \rho V_\infty^2} \quad (\text{A.18})$$

$$\frac{1}{2} \rho V_j^2 + p_j = \frac{1}{2} \rho V_i^2 + p_i + \Delta p_c \quad (\text{A.19})$$

Assuming the inlet velocity to be zero and rewriting (with  $\zeta = \frac{V_j}{V_\infty}$ ):

$$\Delta p_c = \frac{1}{2} \rho V_\infty^2 (\zeta^2 + C_{p,j} - C_{p,i}) \quad (\text{A.20})$$

Inserting in A.17

$$P_c = \frac{1}{\eta_c} \frac{1}{2} \rho V_\infty^3 \zeta A_j (\zeta^2 + C_{p,j} - C_{p,i}) \quad (\text{A.21})$$

Inserting in A.15 and using  $D_{total} = \frac{1}{2}\rho V_{\infty}^2 C_D A_{ref}$ :

$$\frac{1}{2}\rho V_{\infty}^3 C_D A_{ref} = P_{aero, clean} + \frac{1}{\eta_c} \frac{1}{2}\rho V_{\infty}^3 \zeta A_j (\zeta^2 + C_{p,j} - C_{p,i}) \quad (A.22)$$

With  $P_{aero, clean}$  as

$$P_{aero, clean} = \frac{1}{2}\rho V_{\infty}^3 C_{D^*} A_{ref} \quad (A.23)$$

The above equations combine to

$$C_D = C_{D^*} + \frac{1}{\eta_c} \frac{A_j}{A_{ref}} \zeta (\zeta^2 + C_{p,j} - C_{p,i}) \quad (A.24)$$

With  $C_{D^*}$  the drag coefficient neglecting the AFC power consumption,  $C_{p,i}$  the pressure coefficient at the compressor inlet (1 for stagnation pressure). Without AFC blowing the velocity ratio ( $\zeta$ ) equals zero and thus  $C_D = C_{D^*}$ .

---

# Appendix B

---

## Grid Parameters

	GETS	AFC
Geometric	length, width, height, front radius, ground clearance	Coanda radius ( $R_1$ ), radius ratio, slot height, Coanda angle ( $\theta$ )
Topologic	BL thickness, wake length wake thickness	BL jet sheet exp. ratio, jet exp. pt. $a&b$ wake length, wake thickness
	<i>Number of Nodes, Minimum &amp; Maximum Size, Growth Rate</i>	
Sizing	BL thickness, GETS longitudinal GETS lateral, front curved surface interface & outer domain	BL jet thickness, BL GETS thickness Coanda surface, base inside & top interface & outer domain
Quality	minimum quality requirement, amount of smoothing iterations	

**Table B.1:** Model Parameters GETS and AFC model

		GETS			AFC			
Geometric	length	16.5	width	2.595	radius 1	0.1 – 0.45	radius ratio	0.8 – 1.6
	height	3.51	front radius	0.54	slot height	0.002 – 0.006	Coanda angle	90
	ground clearance	0.495						
Topologic	BL thickness	0.02			BL jet sheet expansion ratio	5	expansion ratio $a$	1.5
	wake thickness	0.35			expansion ratio $b$	1.75	wake length	3.5 $w$
	wake length	4 $w$			wake thickness	0.35		
<i>Number of Nodes</i>								
	BL thickness	24	GETS longitudinal	252	BL jet thickness	20	BL GETS thickness	40
	GETS lateral	42	front curved surface	42	Coanda surface	50	base inside & top	100
	<i>Minimum Size</i>							
Sizing	BL thickness	0.0014	GETS longitudinal	0.005	BL jet thickness	0.00005	BL GETS thickness	0.00005
	GETS lateral	0.005	front curved surface	0.005	Coanda surface	0.05	base inside & top	0.05
	interface domain	0.0975	outer domain	—*	interface domain	0.090	outer domain	—*
<i>Maximum Size</i>								
	BL thickness	0.0075	GETS longitudinal	—*	BL jet thickness	0.001	BL GETS thickness	0.001
	GETS lateral	0.030	front curved surface	0.050	Coanda surface	—*	base inside & top	0.05
	interface domain	—*	outer domain	2	interface domain	—*	outer domain	2
<i>Growth Rate</i>								
	BL thickness	—*	GETS longitudinal	1.2	BL jet thickness	—*	BL GETS thickness	—*
	GETS lateral	1.2	front curved surface	1.2	Coanda surface	1.2	base inside & top	1.2
	interface domain	1.1	outer domain	1.2	interface domain	1.1	outer domain	1.2
Quality	minimum quality			0.5	amount of iterations			75

\* Computed from related parameters

**Table B.2:** Model Parameters GETS and AFC model (dimensions in [m])

## Element Properties and Richardson Extrapolation

### C.1 Grid topologies

The use of the finite volume method requires the computational domain to be split in discrete control volumes, where in each volume the mathematical equations are numerically solved. Different types of grid topologies exist, each with their advantages and disadvantages. In this study four types of elements have been used;

- Tetrahedron
- Hexahedron
- Prism/Wedge
- Pyramid

In figure C.1 the four different types are shown. The choice between a structured (Hexahedron element) mesh or an unstructured mesh is mainly a compromise between the amount of cells, and the quality of the solution and the time to generate the grid. The most common used element is the tetrahedron due to its ease of application in most grid generators. For boundary layer grids the structured hexahedron is more appropriate, for reasons stated below. The prism and pyramid elements are mainly used to couple two grids, creating a hybrid grid. The following properties hold for the different element types.

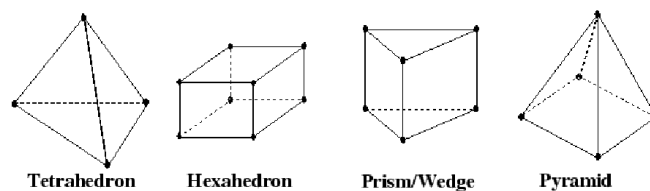
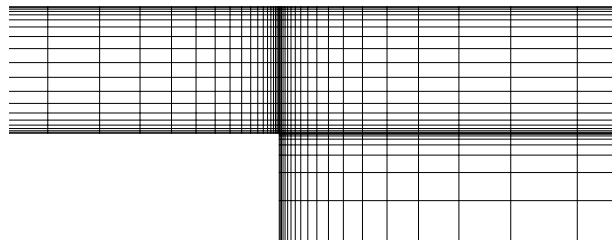


Figure C.1: Grid topologies [3]

- Tetrahedron

- Ease of use; tetrahedrals can be used to fill large domains with greater ease compared to structured elements and with less elements in general.
  - Tetrahedrals are more sensitive for numerical diffusion. Numerical diffusion adds artificial diffusion to the system, influencing the solution, which is especially important in high Reynolds number flows, such as the flow over a truck. Numerical diffusion is an effect of the discretization scheme and the resulting truncation errors and is strongly influenced by the grid topology (see section 3.5). In areas with strong gradients (such as in the boundary layer) the truncation errors can be reduced by aligning the elements with the flow. This is not possible with unstructured elements as the element is based on a triangle. This makes the tetrahedrals less suitable for use in the boundary layer.
  - Tetrahedrals can be used for more complex geometries as every surface can be covered in triangles. Also clustering of cells in areas with high gradients (wakes) is easier compared to structured elements. Generally the use of unstructured cells leads to less cells used compared to a grid built with only structured elements.
- Hexahedron
    - Hexahedral elements can be aligned with the flow in near wall applications, leading to less numerical diffusion in the boundary layer, this makes hexahedral elements the most suitable element for application in the boundary layer.
    - As the element has four edges per face, it can only be qualitatively mapped onto surfaces consisting of four edges. This makes this element less suitable for complex geometries.
    - Hexahedrals are less suited for refinements as the structured grid forces refinements in areas where refinement is often not required. An example is shown in figure C.2 where refinements are made near the corner of a backward facing step, leading to the same refinement at the end of the channel en above the corner.



**Figure C.2:** Example of unwanted grid refinement

- Prism/Wedge
  - Prism or wedge elements are formed by extruding a triangle surface element perpendicular to the surface. They are used to create a boundary layer grid on complex geometries. Since the elements are extruded normal to the surface their thickness can be controlled accurately which is critical in boundary layer modeling.
  - Prims or wedge layers can be easily connected to tetrahedral elements, allowing for grids with a boundary layer formed by prisms/wedges and the domain filled by tetrahedrals.
- Pyramid
  - Pyramids are elements used to connect hexahedrals to tetrahedrals. The quadrilateral base of the pyramid connects to the quadrilateral face of the hexahedron and the triangular faces connect to hexahedral elements. A typical application is to connect a hexahedral boundary layer grid and a tetrahedral domain grid.

- Since the pyramid consists of four edges and five faces it is difficult to achieve a high grid quality with pyramid elements. More on grid quality can be found in C.2.

## C.2 Grid quality criteria

The quality of the computational grid is of significant influence on the final results and the convergence of the CFD computations. Grid requirements can be divided in cell size requirements and cell quality requirements. The CFD predictions will be dependent on the amount of cells used in the grid, making the solution dependent on the amount of cells. As a result of this a compromise has to be found between the amount of cells used for the computations and the accuracy of the results.

**Skewness** The most important quality measure is the element skewness, an indication of the shape quality of the element. The angle skewness, which is valid for all elements, is defined as:

$$\max\left(\frac{\alpha_{max} - \alpha_e}{180 - \alpha_e}, \frac{\alpha_e - \alpha_{min}}{\alpha_e}\right), \quad (\text{C.1})$$

with:

$\alpha_{max}$  the maximum angle in the element (in degrees),

$\alpha_{min}$  the minimum angle in the element (in degrees),

$\alpha_e$  the equilateral angle for the given element (60 degrees for unstructured and 90 degrees for structured grids).

The volume skewness, mainly used for tetrahedral elements is defined as a ratio of the volume of the element to the optimal volume or:

$$\frac{V_{optimal} - V_{element}}{V_{optimal}}. \quad (\text{C.2})$$

The optimal element volume is the volume of an equilateral element with same circumradius as the evaluated element.

In figure C.3(a) a highly skewed compared to a element with low skewness is shown. From [30] the skewness of the surface mesh should not exceed 0.45, while [4] prescribes the skewness for the volume mesh should stay below 0.8 - 0.9 for the flow solver to be able to converge.

**Smoothness** The element smoothness describes the rapidness of the volume change between neighboring cells. A rapid change in cell volume can lead to larger truncation errors and should be prevented. [3] The growth ratio of cells should therefor be limited, which leads eventually to more cells in the domain. In figure C.3(b) an example is given of elements with a high growth ratio. Fluent prescribes a maximum growth ratio of 20% for both surface and volume elements.

**Aspect ratio** The aspect ratio is defined as the ratio of the longest over the shortest edge length, making this ratio a measure for the stretching of the element. Highly stretched cells can lead to an element reduction in anisotropic flows [3] but this should be avoided in isotropic flows. Fluent recommends a maximum aspect ratio of 5:1, for isotropic flows. This value can be exceeded in areas where the flow is aligned with the cells, for example in the boundary layer.

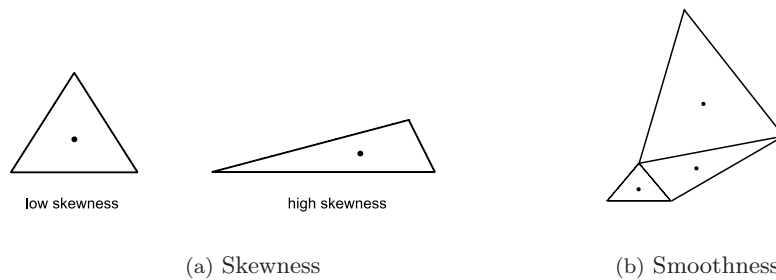


Figure C.3: Different element properties

### C.3 Richardson extrapolation

Richardson extrapolation is a widely applied method to estimate the discretization error in CFD computations [26]. The method uses computational results on different grids to extrapolate the exact grid converged solution (full grid convergence is in practical sense nearly impossible) and can thus indicate the error introduced by the discretization process.

The extrapolation is applied using three different grid sizes, a coarse, medium and fine grid where a global grid size  $h$  is defined as

$$h = \left[ \frac{1}{N} \sum_{i=1}^N V_i \right]^{\frac{1}{3}} \quad (\text{C.3})$$

where  $V_i$  is the volume of the  $i^{\text{th}}$  element and  $N$  the amount of cells in the grid. The three grids used all vary in grid size according to  $h_1 < h_2 < h_3$  and defining the exact solution as follows:

$$\phi_{exact} - \phi_1 = Kh_1^p \quad (\text{C.4})$$

with  $\phi_{1,2,3}$  the numerical solution for grids 1, 2 and 3 respectively.  $K$  is an unknown constant and  $p$  the apparent order of the method.

Defining the following parameters based on the grid sizes and the numerical solutions,

$$\epsilon_{21} = \phi_2 - \phi_1, \quad \epsilon_{32} = \phi_3 - \phi_2, \quad (\text{C.5})$$

$$r_{21} = \frac{h_2}{h_1}, \quad r_{32} = \frac{h_3}{h_2}, \quad (\text{C.6})$$

the apparent method order can be solved for using the following equations:

$$p = \frac{1}{\ln(r_{21})} \left| \ln \left| \frac{\epsilon_{32}}{\epsilon_{12}} \right| + q(p) \right|, \quad (\text{C.7})$$

$$q(p) = \ln \left( \frac{r_{21}^p - s}{r_{32}^p - s} \right), \quad (\text{C.8})$$

$$s = 1 \cdot \text{sgn} \left( \frac{\epsilon_{32}}{\epsilon_{21}} \right). \quad (\text{C.9})$$

Using the apparent order and the results from the used grids 1 and 2 the exact solution can be estimated using

$$\phi_{exact}^{21} = \frac{r_{21}^p \phi_1 - \phi_2}{r_{21}^p - 1}. \quad (\text{C.10})$$

It must be noted that these measures indicate the error in the solution originating from the discretization process it does not account for modeling errors.

### C.3.1 Extrapolation results

Applying the Richardson extrapolation on the computed GETS and AFC grids can give an impression of the discretization error present in the used grids. In table C.1 the summarized results for the extrapolation applied for the GETS and the AFC grids are shown.

	GETS	AFC
$h_1$	0.2005	0.1518
$h_2$	0.2284	0.1666
$h_3$	0.2660	0.1904
$C_D(h_1)$	0.3140	0.1015
$C_D(h_2)$	0.3180	0.1023
$C_D(h_3)$	0.3254	0.1031
$p$	3.2	5.0
$C_{D,exact}$	0.3063	0.1009

**Table C.1:** Richardson extrapolation data

From the table it can be seen that the GETS grids shows convergence for the drag coefficient, but the extrapolated exact value is nearly 2.5% lower compared to the simulation on the finest grid. The AFC grid extrapolated solution differs 0.60% from the computation on the finest grid.

The used grids for both models are approximately  $6M$  grid cells, in order to obtain a grid which leads to a discretization error where the  $C_D(h)$  value is within one percent of  $C_{D,exact}$  a grid consisting of approximately  $20M$  cells, which leads to practical problems for an engineering research.



---

## Appendix D

---

# Additional Computational Results of the GETS System

The locations of the velocity profiles in the wake are shown in figure D.1 where the wake stations are shown in the symmetry plane of the model ( $y = 0$ ).

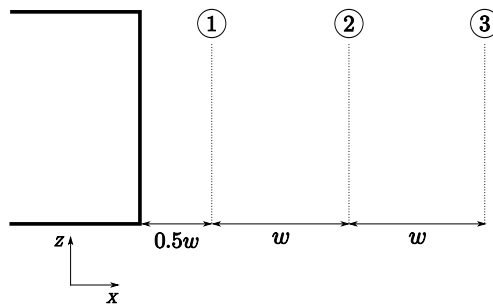


**Figure D.1:** Wake Station aft of the base, in the  $y = 0$  plane

In figure D.2 the base pressure is shown, where the different locations of the base pressure maximum can be seen. The location of the maximum (and minimum) pressure changes due to the presence of the vortex core.

In figure D.3 the effect of the vortex core shows the change of base pressure maximum. Note the effect of the symmetric simulation as the wiggle in pressure coefficient is not present in the full 3D dimensional simulations.

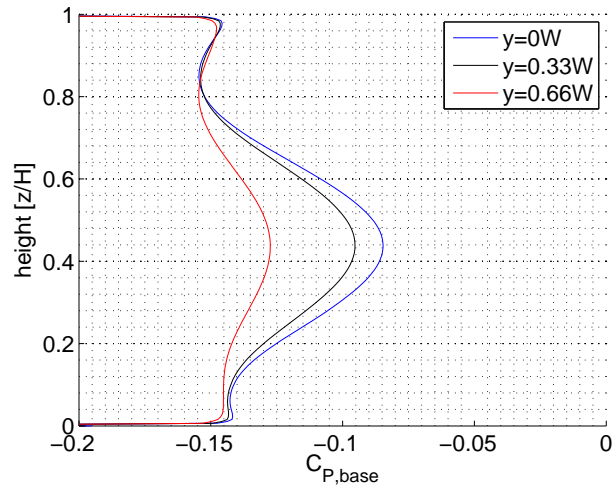


Figure D.2: Base Pressure in XZ-plane

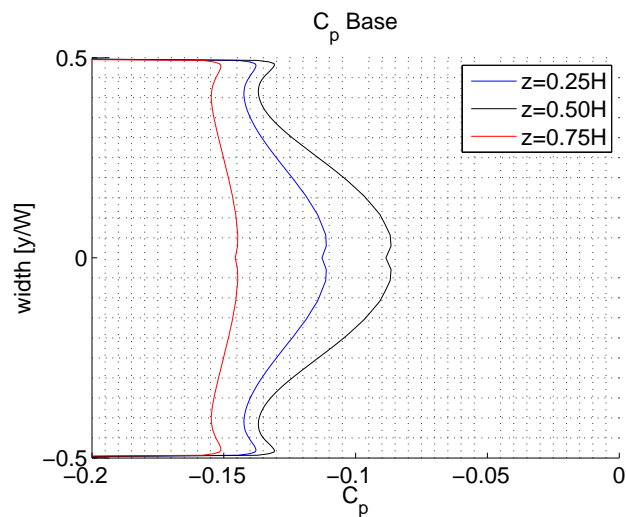
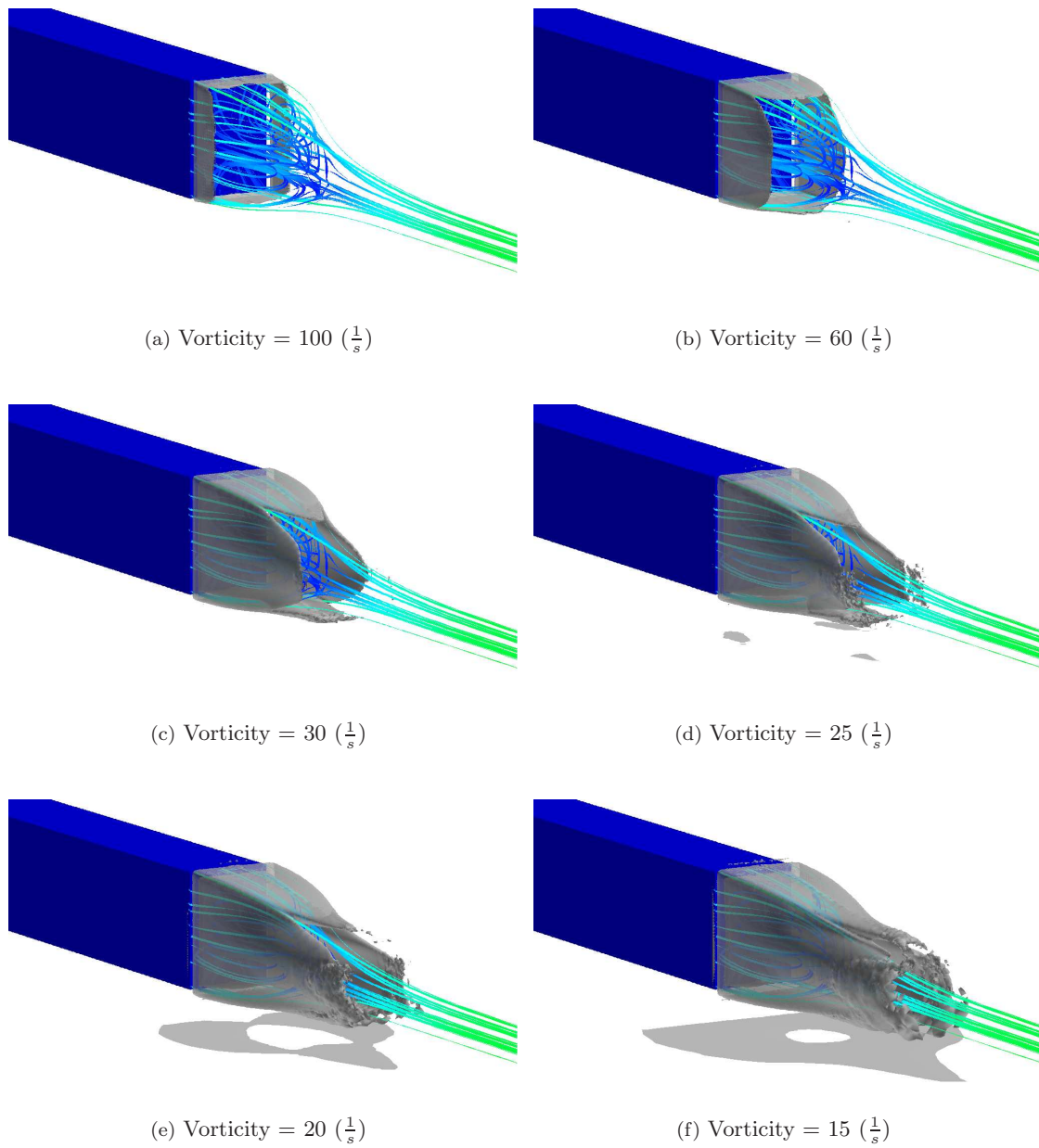


Figure D.3: Base Pressure in XY-plane



**Figure D.4:** Steady vorticity iso-surfaces (streamlines colored by velocity magnitude)



---

# Appendix E

---

## Additional Computational Results of the AFC System

### E.1 Grid independence and quality metrics

As the grid for the Coanda system differs in several ways from the GETS model a grid study is required in order to ensure the quality of the Coanda grid. Several different aspects are discussed, similar as for the GETS grid.

#### E.1.1 Wall function validity

The near wall modeling approach as described in section 3.3 requires the  $y^+$  values to be below five and preferably in the order of unity [3] in order for the near wall approach to be valid. In figure E.1 a contour plot of the  $y^+$  values on the surface of the AFC model is shown with the scaling modified in order to identify possible area's where the  $y^+$  value exceeds the maximum allowable value of five.

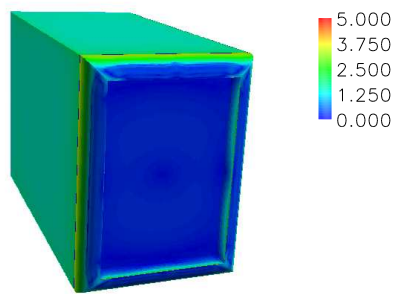


**Figure E.1:**  $y^+$  values on rear section of Coanda system model

As can be seen in the figure the limit of 5 is never exceeded for the parameters used in this simulation ( $C_\mu = 0.021, \zeta = 1.4$ ). It must be noted that for values of  $\zeta$  the friction coefficient on the Coanda surfaces increases, increasing the  $y^+$  value close to the limit of five, however it is never exceeded in this study.

### E.1.2 Grid independence

The grid constructed for the Coanda system uses the near wall modeling approach leading to much denser grid near the boundary layer and more strict cell growth requirements on the interface between the structured and unstructured grid. Although the wake is reduced in size the density of cells in the wake is increased in order to capture the interaction between the jet sheet and the shear layer. The geometry consisting of the  $R_1 = 0.116w$  and a slot height of  $1.5 \cdot 10^{-3}w$  is simulated at a momentum coefficient of 0.021 for various grid densities to validate the grid for convergence. The grid density is varied mainly in boundary layer cell spacing and cell size in the wake. In the outer domain the gradients are small and thus grid refinement is less beneficial in this area.

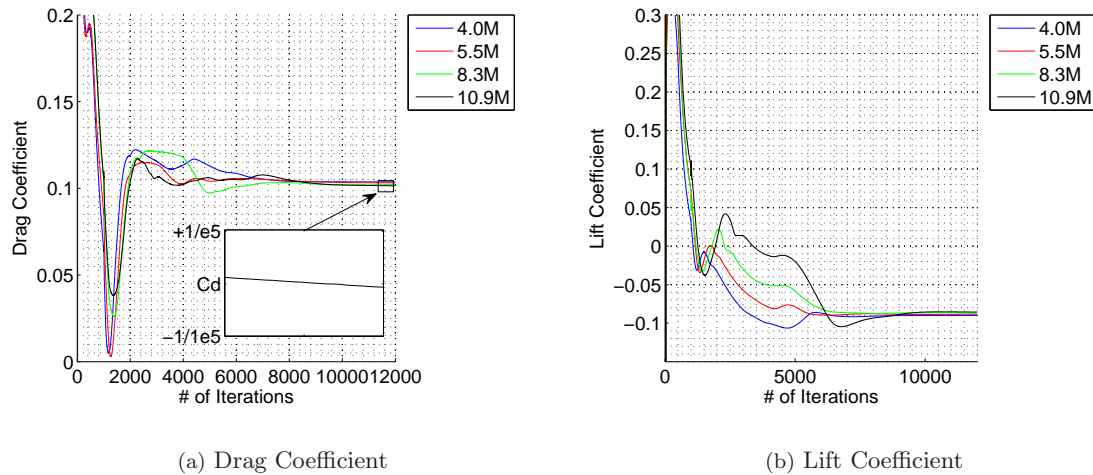


Figure E.2: Convergence of drag and lift coefficient

In figure E.2 the drag and lift coefficient is shown for the amount of iterations performed for the convergence study. Both the lift and drag coefficients converge after approximately 10,000 iterations. A smaller grid with 3.2M cells has also been simulated, however in this simulation turbulent viscosity errors occurred in the wake of the model, indicating an insufficient cell density [3].

In the detail view in figure E.2(a) the drag coefficient does not oscillate as in the GETS simulations but slowly decreases. This implies that the solution is not fully converged regarding the drag coefficient and that there is no unsteady behavior in this AFC simulation. The unsteady flow behavior that was visible in the drag coefficient and the residuals of the GETS simulations (see section 5.2) is not present in the AFC simulations, indicating that the use of time-averaged simulations is valid for the AFC model.

In figure E.3 the residuals for a 5.5M cells grid are shown in an overview and a more detailed view. It can be seen how the residuals decrease slower compared to the GETS simulations (see figure 5.3), thus requiring more iterations for the AFC simulations.

The final converged drag and lift coefficient obtained by the converge study grids are shown in E.4. In both graphs it is visible that both coefficients are not completely converged and also the rate of convergence does not appear to change with the maximum amount of cells (10.9M). Compared to the GETS simulations the lift coefficient is more sensitive to grid changes, as the lift coefficient increases with increasing cell count.

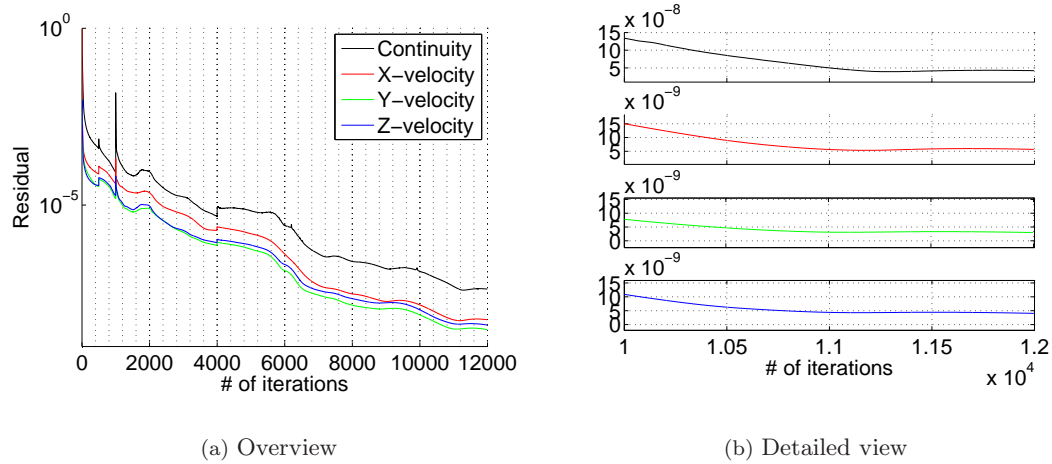


**Figure E.3:** Residuals AFC simulation, 5.5M cells

Using Richardson extrapolation (see appendix C and table C.1) the extrapolated drag coefficient for the AFC model in this configuration is 0.1009, a difference of 2% with the simulation using the 5.5M cells, which is considered acceptable for a discretization error.

A similar conclusion can be found when the velocity profiles are examined from figure E.5. It can be seen that the velocity profile is not completely converged for the 5.5M cells grid when compared to the 10.9M cells grid. Simulations using a 10M or more cells grids are considered to be unpractical for an engineering application and considering the expected accuracy of the CFD simulations the solution is assumed to have been converged for the used grid and grid topology consisting of approximately 5 to 6 million cells.

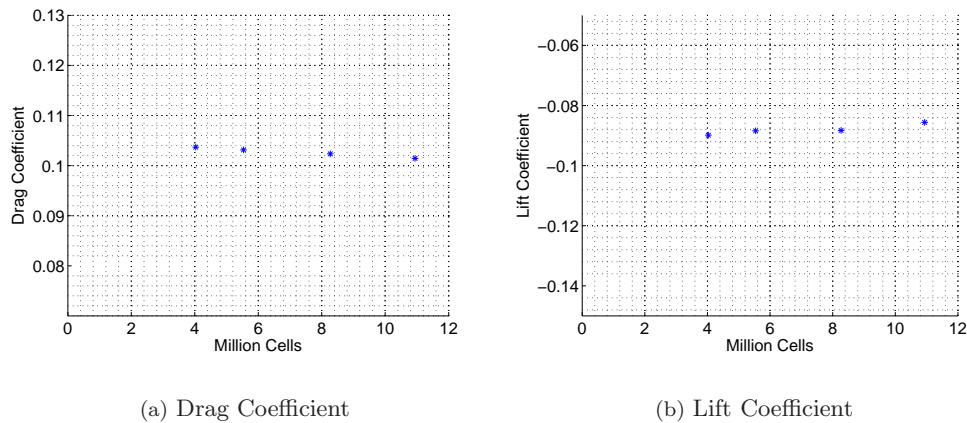


**Figure E.4:** Drag and Lift convergence for different grid sizes

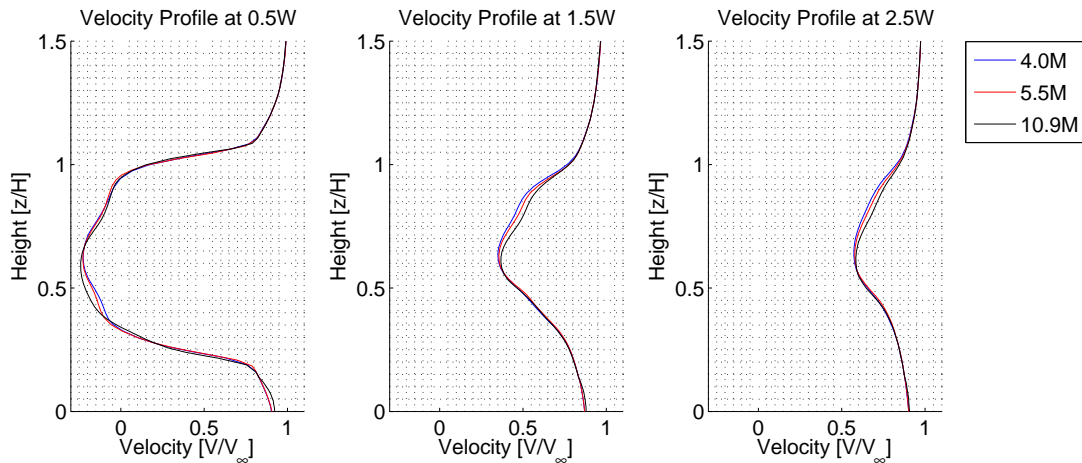


Figure E.5: Velocity profiles in the symmetry plane at different stations behind the AFC model

### E.1.3 Grid cut location

The grid for the AFC system consists of the last  $2w$  of the GETS model and uses a velocity inlet with boundary layer profile obtained in the simulations of the GETS model. In figure E.6 the pressure coefficient is shown in the symmetry plane of the GETS model with a modified scaling showing the location of the grid cut at  $x = 4.4w$ . It can be seen that the pressure coefficient does not change significantly in longitudinal directing, implying that the influence of the wake upstream of the model is minimal at this position.

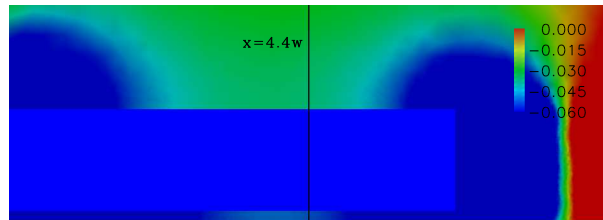
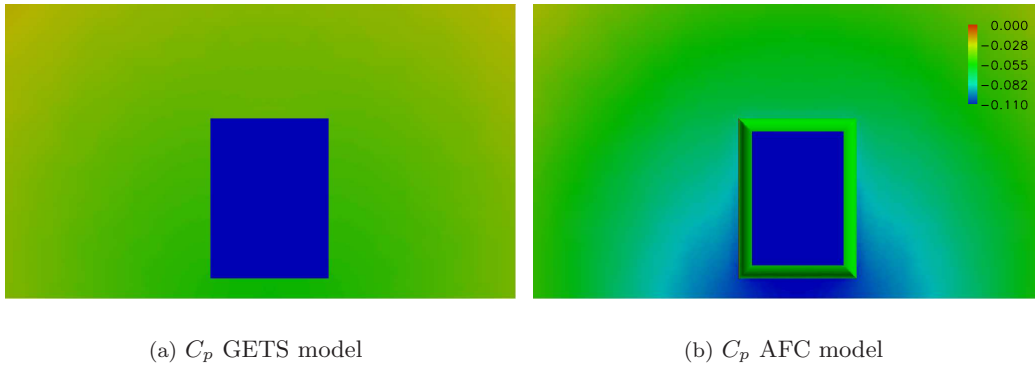


Figure E.6: Pressure coefficient in symmetry plane of GETS model (modified scale)

In figure E.7 the pressure coefficient in the plane at  $x = 4.4w$  is shown for the GETS model and the AFC model. From this figure it can be seen that the wake influences the pressure upstream of the base more in case of the AFC system compared to the GETS model. The assumption that the grid cut at  $x = 4.4w$  is sufficiently upstream of the base for the AFC simulations is therefore not valid and as can be seen mainly the flow underneath the model is significantly influenced by the AFC system, allowing more flow underneath the model and thus reducing the pressure under the model. The pressures induced by the wake influence the complete flow field further upstream than the  $2w$  used in this research and thus will influence the results of the simulations.



**Figure E.7:** Pressure coefficient at  $x=4.4w$  for both GETS and AFC model

### E.1.4 Grid dimensions

Due to the use of the near wall modeling approach the amount of cells required exceed the five million for a model consisting just of the last two widths of length of the GETS model. In order to save cells and thus computation time the grid can (similar to the GETS grid) be split in a symmetric half model. In table E.1.4 the base pressures and the locations of the vortex cores for a half and full AFC model are tabulated.

	$C_\mu$	$C_{D^*}$	$C_D$	$C_{p,base}$	$C_p$	$X_{V1}$	$Z_{V1}$	$X_{V2}$	$Z_{V2}$	$X_{SP}$	$Z_{SP}$
Half model	0.021	0.250	0.264	0.053	-0.213	0.24	0.80	0.39	0.18	0.92	0.49
Full model	0.021	0.247	0.262	0.054	-0.212	0.23	0.82	0.36	0.18	0.92	0.50

**Table E.1:** Data for  $R_1 = 0.116$ ,  $h = 1.5e - 003$ , coordinates expressed in  $X/W$  and  $Z/H$

From the table a small difference of the drag coefficients can be seen, also observed by the GETS simulations in section 5.3. This discrepancy is related to the small difference in base pressure, both base pressures are compared in a contour plot in figure E.8, which shows good agreement between the full and half domain simulations. The locations of the vortex cores and the saddle point are in good agreement with each other, indicating the wake structure is predicted by both simulations in a identical manner.

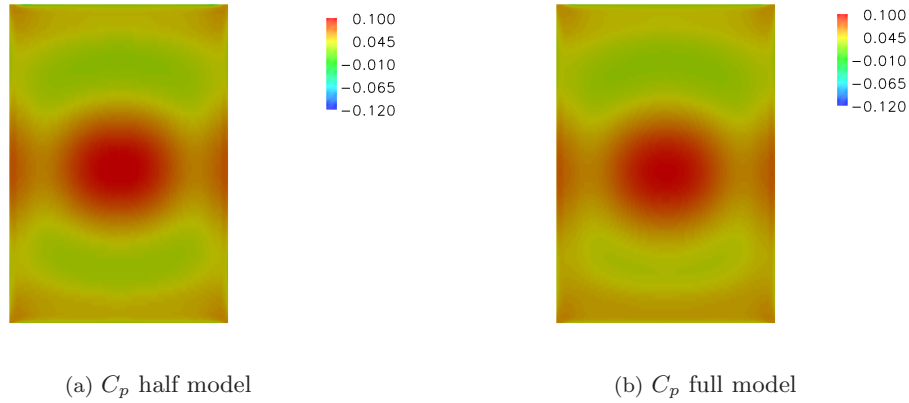


**Figure E.8:** Base pressure coefficient half and full model, ( $R_1 = 0.116w$ ,  $h = 1.5 \cdot 10^{-3}w$ ,  $C_\mu = 0.021$ )

## E.2 AFC system results

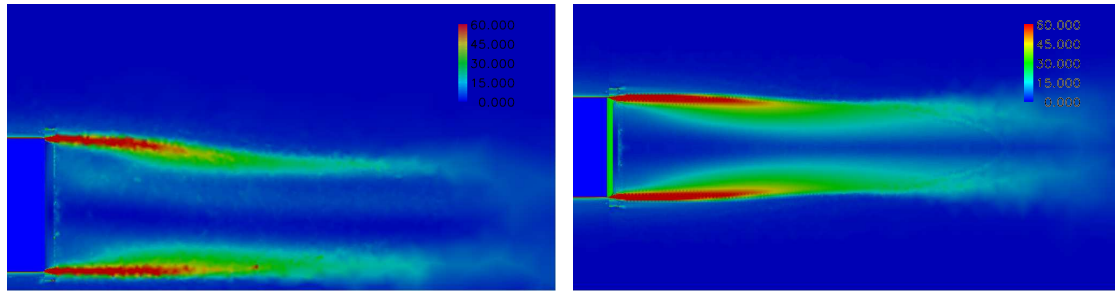
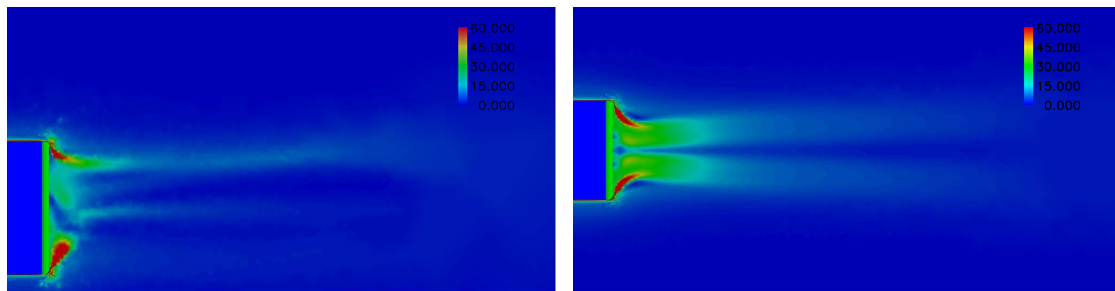
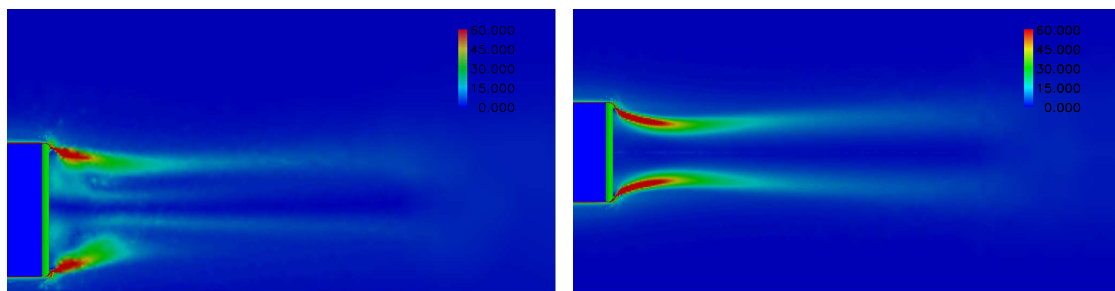
### E.2.1 Englar's reference case

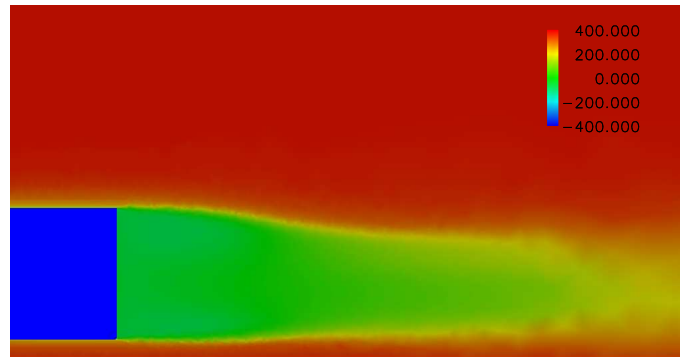
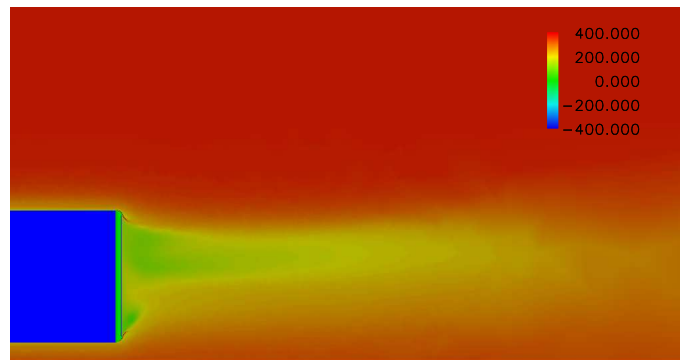
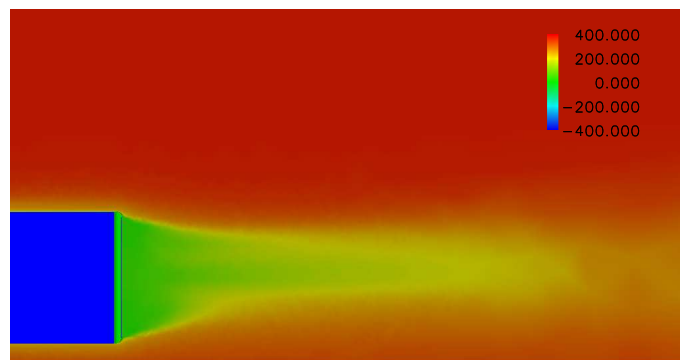
In table E.2 all the results for the reference case simulations are tabulated. Not all geometries are simulated for maximum momentum coefficient, as it practically unwanted to apply very high velocity ratios due to the related power consumption.

$C_\mu$	$\zeta$	$R_1(R/W)$	$h(h/W)$	$C_{D^*}$	$C_D$	$\Delta C_D(\%)$
0.000	0.0	0.116	$1.5e-003$	0.2963	0.2963	-6.8
0.021	1.4	0.116	$1.5e-003$	0.2495	0.2637	-17.1
0.035	1.8	0.116	$1.5e-003$	0.2319	0.2745	-13.7
0.053	2.2	0.116	$1.5e-003$	0.2216	0.3109	-2.2
0.073	2.6	0.116	$1.5e-003$	0.2035	0.3618	13.8
0.015	1.2	0.058	$1.5e-003$	0.2647	0.2703	-15.0
0.034	1.8	0.058	$1.5e-003$	0.2440	0.2866	-9.9
0.061	2.4	0.058	$1.5e-003$	0.2304	0.3512	10.4
0.095	3.0	0.058	$1.5e-003$	0.2195	0.4732	48.8
0.137	3.6	0.058	$1.5e-003$	0.2077	0.6627	108.4

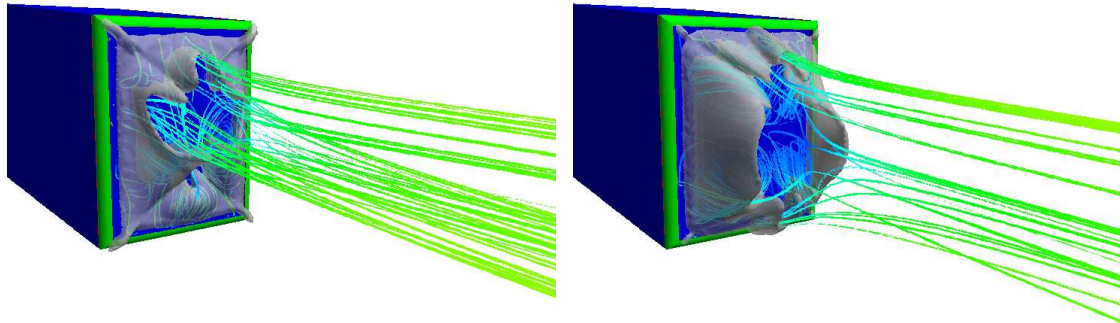
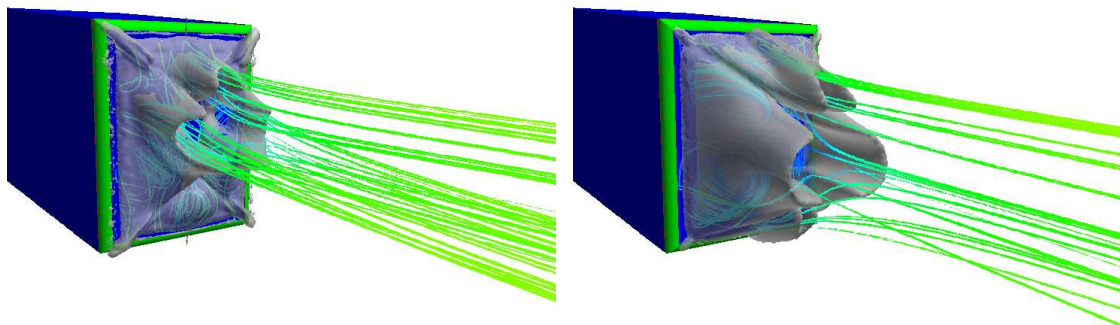
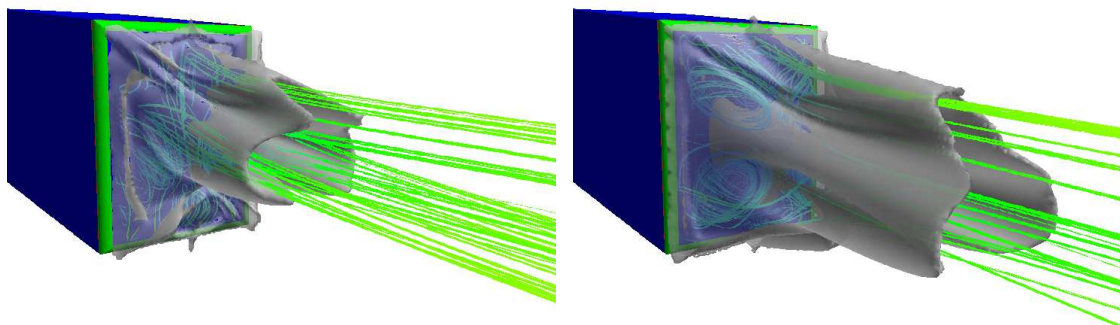
**Table E.2:** Results Reference Case

The inward curvature of the shear layers for the full jet sheet turning and separated flow conditions are compared to the shear layers on the baseline GETS model. The shear layer is visualized by plotting the vorticity magnitude on a modified scale (for maximum contrast in the contour plot) as is shown in figure E.9. The smaller wake size leads to a reduction in total pressure loss as can be seen in figure E.10.

(a) GETS,  $y = 0$  plane(b) GETS,  $z = 0.5H$  plane(c) AFC, (jet turning)  $y = 0$  plane(d) AFC, (jet turning)  $z = 0.5H$  plane(e) AFC, (jet separation)  $y = 0$  plane(f) AFC, (jet separation)  $z = 0.5H$  plane**Figure E.9:** Vorticity magnitude for both models with jet turning and separated jet sheet

(a) GETS,  $y = 0$  plane(b) AFC, (jet turning)  $y = 0$  plane(c) AFC, (jet separation)  $y = 0$  plane

**Figure E.10:** Total pressure for the GETS model, the AFC model with jet turning and separated jet sheet

(a) Jet Turning, Vorticity =  $45 \frac{1}{s}$ (b) Jet separation, Vorticity =  $45 \frac{1}{s}$ (c) Jet Turning, Vorticity =  $25 \frac{1}{s}$ (d) Jet separation, Vorticity =  $25 \frac{1}{s}$ (e) Jet Turning, Vorticity =  $10 \frac{1}{s}$ (f) Jet separation, Vorticity =  $10 \frac{1}{s}$ **Figure E.11:** Vorticity iso surfaces for AFC model with jet turning and separated jet sheet

### E.2.2 Slot height variation

The simulations concerning the slot height variation yielded the results tabulated in E.3. Only the slot heights other than  $h = 1.5 \cdot 10^{-3}w$  height are tabulated, for those results see E.2.

$C_\mu$	$\zeta$	$R_1(R/W)$	$h(h/W)$	$C_{D^*}$	$C_D$	$\Delta C_D(\%)$
0.000	0.0	0.116	$7.7e - 004$	0.3066	0.3066	-3.6
0.011	1.4	0.116	$7.7e - 004$	0.2722	0.2864	-9.9
0.018	1.8	0.116	$7.7e - 004$	0.2533	0.2959	-6.9
0.027	2.2	0.116	$7.7e - 004$	0.2405	0.3298	3.7
0.038	2.6	0.116	$7.7e - 004$	0.2294	0.3877	21.9
0.008	1.2	0.058	$7.7e - 004$	0.2809	0.2865	-9.9
0.014	1.6	0.058	$7.7e - 004$	0.2611	0.2875	-9.6
0.017	1.8	0.058	$7.7e - 004$	0.2550	0.2976	-6.4
0.021	2.0	0.058	$7.7e - 004$	0.2507	0.3141	-1.2
0.026	2.2	0.058	$7.7e - 004$	0.2448	0.3341	5.1
0.031	2.4	0.058	$7.7e - 004$	0.2387	0.3595	13.0
0.036	2.6	0.058	$7.7e - 004$	0.2357	0.3940	23.9
0.031	1.4	0.116	$2.3e - 003$	0.2554	0.2696	-15.2
0.051	1.8	0.116	$2.3e - 003$	0.2542	0.2968	-6.7
0.077	2.2	0.116	$2.3e - 003$	0.2435	0.3328	4.6
0.107	2.6	0.116	$2.3e - 003$	0.2003	0.3586	12.8
0.031	1.4	0.058	$2.3e - 003$	0.2627	0.2769	-12.9
0.051	1.8	0.058	$2.3e - 003$	0.2738	0.3164	-0.5
0.077	2.2	0.058	$2.3e - 003$	0.2596	0.3489	9.7
0.107	2.6	0.058	$2.3e - 003$	0.2079	0.3662	15.2

**Table E.3:** Results Variation of slot height

### E.2.3 Radius variation

Results for the variation of Coanda surface radius, for constant radius ratio ( $R_2/R_1 = 1$ ) in table E.4. The slot height in these simulations is kept constant at  $h = 1.5 \cdot 10^{-3}w$  and for the reference radii results see table E.2.

$C_\mu$	$\zeta$	$R_1(R/W)$	$h(h/W)$	$C_{D^*}$	$C_D$	$\Delta C_D(\%)$
0.000	0.0	0.039	$1.5E - 003$	0.3137	0.3137	-1.4
0.015	1.2	0.039	$1.5E - 003$	0.2689	0.2745	-13.7
0.034	1.8	0.039	$1.5E - 003$	0.2463	0.2890	-9.1
0.061	2.4	0.039	$1.5E - 003$	0.2392	0.3599	13.2
0.000	0.0	0.173	$1.2E - 003$	0.3032	0.3032	-4.7
0.014	1.4	0.173	$1.2E - 003$	0.2854	0.2996	-5.8
0.022	1.8	0.173	$1.2E - 003$	0.2747	0.3174	-0.2
0.033	2.2	0.173	$1.2E - 003$	0.2536	0.3428	7.8
0.047	2.6	0.173	$1.2E - 003$	0.2323	0.3906	22.8

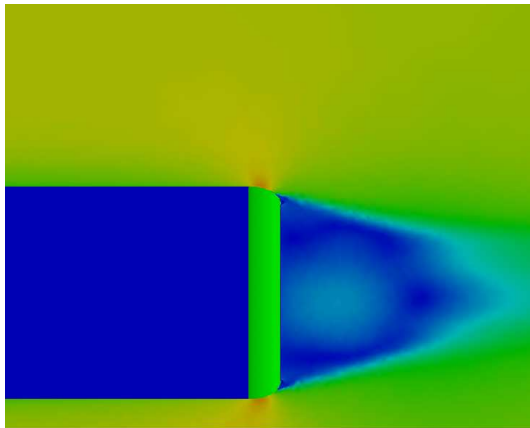
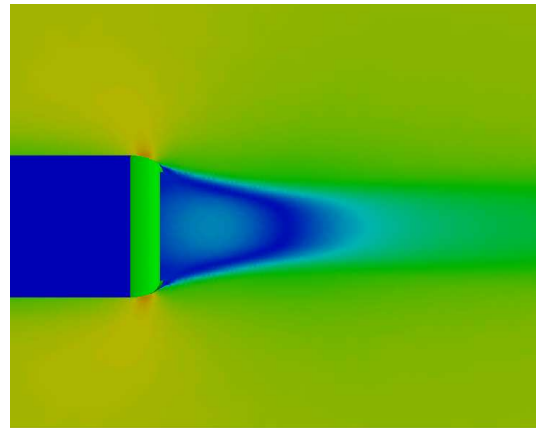
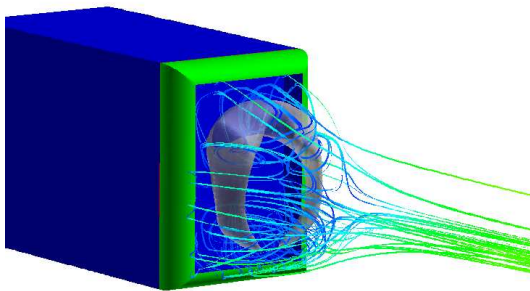
**Table E.4:** Results variation of radius

### E.2.4 Design optimization

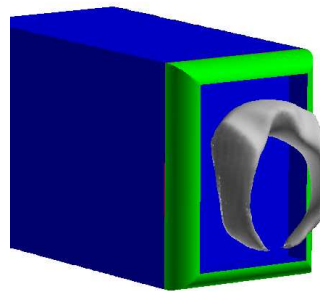
In the following table the results of the design optimization runs are tabulated.

$C_\mu$	$\zeta$	$R_2/R_1$	$h(h/W)$	$C_{D^*}$	$C_D$	$\Delta C_D(\%)$
0.000	0.00	0.8	$1.54E-003$	0.2995	0.2995	-5.8
0.000	0.00	1	$1.54E-003$	0.2969	0.2969	-6.6
0.000	0.00	1.2	$1.54E-003$	0.2824	0.2824	-11.2
0.000	0.00	1.4	$1.54E-003$	0.2764	0.2764	-13.1
0.000	0.00	1.6	$1.54E-003$	0.2711	0.2711	-14.7
0.011	1.00	0.8	$1.54E-003$	0.2743	0.2743	-13.7
0.011	1.00	1	$1.54E-003$	0.2735	0.2735	-14.0
0.011	1.00	1.2	$1.54E-003$	0.2659	0.2659	-16.4
0.011	1.00	1.4	$1.54E-003$	0.2624	0.2624	-17.5
0.011	1.00	1.6	$1.54E-003$	0.2605	0.2605	-18.1
0.021	1.40	0.8	$1.54E-003$	0.2537	0.2679	-15.8
0.021	1.40	1	$1.54E-003$	0.2495	0.2637	-17.1
0.021	1.40	1.2	$1.54E-003$	0.2460	0.2602	-18.2
0.021	1.40	1.4	$1.54E-003$	0.2429	0.2571	-19.1
0.021	1.40	1.6	$1.54E-003$	0.2416	0.2558	-19.6
0.018	1.28	0.8	$1.54E-003$	0.2584	0.2669	-16.1
0.018	1.28	1	$1.54E-003$	0.2551	0.2636	-17.1
0.018	1.28	1.2	$1.54E-003$	0.2514	0.2599	-18.3
0.018	1.28	1.4	$1.54E-003$	0.2479	0.2564	-19.4
0.018	1.28	1.6	$1.54E-003$	0.2465	0.2550	-19.8
0.026	1.53	0.8	$1.54E-003$	0.2486	0.2705	-14.9
0.026	1.53	1	$1.54E-003$	0.2432	0.2652	-16.6
0.026	1.53	1.2	$1.54E-003$	0.2408	0.2627	-17.4
0.026	1.53	1.4	$1.54E-003$	0.2382	0.2601	-18.2
0.026	1.53	1.6	$1.54E-003$	0.2365	0.2584	-18.7

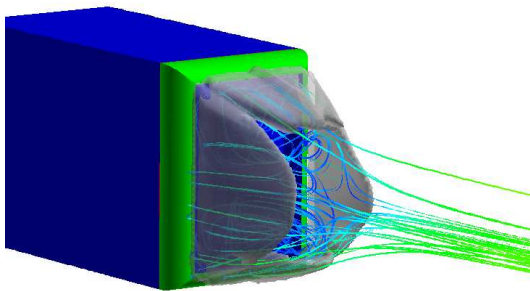
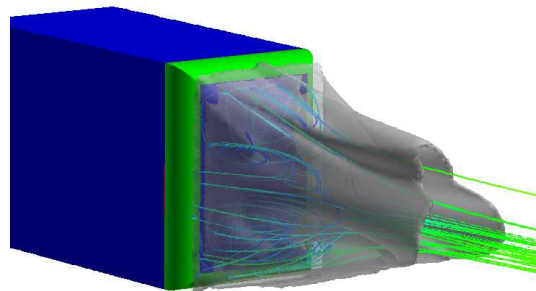
**Table E.5:** Results design optimization

(a) Velocity magnitude in  $y = 0$  plane(b) Velocity magnitude in  $z = 0.5H$  plane

(c) Stream lines, colored by velocity magnitude



(d) Vortex core visualization

(e) Vorticity =  $45 \frac{1}{s}$ (f) Vorticity =  $15 \frac{1}{s}$ **Figure E.12:** Wake visualization optimal AFC model



